Dye-doped Silica Nanoparticles for Cancer Cell Staining and Detection

Claire O'Connell B.Sc.

Thesis Submitted for the Award of Doctor of Philosophy

School of Physical Sciences

Dublin City University

Research supervisor:

Prof. Colette McDonagh

September 2017

Declaration

I hereby certify that this material, which I now submit for assessment on the programme of study leading to the award of Ph.D. is entirely my own work, and that I have exercised reasonable care to ensure that the work is original, and does not to the best of my knowledge breach any law of copyright, and has not been taken from the work of others save and to the extent that such work has been cited and acknowledged within the text of my work.

Signed: _____   ID No.: 59418270   Date: _____.

Acknowledgments

First and foremost, thank you to Prof. Colette McDonagh for all your time, advice and guidance during the project over the last number of years which has been invaluable. To Dr. Rob Nooney, thanks for teaching me everything you know about nanoparticles, for the great ideas and for being a mentor and friend. Thanks to Dr. Daragh Byrne for your help, input and advice with the plasmonics aspect of the project and provision of gratings. To Dr. Dorota Wencel and past members of the Optical Sensors Group, thanks for your advice and help on various aspects of the project.

Thanks to the Irish Research Council, for their funding not only the first time around for a research masters but also the second time, to extend it to a PhD. Thanks to the Graduate Studies Office team, particularly Jonny Hobson, and Aisling Robinson, from BDI, who helped with the second round of funding. Without them, I otherwise could not have continued my studies.

Thank you to both Dr. Macdara Glynn and Dr. Damien King from the microfluidics group for their help getting started on the cell aspect of the project. Thanks to Richard O'Kennedy's group for the use of their cell culture facilities and very helpful advice and tips on biological queries that I've had over the years. Thanks to Dr. Ronan Murphy and Javier Monedero in the School of Health and Human Performance for their help with instrumentation aspects of the project. Particular thanks to Rob Wallace, for troubleshooting and late evening company and conversation when carrying out flow cytometry experiments.

To all those that I have interacted with or shared lab space with in BDI, in the S252 lab, there are too many of you to mention, thanks for all your advice, the introduction to new music and ensuring that no day was dull. Thanks to all the staff and academics of the School of Physical Sciences for your help along the way in getting this far since my undergraduate. I really would not have got this far without you!

To the lunch time postgrad crew, particularly Ben and Stephen, and all the other postgraduates of DCU, for all their good humour, friendships and great memories that

we have created over the years. To my friends from university, and my friends from home, both near and in Australia (Angela), thanks for all your encouragement over the years.

To my family, my parents, Mary and Thomas, and siblings, Áine and Tomás, thank you for never doubting me for a second with your support, copious amounts of tea and chats.

To Floris, thanks for reminding me that my PhD was not everything, for putting up with my bad jokes and being my rock when things got stressful. To everyone I have forgotten to mention, in and out of DCU, thank you also.

I have all of you to thank for the completion of this thesis and will always be grateful for the amazing opportunity I have had.

Table of Contents

i. List of abbreviations

APC – allophycocyanine
AOT – dioctyl sulfosuccinate sodium salt
APTES – 3-aminopropyltriethoxysilane
APTMS – aminopropyltrimethoxysilane
BCA - bicinchoninic acid
BSA – bovine serum albumin
CD – cluster of differentiation
CT – computed tomography
CTC – circulating tumour cell
DAPI – 4',6-Diamidino-2-phenylindole
DLS – dynamic light scattering instrument
DMEM - Dulbecco's modified Eagle's medium
DNA – deoxyribonucleic acid
EDC – 1-Ethyl-3-(3-dimethylaminopropyl)carbodiimide
EDTA – ethylenediaminetetraacetic acid
EM – electromagnetic
Fc – constant region of an antibody
FDA – Food and Drug Association
FBS – fetal bovine serum
FITC – fluorescein isothiocyanate
FRET – Förster Resonance Energy Transfer
FSC – forward scatter
GFP – green fluorescent protein
HeLa – cervical cancer cell line
IgG – immunoglobulin G
LNCaP – prostate cancer cell line
LOD – limit of detection
LSPR – localised surface plasmon resonance

MCF-7 – breast cancer cell line
MES – 2-(N-morpholino)ethanesulfonic acid
MFI – median fluorescence intensity
MRI – magnetic resonance imaging
NHS – N-hydroxysuccinimide
NIR – near infrared
NP – nanoparticle
NP5 – polyoxyethylene (5) nonylphenylether
PBS – phosphate buffer saline
PDMS – polydimethylsiloxane
PEG – polyethylene glycol
PET – positron emission tomography
PMT – photomultiplier tube
PNT1A – healthy prostate cell line
PVP – polyvinylpyrrolidone
RNA – ribonucleic acid
ROI – region of interest
Rubpy - tris(bipyridine)ruthenium(II) chloride
SPP – surface plasmon polariton
SPR – surface plasmon resonance
SSC – side scatter
STED – Stimulated emission depletion
STORM – stochastic optical reconstruction microscopy
TEM – transmission electron microscopy
TEOS – tetraethyl orthosilicate
WBC – white blood cell
WGA – wheat germ agglutinin

ii. List of figures

iii. List of tables

Abstract

Claire O'Connell

Dye-doped silica nanoparticles for cancer cell staining and detection

Cancer is a leading cause of death worldwide, with metastasis responsible for a majority of these deaths. Circulating tumour cells (CTCs) present in blood samples can be a precursor to metastasis and if detected in low numbers can indicate early stage cancer. In this work, fluorescent silica nanoparticles (NPs) were developed to detect these CTCs. NPs approximately 40 nm in diameter were doped with two different concentrations of Cyanine5 dye molecules, using the reverse microemulsion method. The NPs were over 100 times brighter than Cyanine5 free dye and the measured fluorescence intensity matched a homo-Förster Resonance Energy Transfer model. NPs were conjugated with anti-epithelial cellular adhesion molecule (EpCAM) antibody to the NP surface for immunospecific targeting. The NP labels were shown to selectively bind to model CTC lines, MCF-7 and LNCaP, a metastatic breast and prostate cancer cell line respectively, by targeting EpCAM present on the cell's membrane.

In flow cytometry experiments, the NPs were twice as bright as commercial anti-EpCAM red fluorophore conjugates, APC and AlexaFluor®647 on the MCF-7 cell line. This increase was achieved while keeping non-specific binding low with a non-metastatic cancer control cell line (HeLa). The NPs were also immunospecific in fluorescence microscopy experiments. Confocal microscopy was used to confirm that the NPs were located on the cell's surface, matching with the location of the EpCAM marker. The NPs were tested in a mixed cell environment by spiking CTCs into lysed blood samples where the NPs successfully identified CTCs at different ratios to white blood cells.

Some experiments were also conducted to investigate the use of NPs for secondary antibody staining of EpCAM on CTCs. In addition, gold grating plasmonic enhanced fluorescence imaging of CTCs was investigated briefly. In summary, the NP labels have excellent potential in biomedical applications, particularly in cell labelling and diagnostics.

Chapter 1: Introduction

1.1 Motivation and context

Cancer is the second leading cause of death worldwide, with 8.8 million deaths occurring in 2015 and it has been predicted that this number is going to rise by 70% over the next 20 years [1,2]. The majority of cancer deaths are caused from the phenomenon that is called metastasis which is the spread of cancer from the primary tumour site to form secondary tumours elsewhere in the body. This happens due to proliferation of cancer cells from the primary tumour, called circulating tumour cells (CTCs), that can enter the blood stream and spread to other organs. The metastasis of cancer makes it very difficult to treat, primarily because these cells are found in blood samples at such a low range of concentrations. These numbers vary from cancer type and stage but can be as low as 1-10 in every millilitre of blood, which contains millions of healthy blood cells [3]. The attraction of research into these cells is that accurate identification and quantification could represent a non-invasive method of assessing cancer patient disease stage or evaluation of patient treatment where, usually, patients routinely endure long waiting times for scans or invasive biopsies.

1.2 Current detection methods of cancer

Currently, cancer diagnosis in patients is primarily based on self-reporting, where a patient, upon finding a lump or presenting with other symptoms of being unwell, will visit their local general physician. The doctor will send the patient for further testing in the form of biopsy tests and imaging scans that can be expensive. It is a well-known fact that time is of the essence when dealing with cancer, so long waiting lists in hospitals for these procedures can increase the mortality rate of the patient. Furthermore, even when results are returned, the diagnosis can often be of late stage cancer, for which treatment has a high rate of failure.

1.2.1 Imaging

There are many types of imaging systems that can be used to image and detect cancer tumours, leading to diagnosis. Irish breast cancer patients with self-reported lumps or those in the age bracket of 50-69 that are more prone to the risk of breast cancer, are sent for mammograms in order to detect tumours. A mammogram consists of one or two x-ray images of the breast tissue and identification of a tumour by means of denser tissue or some calcification spots which can signify tumour growth [4]. This method can also be used to image lung cancer or detect cancer that has metastasised [5]. Current imaging techniques can detect tumours that are less than 15mm in size when assessed by a skilled radiologist and imaged correctly within 85-90% accuracy [6]. The problem with this method is that when the tumour is larger in size, patients have a decreased survival rate. When tumours found in patients are greater than 5cm, the patient has only a 70% five-year survival rate compared with 95% when tumours are found at less than 2cm [7,8].

A computed tomography (CT) scan is usually carried out on an organ such as the liver or lung and abdomen to detect cancer tumours [5]. CT scans consist of a series of X-ray scans taken at multiple angles to form detailed images in either planes of view or even to construct 3D images of an organ. As different types of tissue absorb the X-rays to varying degrees, the distinction can be made between different tissue types and tumours.

Positron emission tomography (PET) scans work similarly to CT scans and are usually used as a complementary technique to CT scans. Instead of using X-rays, PET scans use a radioactive tracer that emits gamma rays [9]. The tracer, usually an isotope with a short half-life such as carbon-11, oxygen-15, nitrogen-13, and fluorine-18, when combined with certain biological functionality, like fludeoxyglucose, will detect tumours as they usually have higher uptake of glucose than regular tissue [9]. The positron emission of these radioactive isotopes combines with electrons from surrounding atoms to form a pair of gamma rays by annihilation which are then detected by the scanner [9]. This is carried out in targeted areas of the body or organs to create high detail images.

Magnetic resonance imaging (MRI) scans use an external magnetic field, in which nuclei with certain spin can be aligned in this uniform magnetic field. Hydrogen atoms have a non-zero spin, which encompasses a magnetic and angular momentum, and are found in tissues of the body such as fat and water. As radio waves are pulsed into a sample containing hydrogen atoms within the magnetic field, they excited the hydrogen nuclear

spin and, depending on the difference in relaxation time of the hydrogen in the different types of tissue, the technique can be used to distinguish between healthy and cancerous tissues [10]. As these scans avoid the use of ionizing radiation, they are primarily used for the imaging of the brain and spinal cord [11].

1.2.2 Biopsy

A variety of biopsies can be carried out to investigate the suspicion of cancer depending on the type of cancer. Endoscopic biopsies are carried out for forms of cancer such as those of the oesophagus, colorectal, lung or urinary tract, to name just a few [12]. Another form of biopsy is the needle biopsy, where either fluid or a small sample of tissue is extracted from the area of interest for further testing and is usually used for cancers such as breast and thyroid or even in an enlarged lymph node [12]. A skin biopsy involves the removal of a piece of skin from the patient which is then sent for further analysis and usually is for the detection of melanoma. A bone marrow biopsy involves a needle insertion into the bone marrow to search for abnormal cells linked with blood cancers or metastasis [12]. The last type of biopsy that will be mentioned is a surgical biopsy and this type is performed on suspicious areas that cannot be accessed by any of the other methods of biopsies. When the fluid, cell or tissue sample has been obtained from the patient, this is used for further testing and tissue samples can be thinly cut into slices and stained for certain cancer markers which are examined under the microscope [12]. In some situations, a pathologist will examine the cell samples to determine the particular stage or type of cancer. One thing that is common to all these biopsies is that they are extremely invasive for a patient as well as introducing a risk of infection from having the procedure. Stress induced from waiting time of tests and results can have detrimental effects on patient, especially when this can be up to 25 weeks for brain magnetic resonance imaging (MRI) for public patients in the Republic of Ireland [13]. If it were possible to reduce these wait times using a simple blood sample test then this would be a huge achievement. This is another reason to strive for non-invasive detection systems of cancer diagnosis.

1.3 Significance of detection of CTCs

As CTCs are a precursor to metastasis, research into their enumeration and link to cancer stage is of great importance, as it requires only a blood draw which could be incorporated

into a patient's routine check-up. Low number detection rates of these CTCs, ≤5 per 7.5mL of blood, has been shown to have huge impact on mortality rate of patients whereby patients with higher than 5 CTCs had a predicted overall survival time of 8.2 months compared with 18 months to patients with a count less than 5 [14]. This study was carried out using an FDA approved CTC detection instrument called CellSearch (Menarini-Silicon Biosystems Inc., CA, USA) which is an expensive system that removes CTCs from a blood sample with the use of immuno-magnetic beads followed by a staining procedure to verify that the cell is a CTC. The technique is discussed in more detail in section 2.6. Other companies have similar systems for the detection of CTCs, some are based solely on fluorescence, such as the CytoTrack instrument, (CytoTrack ApS, Lyngby, Denmark) and some are based on the evaluation of size and deformation differences between blood cells and CTCs, such as Celsee PREP100 or PREP400 (CelSee Diagnostics, MI, USA), after which the cells are stained to verify that there are markers present for CTCs on captured cells.

The focus for this PhD work is to develop a very bright CTC stain using dye-doped silica nanoparticles. These particles can incorporate hundreds, and even thousands, of dye molecules inside a single particle so that they can be used as a tool to provide a high degree of separation, based on photon emission, between positive and negative cell populations [15,16]. The proof of concept is to determine whether CTCs can be distinguished by using only a nanoparticle based fluorescence stain with conventional lab instruments such as a flow cytometer or microscope.

1.4 Overview of work and structure of the thesis

The work carried out for this thesis focused on successfully using dye-doped silica nanoparticles for cell staining to identify CTCs. In order to do this, synthesis and analysis of Cyanine5 dye-doped nanoparticles was undertaken. A cell staining method was developed in order to evaluate the efficiency of the particles on two cell lines that expressed a marker for CTCs; MCF-7 breast cancer and LNCaP prostate cancer, and compared to cell lines that did not express EpCAM; cervical cancer cell line, HeLa, and healthy prostate cell line, PNT1A. Initial work concentrated on characterising the efficiency of the staining using fluorescence microscopy and flow cytometry on the cell lines separately. Following this, the EpCAM positive cells were spiked into blood

samples to imitate patient blood samples to evaluate the nanoparticles ability to label the cells correctly. Secondary antibody staining methods were investigated to improve sensitivity and signal and nanoparticles were also used with grating coupled surface plasmon resonance for enhanced cell imaging.

The structure of this PhD thesis comprises of a brief introductory chapter, chapter 1, to give context of the project, followed by chapter 2 which provides the theory and background behind the various aspects involved within this thesis and also contains a section on state of the art nanoparticle synthesis and application in cell staining. Chapter 3 gives a brief overview of the instrumentation and characterisation techniques used throughout the PhD, while Chapter 4 describes the synthesis, characterisation and development of the fluorescent nanoparticles. Chapter 5 details the imaging and flow cytometry results from using the nanoparticles as a stain and comparison to commercially available dyes. Chapter 6 explores the use of nanoparticles to detect the CTCs in a mixed blood cell population. Chapter 7 investigates the use of nanoparticles as a secondary antibody label and chapter 8 is an exploratory chapter on the use of the nanoparticles on gold gratings for surface plasmon resonance enhancement imaging. Finally, chapter 9 summarises the work completed in the thesis and details how this work could be furthered in the future.

1.5 Research aims and objectives

Main Aim:

To demonstrate the specific staining of circulating tumour cells from blood using fluorescent silica nanoparticles for cell staining, both in flow cytometry and imaging, in comparison to single dye labels.

Objectives:

1. Synthesize and characterise Cyanine5-doped silica nanoparticles using a microemulsion method.
2. Successfully conjugate antibodies that are specific to markers for CTCs to the nanoparticle surface.

3. Use the nanoparticles to stain cell lines that represent CTCs specifically, while keeping non-specific binding low and characterise the staining using fluorescence imaging and flow cytometry.

4. Spike the cell line CTCs into blood and investigate if the nanoparticles can detect them from a mixed blood cell population via flow cytometry and imaging.

5. Investigate the use of a more sensitive detection assay such as secondary antibody labelling to improve signal enhancement.

6. Investigate the use of the nanoparticles with gold grating surfaces to further enhance the signal when imaging for sensitive detection of rare markers.

1.6 References

[1] M.H. Forouzanfar, L. Alexander, H.R. Anderson, V.F. Bachman, S. Biryukov, M. Brauer, R. Burnett, D. Casey, M.M. Coates, A. Cohen, K. Delwiche, K. Estep, J.J. Frostad, K.C. Astha, H.H. Kyu, M. Moradi-Lakeh, et al, Global, regional, and national comparative risk assessment of 79 behavioural, environmental and occupational, and metabolic risks or clusters of risks in 188 countries, 1990-2013: A systematic analysis for the Global Burden of Disease Study 2013, Lancet. 386 (2015) 2287-2323.

[2] M.H. Forouzanfar, A. Afshin, L.T. Alexander, H.R. Anderson, Z.A. Bhutta, S. Biryukov, W.W. Godwin, et al, Global, regional, and national comparative risk assessment of 79 behavioural, environmental and occupational, and metabolic risks or clusters of risks, 1990–2015: a systematic analysis for the Global Burden of Disease Study 2015, Lancet. 388 (2016) 1659-1724.

[3] H.W. Hou, M.E. Warkiani, B.L. Khoo, Z.R. Li, R.A. Soo, D.S.-. Tan, W.-. Lim, J. Han, A.A.S. Bhagat, C.T. Lim, Isolation and retrieval of circulating tumor cells using centrifugal forces, Sci. Rep. 3 (2013).

[4] National Cancer Institute, Mammograms in Breast Cancer Types, 2017 (2016).

[5] American Cancer Society, Tests to find out if breast cancer has spread (CT, PET, Bone Scan, MRI), 2017 (2017).

[6] L. Tabár, P.B. Dean, T.H.-. Chen, A.M.-. Yen, S.Y.-. Chiu, T. Tot, R.A. Smith, S.W. Duffy, The impact of mammography screening on the diagnosis and management of early-phase breast cancer, in: Anonymous Breast Cancer: A New Era in Management, , 2014, pp. 31-78.

[7] E.A. Asare, M. Washington, D.M. Gress, J.E. Gershenwald, F.L. Greene, Improving the quality of cancer staging, CA Cancer. J. Clin. 65 (2015) 261-263.

[8] American Cancer Society, Breast cancer facts and figures 2015-2016, 861015 (2015).

[9] S.I. Ziegler, Positron emission tomography: Principles, technology, and recent developments, Nucl. Phys. A. 752 (2005) 679c-687c.

[10] E. Odeblad, G. Lindström, Some preliminary observations on the proton magnetic resonance in biological samples, Acta Radiologica. 43 (1955) 469.

[11] The Round Table Foundation, Chapter 21 Facts and Figures of magnetic resonance, a peer reviewed critical introduction, 2017 (2017).

[12] Mayo Clinic, Biopsy: Types of biopsy procedures used to diagnose cancer, 2017 (2016).

[13] P. Cullen, Public patients wait up to 25 times longer for cancer tests, The Irish Times. (2016).

[14] M. Cristofanilli, G.T. Budd, M.J. Ellis, A. Stopeck, J. Matera, M.C. Miller, J.M. Reuben, G.V. Doyle, W.J. Allard, L.W.M.M. Terstappen, D.F. Hayes, Circulating tumor cells, disease progression, and survival in metastatic breast cancer, New Engl. J. Med. 351 (2004) 781-791.

[15] M.-. Estévez, M.B. O'Donoghue, X. Chen, W. Tan, Highly fluorescent dye-doped silica nanoparticles increase flow cytometry sensitivity for cancer cell monitoring, Nano. Res. 2 (2009) 448-461.

[16] R.I. Nooney, C.M.N. McCahey, O. Stranik, X. Le Guevel, C. McDonagh, B.D. MacCraith, Experimental and theoretical studies of the optimisation of fluorescence from near-infrared dye-doped silica nanoparticles, Anal. Bioanal. Chem. 393 (2009) 1143-1149.

Chapter 2: Theory, background and state of the art

2.1 Introduction

This chapter describes the fundamental theory behind the work in this thesis relating to fluorescence phenomena and includes some background on nanoparticle synthesis, antibodies and blood. Included in this chapter is a description of the state of the art on the current approaches taken to use targeted dye-doped silica nanoparticles in the application of cell staining and flow cytometry for cancer cells.

2.2 Fluorescence phenomena

2.2.1 Fluorescence and Stokes shift

Luminescence can be described as the emission of light from a substance and this emission can be stimulated in many ways. A summary of the types of light emission can be viewed in Fig 2.1. For photoluminescence, there are three primary forms of light emission and these are fluorescence, phosphorescence and Raman emission.
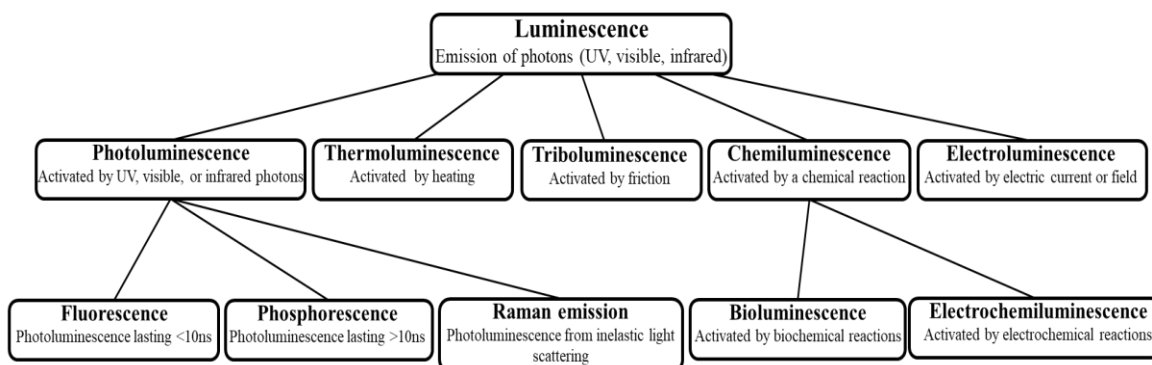
Fig 2.1: Summary of some types of luminescence adapted from [1].

In the instance of fluorescence, light emission is stimulated by photons from the UV, visible or infrared wavelengths of light. Photon emission is only generated when

electrons in the fluorophore become excited, from a ground state to a higher electronic state, by incoming photons of specific energy or frequency. These energy states, for both the excited and ground state, contain discrete vibrational and rotational levels. An electron will only be excited to a higher energy state if the energy of the absorbed photon is equal to or greater than the energy needed to make the excited electronic transition, as shown in the Jablonski diagram Fig 2.2 (left), such that

$$\Delta E = h\nu \qquad\qquad \text{(Eq. 2.1)}$$

where E is energy of the photon, h is Planck's constant and ν is the frequency of the electromagnetic radiation/photon. The electron will favour a specific vibrational state during electronic excitation. One particular vibrational state will be more likely if it has a similar wavefunction to that of the electron in its ground state, as predicted by the Franck-Condon principle [2,3]. This is shown in Fig 2.2 (right), which shows schematically the processes of photon absorption and fluorescence with relevant energy levels.

When the ground state electron reaches the higher electronic and vibrational state, internal conversion happens. This is where vibrational relaxation of the electron occurs, with a small thermal energy loss, which happens on the pico-second scale [4]. When the electron relaxes back to a lower energy state, it will enter a vibrational state with similar wavefunction to that of the excited electron and release the energy in the form of a photon with less energy than that of the initial absorbed photons. This process is known as fluorescence. The released photon has less energy and, consequently, has a shorter frequency and longer wavelength. Therefore, it is usually shifted to the red in terms of wavelength compared to its absorption wavelength.
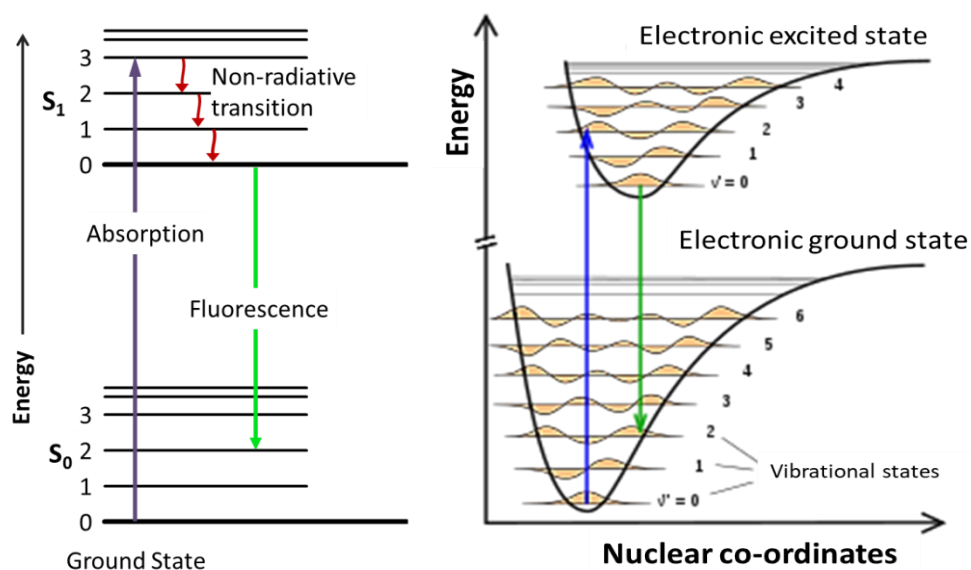
Fig 2.2: Simplified Jablonski luminescence diagram (left) and the Franck-Condon principle diagram for the excitation of an electron with light. S refers to singlet state excitation. Reproduced under Creative Commons CC0 1.0 Universal Public Domain Dedication.

The difference in wavelength between the absorbed and emitted photon is known as the Stokes shift of a molecule. In general, it is the difference in wavelength between the peak photon absorption and emission of a fluorophore and an example of an absorption and emission spectrum can be seen in Fig 2.3 for Cyanine5 free dye. A larger Stokes shift allows for a more efficient collection of emission photons, where there is less overlap between absorption and emission spectra and is desirable in a dye but not necessary to detect emitted photons.
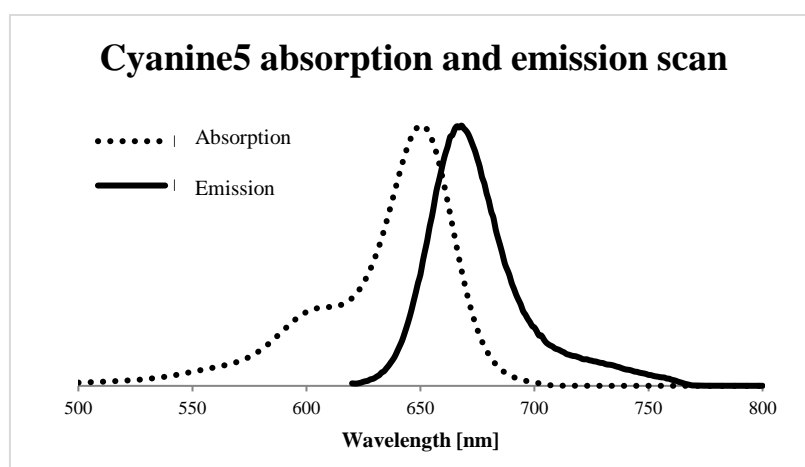
Fig 2.3: Absorption and emission scan for Cyanine5 dye molecule exhibiting a small Stokes shift measured on spectrophotometer.

Phosphorescence occurs in a molecule when an electron, which has been excited to a higher electronic state and has relaxed to the lowest vibrational state, undergoes intersystem crossing and relaxes from a singlet state to the triplet state. When the electrons relax from the triplet state, the process is known as phosphorescence. Photons that are emitted from phosphorescence are on the microsecond to sub-second scale and thus are much longer than for fluorescence processes, which are emitted in nanoseconds or less [4]. The dyes used in this thesis luminesce via fluorescence but for completeness phosphorescence is also explained.

2.2.2 Molar absorption

High molar absorbance is a property that is desirable for fluorescent molecules. Molar absorptivity is the measure of the efficiency of photon absorption of a chemical species at a specific wavelength. The molar attenuation coefficient ε can be calculated using a spectrophotometer and Beer-Lambert's Law. ε is inversely proportional to the concentration of the dye c, the pathlength l and the absorbance A to form the equation:

$$A = \varepsilon c l \qquad \text{(Eq. 2.2)}$$

Dyes with higher molar absorbance are desirable as they require shorter exposure times for detection using imaging techniques, which is an ideal property for the application of cell staining.

2.2.3 Quantum yield

Simply put, the quantum yield is a ratio of the number of photons emitted compared to the number that are absorbed by a fluorescent molecule [4]. The more efficient the molecule, the closer the value of the quantum yield will be to 1. When a molecule is excited, the energy can dissipate into processes that are radiative, e.g. produce a photon, or non-radiative, such as thermal energy loss. The equation to describe these processes is given by:

$$\phi = \frac{\Gamma}{\Gamma + k_{nr}} \qquad \text{(Eq. 2.3)}$$

where ϕ is the quantum yield, Γ is the sum of the radiative rates and k_{nr} is the sum of the non-radiative rates.

2.2.4 Fluorescence quenching

Fluorescence quenching is the reduction in photon emission due to an increase in non-radiative energy decay rates. It can be caused by static quenching or dynamic quenching, also known as collisional quenching, and can also be induced by energy or electron transfer [4]. Static quenching happens upon the formation of a complex between the quencher and fluorescent molecule when both are in the ground states, resulting in a non-radiative molecule. Dynamic or collisional quenching occurs when the fluorescent molecule is excited and, due to a collision with a molecule in solution, has transferred its energy to the quenching molecule. Oxygen is a known quenching molecule for fluorescent molecules [5]. Quenching can be caused photochemically, because of a transition of oxygen from the singlet state to triplet state, which is very reactive, and when it comes into contact with the excited fluorescent molecule it can deactivate it. Dyes that are not as susceptible to this are known as photostable dyes [6]. Long photostability is important for microscopy and analysis of living cells where there may be high levels of oxygen present. Also in microscopy, longer exposure times are usually needed for imaging with the microscope lamp light compared to the exposure time needed with a laser in flow cytometry. This longer exposure time can induce more excitation-emission cycles in a fluorophore which lead to photobleaching.

2.2.5 Förster resonance energy transfer (FRET)

There are a number of non-radiative processes by which an electron can lose energy. Thermal energy loss occurs initially when the excited electron relaxes vibrationally. Another process called Förster resonance energy transfer (FRET), can occur when two fluorescent molecules have overlapping emission and excitation spectra and are within close proximity, on the nanometre scale, to each other [4]. FRET happens when an emission photon from one dye molecule, the donor, has enough energy to excite another dye molecule, the acceptor molecule. This process can also occur in two adjacent fluorescent molecules of the same dye within a close enough radius, and small Stokes shift. When FRET happens in this instance, between two of the same molecules, it is known as homo-FRET. The amount of energy that is transferred from the donor to acceptor is inversely proportional to the distance to the power of 6 such that

$$E = \frac{R_0^6}{R_0^6 + r^6}$$

(Eq. 2.4)

where E is the energy of the photon, r is the distance between the donor and acceptor molecule and R_0 is the Förster radius which is the distance at which there is a 50% energy transfer between molecules [7]. For dyes with a large Stokes shift, homo-FRET is less likely to occur due to the larger separation between absorption and emission peaks.

2.3 Fluorophores

There are many types of fluorescent dyes, including those naturally found in proteins or chemically synthesised, that cover the ultraviolet, visible and infrared spectrum. Their photophysical properties are of significant importance if they are to be useful as optical sensors. These desirable properties include a high molar absorbance, high quantum yield, large Stokes shift and photostability. For the application of CTC detection, a dye with a high quantum yield and large Stokes shift would be an ideal candidate. Dyes that fluoresce in the red and near infrared are of interest due to low intrinsic fluorescence of biological samples at these wavelengths [8]. In addition, whole blood only has a weak absorption within this far-red region. It has been found that far-red dyes make good candidates for utilisation in biological applications, more specifically for applications where sensitivity is an issue and the background fluorescence can hinder an observable result. Some dyes that fluoresce in the red wavelength region, close to 650nm, are included in Table 2.1.

Table 2.1: Fluorescent dyes which emit in the red wavelength of the spectrum

Dye	Absorption Max [nm]	Emission Max [nm]	Stokes Shift [nm]	Quantum Yield[†]	Molar attenuation coefficient [M^{-1} cm^{-1}]	Ref
Allophycocyanine (APC)	650	660	10	0.68	700,000	[9]
ATTO 647N	644	669	25	0.65	150000	[10]
DY-649P1	653	672	19	*	250000	[11]
Alexa Fluor® 647	650	665	15	0.33	239000	[12]
Cyanine5	646	662	16	0.2	250000	[13]

*no quantum yield value available.   [†] Provided by manufacturer, no medium detailed

Some of the dyes in Table 2.1 have different advantages over the others. For example, allophycocyanine (APC) and ATTO 647N dyes have a very high quantum yield of 0.68

and 0.65 respectively but the ATTO 647N has a large Stokes shift which is more ideal for easier detection of the emission photons. DY-649P1 also has a relatively large Stokes shift. However, no quantum yield information is available for this dye.

The two most commonly used dyes in the red part of the spectrum are APC and AlexaFluor®647. APC is a pigment found in algae and AlexaFluor®647 is a synthesised dye. They are favoured over other dyes because they have a relatively high quantum yield, as well as being photostable. New labels that emit in the red have more recently been established requiring ultra violet or violet excitation from BD Biosciences [14,15]. They are known as conducting polymer dyes and have a large Stokes shift, thus, they can emit in a broad range of the visible spectrum and even the near infrared.

APC has a very high molar attenuation coefficient and is followed by DY-649P1 and Cyanine5. Although Cyanine5 has a low quantum yield, its molar attenuation coefficient is relatively high. Cyanine5 could be used as a CTC stain, although, the signal must be amplified and this can be achieved, for example, by encapsulating the dye in silica nanoparticles, which was carried out throughout the course of this work. This dye encapsulating method will be discussed in more detail in section 2.7 and the molecular structure of Cyanine5 can be seen in Fig 2.4.
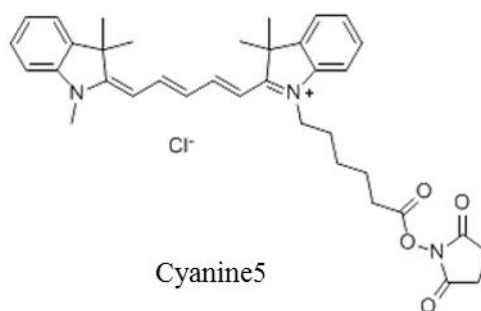
Fig 2.4: Chemical structure of cyanine5 NHS ester dye adapted from [13]

For the work in this thesis, nanoparticles were synthesised with Cyanine5 dye that is both absorbs and emits photons in the red and the NPs were benchmarked against both APC and AlexaFluor®647 to determine how they perform in the application of cell staining and flow cytometry comparatively in terms of brightness. This work could allow researchers to use commonly available dyes, such as Cyanine5, with lower quantum yields, to close the gap on more expensive, higher quantum yield dye or those excited at ultraviolet wavelengths without the need to add a new excitation source as required for the conducting polymer dyes.

2.4 Zeta potential

Zeta potential is the indication of surface charge that a particle has at a certain distance away from its surface. It is the potential difference between the solution in which the particle is placed and the layer of fluid that is attached to the particle. The particle is surrounded by an 'electrical double layer' comprised of two layers of ions. The Stern layer is the innermost layer and is closest to the particle where charged ions in solution are greatly attracted to the particle. The next layer is the diffuse layer, where ions are attracted to the particle and there are equal numbers of oppositely charged ions in this layer. The zeta potential is measured at the outer side of the diffuse layer known as the 'slipping plane'; see Fig 2.5 for a diagram of the layers around a charged particle.
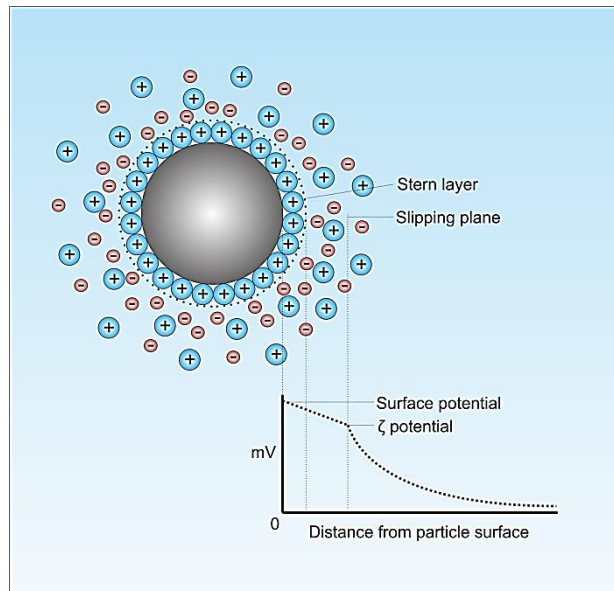
Fig 2.5: Illustration of the electric double layer (diffuse and stern layer) around a charged particle from [16]. Reproduced under creative commons licence CC-BY-SA 3.0.

The mobility of the particles can be measured using the equation

$$V_D = \frac{Uq}{2\pi} cos\frac{\theta}{2}$$ (Eq. 2.5)

where V_D is the frequency shift of the scattered light, U is the particle mobility, θ is the scattering angle, q is the scattering vector given by $q=4\pi n Sin(\theta/2)/\lambda$, λ is the wavelength of the incident light and n is the refractive index of the medium. This light scattering is measured on the dynamic light scattering (DLS) instrument which is discussed in more detail in section 3.5.

The particle mobility is related to the particle's zeta potential Z and can be calculated from Smoluchowski's equation

$$Z = \frac{\eta}{\varepsilon_0 \varepsilon_r} U \qquad \text{(Eq. 2.6)}$$

where η is the viscosity of the solvent, ε_0 is the dielectric constant in vacuum and ε_r is the relative dielectric constant of the solvent [17].

2.5 Antibodies

Antibodies are part of the immune system in the body. They are proteins in the shape of a Y, as seen in Fig. 2.6, and are comprised of different sections. They are produced by a subset of B cells called plasma cells to protect the body from invasion from pathogens like bacteria and viruses.
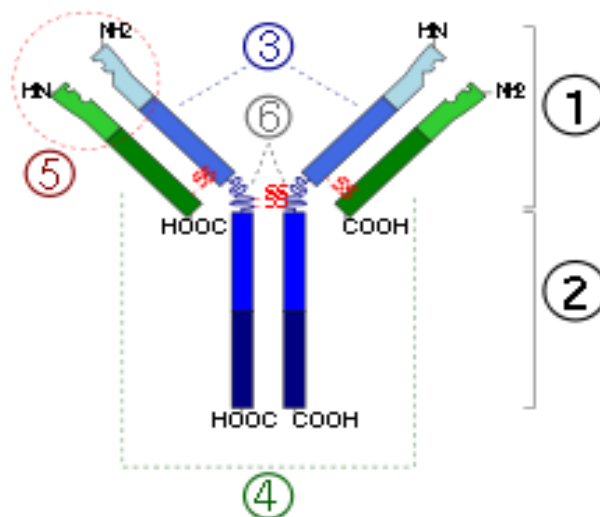
Fig 2.6: Antibody schematic of different regions with: (1) Fab region; (2) constant region (Fc); (3) heavy chain (blue) comprised of one variable domain (light blue) followed by a constant domain (dark blue), a hinge region, and two more constant domains (dark and navy blue); (4) Light chain (green) with one variable (light green) and one constant domain (dark green); (5) Antigen binding site (paratope) and (6) Hinge regions [18]. Reproduced under creative commons license CC-BY-SA 3.0.

2.5.1 Antibody structure

The two 'arms' on the Y shape, called Fab sections, have receptors at the end that can interact with pathogens [19]. These are known as paratopes. On the surface of a pathogen there are many proteins that are foreign to the body, and are called antigens, and

antibodies whose receptors are a complement of the antigens will selectively bind to the pathogen. The antibodies can then signal to surrounding blood cells to remove the pathogen from the body through the stem part, or constant region, of the antibody which is also known as the Fc region [19].

Antibodies can be bioengineered to be specific to antigens. This is done through the use of mammals for polyclonal antibodies (multiple antibodies that can bind to the same antigen) or hybridoma cells for monocolonal antibodies (one antibody specific to one antigen). Polyclonal antibodies are found in the blood of mammals and can be purified to harvest them and monoclonal antibodies are secreted by hybridoma cells and purified using affinity chromatography. For direct targeting of an antigen, a monoclonal antibody is best suited, as there is only one copy of antibody for which there is a known affinity to the antigen. This reduces variability between tests.

2.5.2 Bioconjugation of antibodies

In order to target antigens on cells, a bioconjugation method was developed to produce efficient antibody attachment to the surface of the nanoparticle. There are many regions on an antibody which can be used to attach to the nanoparticle and the most commonly used include:

1. *Amine group regions*. These are found on the lysine residues of the antibody and are found dispersed on all chains of the antibody (see Fig 2.7). They are the most abundant groups that are available for modification on the antibody [20]. There are a number of these groups found on the antigen binding region and because of this, there is a possibility that the binding efficiency of the antibody could be reduced. 2. *Disulfide bond regions*. These are found on cysteine residues and the disulphide bonds are a crucial part of the structure of the antibody, mainly the hinge region, which holds the two halves of the antibody together. Modifying the disulfide bonds in the cysteine residues could result in a conformational change to the antibody, causing some regions of the antibody to fold incorrectly and thus cause it to denature [20]. 3. *Carbohydrate regions*. These are found mostly on the constant region of the antibody and can be oxidised to make aldehyde groups active for conjugation. This type of coupling does not interfere with the antigen binding sites because of its location on the antibody. However, this process has more steps than amine conjugation because the carbohydrate regions first need to be oxidised [20].
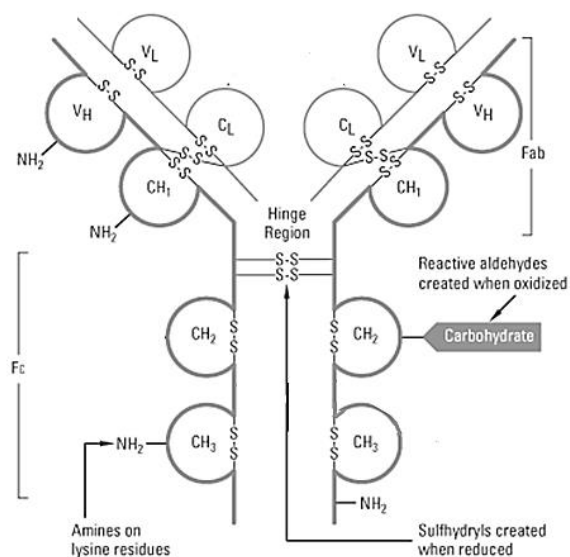
Fig 2.7: Binding groups available on an antibody adapted from [20].

The amine groups were chosen for modification to bind to NPs as the disulphide bond conjugation can cause denaturation and the carbohydrate conjugation is more complicated. Although there is a possibility that the antigen binding region could be blocked by the orientation in which it binds to the surface, there will be a large number of antibodies on the surface therefore, statistically, there will be some that will be correctly orientated and available to bind to antigens.

2.5.3 Primary vs secondary antibody detection systems

Secondary antibody systems can be more sensitive than direct binding primary antibody systems because it is possible for more than one secondary antibody to bind to the primary antibody target, see Fig 2.8 for schematic representation of antibody staining methods. Using a secondary antibody system means that the primary antibody is not modified through bioconjugation with a label, leaving it unhindered, pristine and most importantly, all binding sites open for interaction with target antigen. There are two types of secondary staining detection systems. The first is an antibody-antibody system, where a primary unlabelled antibody is used to bind to a specific antigen and then a secondary labelled antibody is introduced which is specific to the primary antibody, and binds to Fc regions of the primary antibody. The second system is a biotin-avidin detection system. In this case, an unlabelled biotinylated antibody targets a protein and then an avidin modified labelled antibody is introduced that will bind directly to the biotin on the primary antibody.
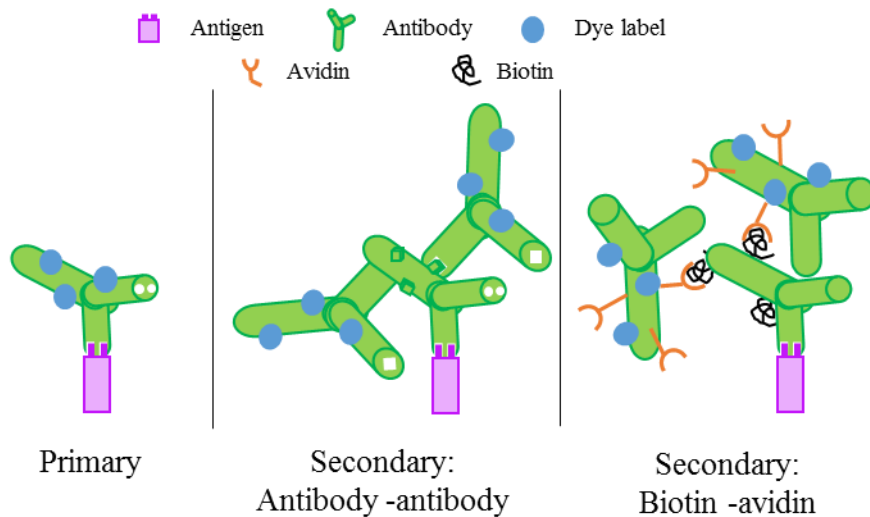
Fig 2.8: Schematic of cell staining methods using primary antibody, secondary antibody – antibody or secondary biotin – avidin methods.

.

2.6 Blood cells and circulating tumour cells

In the human body, there are many types of cells, that carry out various functions. In the blood, there are between 4.2-6.1 million red blood cells per microliter and 5-10 thousand white blood cells per microliter [21]. Circulating tumour cells (CTCs) are cells that have dissociated from a primary cancer tumour somewhere in the body and have entered either the blood stream or lymphatic system. They are the cause of metastasis in cancer patients, as mentioned earlier. This particular cell population is extremely rare in the blood in terms of numbers among patients, especially at early stage. It has been estimated that there are 1 to 100 circulating tumour cells (CTCs) in 10^9 blood cells [22]. It is clear there are a substantial number of cells from which CTCs must be differentiated. Efforts have been made to detect CTCs based on physical parameters such as size and density on microfluidic platforms but as these parameters are not so distinct from normal cells, the separation has not been unambiguous [23-25]. One way to distinguish CTCs from blood cells is through their surface markers. As these cells originated from the epithelium, they exhibit surface antigens that are related to this area of the body and express markers that are not present on blood cells. This largely includes the expression of epithelial cell adhesion molecule (EpCAM), cytokines or e-cadherin [26]. Some CTCs express a surface protein, EpCAM, which is a 40 kDa glycoprotein antigen (one made of both oligosaccharides (glycans) and a protein) and is also known as cluster of

differentiation (CD) 326. Epithelial originating CTCs also express particular cytokines, which are intermediate filaments for cytoskeletal structure, and include K8, K18 and K19. E-cadherin is a protein that supports epithelial structural adhesion and prevents it from detaching. It is also used for the identification of non-blood cells [26]. A combination of these markers in conjunction with markers to identify white blood cells are used to correctly isolate and identify CTCs. This can be done using immunomagnetics and fluorescence recognition. An FDA approved detection platform called CellSearch (Menarini Silicon Biosystems Inc, CA, USA) uses a combination of these principles to detect CTCs in patient whole blood [27]. Anti-EpCAM magnetic beads are used to select EpCAM positive cells, which are then stained with cytokeratin, anti-CD45 and DAPI stains to verify if CTCs have been captured. Some microfluidic platforms have been developed with a similar workflow as the CellSearch by using immunomagnetic and fluorescence staining of cells to achieve the same outcome by taking advantage of surface markers [28]. In the work presented in this thesis, for simplicity and proof of concept of tagging CTCs with NPs, EpCAM was chosen as the targeting surface receptor on a model CTC line.

Monoclonal antibodies have been engineered specifically to the EpCAM antigen and are commercially available to adhere to EpCAM positive cells. For this project, two cell lines were used to investigate a system of detection. One cell line was EpCAM positive and the other EpCAM negative. The EpCAM positive cells that were used for this project were MCF-7 and LNCaP cells which are a breast cancer and prostate cancer adenocarcinoma. The EpCAM negative cells used were HeLa, a cervical cancer cell line that does not express EpCAM, and LNCaP, a normal, non-cancerous, prostate tissue cell line. All cell lines were grown by adherent growth methods throughout this work.

2.7 Nanoparticle synthesis

Silica nanoparticles can be synthesised mainly by two methods; the Stöber method and the microemulsion method. The Stöber method, first published in 1968, involves the hydrolysis of alkyl silicates, usually tetraethyl orthosilicate (TEOS) with ethanol, and a condensation reaction occurs in the presence of a catalyst to form monodisperse silica nanoparticles in the range of 50nm - 2µm [29]. The growth mechanism has been investigated by Masalov et al. and it was concluded that the silica nanoparticles form

through aggregation of primary particles, ~5nm in size, and when there is not enough polymer left to form these primary particles, the polymer forms a thin coat around the aggregated particles to produce a smooth silica particle for particles up to ~160nm in size, see Fig 2.9 [30]. Upon the addition of further amounts of TEOS, larger particles form and coat the smooth, <160nm, particle. This repeats itself upon the addition of more TEOS until the particles reach micron size.
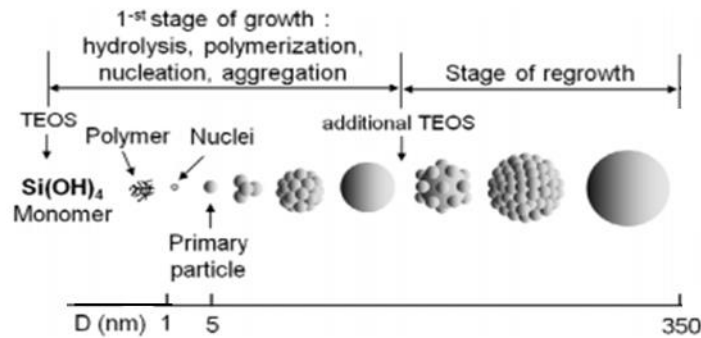
Fig 2.9: Growth of silica nanoparticles via Stöber method adapted from [30]

The reverse microemulsion method of producing silica nanoparticles is a system that can produce particles in the range of 20-500nm and entails the use of water in a solvent, such as cyclohexane or hexane, with a silicate and a number of surfactants in order to control the size and shape of the nanoparticles [31,32]. In this method, the hydrolysis of silica and the condensation reactions occur at the interface between the water and oil phase. This water and oil phase consists of water micelles that are surrounded by surfactant in an oil medium.

2.7.1 Dye doped nanoparticles

Hydrophilic dye can be encapsulated in silica NPs using the reverse microemulsion method when added to the water phase of this method. However, when using this system to produce dye-doped nanoparticles with hydrophobic dyes, it can fail to form proper micelles, due to aggregation of the dye and cause insufficient dye loading of the particles [33]. Previous work has shown that it is possible to incorporate hydrophobic dyes into nanoparticles using the reverse microemulsion method by first conjugating an N-hydroxysuccinimide (NHS) ester dye molecule to a silane (aminopropyltrimethoxysilane also known as APTMS) and using an additional negatively charged surfactant such as dioctyl sulfosuccinate sodium salt (AOT) alongside nonionic surfactants like polyoxyethylene (5) nonylphenylether (NP-5) to

form micelles (see Fig 2.10 below for a schematic representation of how dye-doped nanoparticles form) [33,34]. This method is known as a quaternary method as it involves a combination of four solvents and/or surfactants; APTMS, cyclohexane, NP-5 and AOT. This was the formulation for nanoparticle synthesis used throughout this thesis to incorporate Cyanine5 hydrophobic dye into nanoparticles and is referred to as the quaternary method. If there were a combination of three solvents and surfactants, this would be a tertiary system.
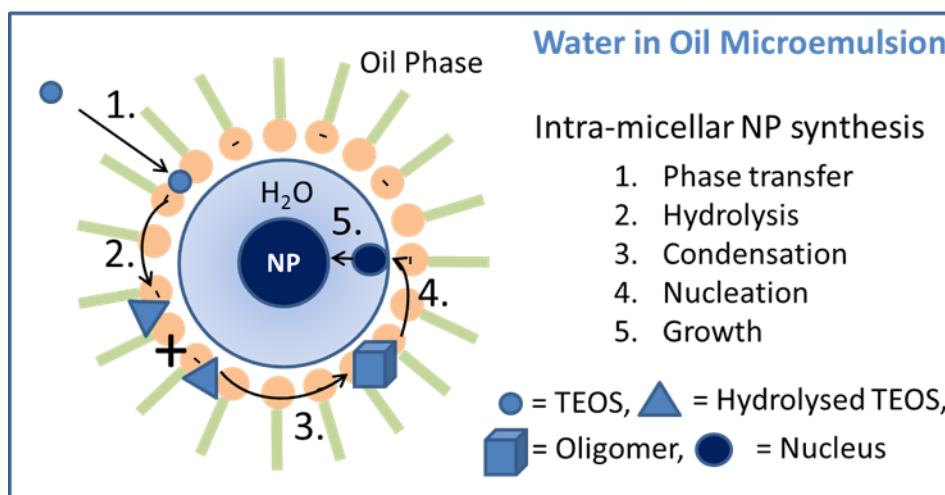
Fig 2.10: Dye-doped silica nanoparticle synthesis method with dye-conjugated TEOS. © Robert Nooney 2015. Reproduced with permission.

2.7.2 Surface functionalisation design considerations

Surface compatibility for bioconjugation is necessary for targeted cell staining. Silica is readily able to bind and interact with proteins without the need for functionalization of the nanoparticles. This passive adsorption of protein on the nanoparticle surface has been analysed and discussed by a number of groups [35-39]. This inherent affinity of the proteins and silica is not a strong bond and as such is unsuitable for use in antigen targeting where the antibody to nanoparticle bond should be strong enough to bind the particle to the analyte. Covalently conjugating the antibody to the surface circumvents this. A typical approach is to attach a layer of amine groups through hydrolysis to the silica surface of the nanoparticles. This is done so that the surface is readily available for further modification. There are a wide range of molecules available to be used as linkers between nanoparticle and protein but they mainly fall into two sub headings: linear or branched linkers. An investigation carried out by Gubala et al. showed that branched linker molecules, or multivalent linkers, as referred to in the paper, are more efficient for protein binding and they also increased the particle stability [40]. For this

reason, an 8-arm PEG linker was used in the nanoparticle synthesis step to bind to the surface after amine functionalisation (see Fig 2.11 below, with modified NHS ester end groups). The NHS ester groups allow for reactivity of the PEG molecule to amine groups on an antibody.
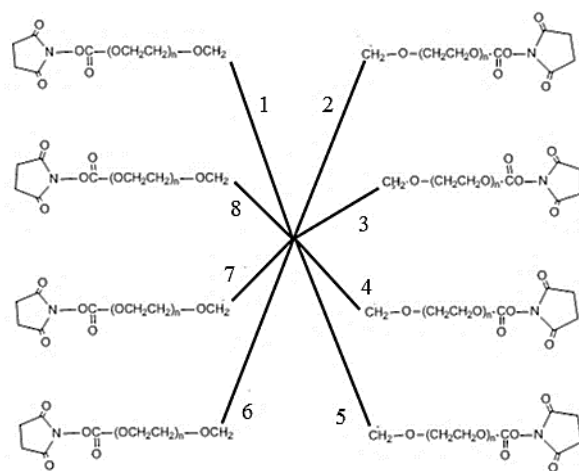
Fig 2.11: 8-arm PEG multivalent linker molecule adapted from [41].

One of the challenges in using NPs for targeted cell imaging or staining is high non-specific interactions between the cells and particles followed by endocytosis. The internalisation of NPs by cells can be useful for investigating pH, toxicity and drug delivery applications [42-44]; however, for the work presented in this thesis, it is imperative that the nanoparticles do not get adsorbed or up taken non-specifically. Key parameters to prevent non-specific binding include a negative zeta potential, polyethylene glycol (PEG) functionalisation and protein stabilisation of NPs [37,45,46]. It has been reported that, to prevent NPs from crossing the cell membrane, the NPs need to be negatively charged because phospholipid membranes of the cells are also negatively charged leading to electrostatic repulsion, whereas positively charged NPs are more regularly up taken [45,47]. PEG has been used to increase circulation times of NPs in vivo due to reduction in aggregation of opsonins and proteins from blood serum on the surface of NPs that cause endocytosis [48,49]. In a detailed study, Rampazzo et al. investigated the use of PEG molecules on the surface of silica NPs with different charged functional groups to reduce particle up take in cells [49,50]. Results indicated that PEG only nanoparticles had reduced up take in the cell compared to positively charged amino-PEG-NPs, but that overall the highly negative carbo-PEG-NPs were least

effective at entering the cell membrane, emphasising the point that the overall negative charge of the NP helps to prevent its endocytosis. It has been shown that proteins help to stabilise NPs by creating a protein layer around the particles, also known as a protein corona, that helps to prevent aggregation sterically in protein rich sample media such as serum [37,46,51]. Lesniak et al. have shown that, without serum, NPs are internalised by cells much more effectively because of the lack of protein in solution, and similarly Kim et al. have shown that at low concentrations of protein, NP uptake is greater than at higher concentrations [61,63].

NP size is another aspect which must be considered when using silica NPs before experimentation for biomedical applications with cells. A great deal of research has been carried out recently in relation to this, particularly for cell cytoxicity in the presence of different size silica nanoparticles [52-55]. Nanoparticles of different sizes, ranging from 20-200nm, were analysed in the presence of three different cell types at different time points [52]. It appeared that 20,60 and 200nm silica nanoparticles at a concentration of 100µg/mL or less are not cytotoxic and do not induce cell death. They found that 20nm particles over 24 hours caused damage to intracellular structures upon uptake, that the 60nm NPs were uptaken the most over this time frame but the 200nm NPs that were endocytosed resided in the mitochondria [52]. The high particle uptake for 60nm size NPs agreed with another study that found similar results for this size particle [54]. 60nm dye-doped silica NPs had previously been developed in the optical sensors group at Dublin City University. Their synthesis was a well understood process and they had been used sucessfully with immunoassays. For this thesis, part of the investigation and exploratory work was to determine if they could be used for surface antigen detection on cells despite known particle uptake by cells at this size nanoparticle.

Taking all these factors into consideration, a ~60nm negatively charged PEGylated NP, that is colloidally stable due to protein adsorption, for specific targetting of EpCAM markers on the surface of the MCF-7 cells was developed.

2.8 Nanoparticles for cell staining and flow cytometry - state of the art

Cell imaging and flow cytometry has been used in the field of biomedical diagnostics for decades in relation to the detection of many disease markers and has contributed to the study of histology and oncology. These experiments have been carried out using various fluorescent probes including dyes and nanoparticles for the detection of cancer either targeted or untargeted. These fluorescent probes include but are not limited to: quantum dots [56-58], carbon dots [59,60], polymer dots [61-63] and dye doped silica nanoparticles [64,65].

Dye-doped silica nanoparticles have been used for biomedical applications such as cell imaging and immunoassays previously [64-66]. They have advantages over other nanoparticles due to their high dye doping ability, biocompatibility and relative non-toxicity [67]. Their easily functionalised surface allows for the conjugation of bio recognition units to the NP such as antibodies and DNA which can transform the NPs into biosensors [68,69]. It has been demonstrated that the NPs can encapsulate a versatile range of dyes including hydrophobic and hydrophilic dyes such as fluorescein isothiocyanate (FITC), tris(bipyridine)ruthenium(II) chloride (Rubpy), Cy5[TM] and AlexaFluor[®]750 to name but a few [68-74]. These NPs can be used to detect pH, oxygen, glucose and ion species in cells intracellularly by doping them with metal complexes such as Ruthenium complexes or pH sensitive dyes [64,75,76]. However, the brightness and photon emission of the NPs is limited by a number of factors that were mentioned previously in this chapter in section 2.2 such as the quantum yield of the dye and the effects of Forster resonance energy transfer between dye molecules in close proximity. Despite this, enhancements of over two orders of magnitude have been achieved when comparing free dye to NPs that have encapsulated the same dye [34,68].

In sections 2.8.1-2.8.3, specific and non-specific targeting of cells using dye doped silica nanoparticles in cell imaging and flow cytometry is discussed. Primarily, these NPs were made using the microemulsion method, although some NPs synthesised using the Stöber method are included as well. For cell staining using NPs, there are usually two types mentioned: specific and non-specific staining. The more common and easiest to implement is non-specific staining. In this case, cells are incubated with NPs that have no biological recognition receptors on their surface but are either completely bare or

have the addition of some functional groups on their surface such as amine, thiol etc. Non-targeted cell staining can also be useful in determining if surface charge or certain surface groups on the NP induce a greater/lesser uptake in the cell or are toxic to it. However, the real challenge lies within targeted NP staining of cells and NP stability. Some of these factors which must be considered are NP stability in cell media, correct design of antibody-nanoparticle conjugation and NPs entering through the cell membrane through cell mediated pathways to name just a few. Reduction of non-specific binding is an important step in optimisation of the use of the NPs as cellular labels and also as labels for fluorescence-based immunoassays and DNA assays where low limits of detection (LOD) and a high signal to noise ratio are required.

2.8.1 Untargeted silica nanoparticle cell staining

It is important to know the fate of the NPs once incubated with cells, for example, in cell staining when detecting surface markers, to ensure that the targeting antibody is functional and not endocytosed by the cell, or in drug delivery, if the drugs are targeting a specific cell organelle. This can be useful when investigating the toxicity of the nanoparticles to the cells in question. A study carried out by Al-Rawi et al. showed that 70nm silica NPs labelled with FITC end up in the lysosomes of HeLa cells. However larger particles of 200-500nm diameter were located in endosomal compartments within the cytosol of the cell due to the time frame of the study [77]. In general, particles will eventually migrate to the lysosome of a cell [78]. They also reported that the 70nm particles were toxic to the HeLa cells without the presence of serum.

Different microscopy methods can be used to identify where the NPs are located. For example, Ye et al. used a transmission electron microscopy (TEM) method for the investigation of 50nm unfunctionalised silica NPs across the blood-brain and intestine-endothelial barriers [79]. In another study, Lesniak et al. used both TEM and confocal analysis to determine the fate of dye-doped unfunctionalised silica NPs in A549, adenocarcinomic human alveolar basal epithelial cells [80].

2.8.2 Targeted silica nanoparticles for cell staining

A number of papers have been published in which is described the surface functionalisation of dye doped silica NPs with a bio-recognition structure, such as an antibody, and used to successfully identify a target protein on a cell population. Below are a few examples of these studies.

Woolley et al. used anti-CD41 conjugated nanoparticles to image platelets [81]. They doped NIR-664 dye into silica particles using the reverse microemulsion method and could image the surface of the platelets. They achieved good specificity when compared with either bare NPs or IgG conjugated NPs incubation with platelets. They confirmed the location of the NPs using a combination of scanning electron microscopy and confocal microscopy. A study by He et al. was carried out to investigate two sets of NPs prepared by microemulsion method, either anti-carcinoembryonic antigen (CEA) FITC NPs or anti-CK19 Rubpy doped NPs. They were developed to detect MGC-803 gastric cancer cells [82]. Both antibodies can detect a different marker for gastric cancer cells and, using the two dye-doped NP labels, they could use different fluorescent channels in confocal microscopy to image the cells. They also obtained xenograft primary gastric cancer tumour cells from mice and showed that the NPs could successfully label these cells. Another study was carried out in which HepG liver cancer cells were recognised using FITC doped NPs that were synthesised using the reverse microemulsion method [83]. Using anti-HAb18 monoclonal antibody that was conjugated to the NPs, the liver cancer cells were distinguished with good specificity. Another study by Tiernan et al. investigated NIR664 doped silica NPs synthesised using the microemulsion method for targeting colorectal cancer cells [84]. They conjugated anti-CEA antibody via a branched dendrimer linker molecule to the NPs. They were successful in identifying LS174T, LoVo and HCT116 colorectal cancer cell lines using the NPs in confocal microscopy applications and showed that the particles could also be used to detect xenografts of colorectal tumours in mice in vivo.

Some groups have carried out work using dye-doped silica nanoparticles for the identification of a single protein on a cell line within a mixed cell system [69,85]. Tao et al. identified EpCAM positive colo205 colon cancer cells from EpCAM negative sw480 colon cancer cells using Rubpy doped silica NPs that were synthesised via the microemulsion method [69]. First, they used single cell line populations in cell imaging and flow cytometry to ensure specificity of the NPs. They then used a mixed cell population of the EpCAM positive and negative cell lines together and visualised this mixed cell population by microscope, but not by flow cytometry. Another mixed cell population study, by Peng et al., has looked at the detection of BEL-7404 liver cancer cells from MCF-7 cells that were transfected with green fluorescent protein (GFP). They spiked the BEL-7404 cells into MCF-7s and incubated them with galactose conjugated

Rubpy-doped NPs, synthesised by the microemulsion method. Initially the cells were analysed using confocal microscopy and after the NPs displayed specificity, this was followed by spiking the liver cancer cells in to the MCF-7s at a range of different ratios. The mixed cell populations were then monitored via flow cytometry where they achieved high specificity and were able to detect the liver cancer cells with the NPs down to 1% of cell population [85]. In this same paper, they also looked at the detection of the liver cancer cells from white blood cells. They detected the BEL-7404 liver cancer cells using the same galactose Rubpy doped silica NPs as previous and, via confocal laser microscopy, could distinguished them from white blood cells [85]. They did not carry out flow cytometry on these mixed cell samples.

2.8.3 Targeted silica nanoparticles for flow cytometry.

Another application of dye-doped silica NPs is for use with flow cytometry. As the two methods of detection, cell staining and flow cytometry, largely overlap in studies, below are some examples of work that solely relate to flow cytometry.

Estevez et al. utilised a biotin-avidin secondary labelling system with FITC doped silica NPs that were made via the Stöber method for detection of cells. Using a sgc8-polyT10-biotin aptamer that was allowed to incubate with the cells first and introducing neutravidin conjugated NPs, the NPs showed large specificity to CEM cells, also known as human acute lymphoblastic leukaemia cells, compared to the Ramos human Burkitt's lymphoma control cell line using flow cytometry [68]. They repeated these experiments using confocal microscopy to image the cells and also stained the same cells with Rubpy NPs, synthesised using the microemulsion method, which showed good specificity for the cell line. They then used a mixed cell population consisting of CEM cells spiked into Ramos cells at different percentages and, after incubation with FITC NPs, detected them using flow cytometry. More flow cytometry analysis was carried out using an antibody-antibody secondary system where this time biotinylated anti-PTK7 was first incubated with cells and then neutravidin coated FITC or Rubpy doped NPs were added. They achieved a 100-fold increase in signal compared to a primary anti-PTK7 AlexaFluor®488 antibody and this large increase can partly be attributed to comparing a primary antibody system to a more sensitive secondary one.

One group recently published a study on the effect of the orientation of conjugated EpCAM antibodies on Stöber synthesised Cy5 doped NPs in relation to cancer cell

detection. [86]. NPs were first conjugated with protein G, a protein which only allows antibodies to bind via their constant region, thus allowing only one orientation, facing outwards. The NPs were then incubated with anti-EpCAM, to allow binding to the NP, which were used to detect colorectal HK 29 cells through flow cytometry and interestingly found that the orientated NPs were over 10 times more sensitive than anti-EpCAM NPs that were prepared using the commonly used EDC-NHS chemistry.

Yun et al. targeted blood cells to enumerate subsets of leukocytes with FITC doped NPs that have implications for HIV and AIDS monitoring [87]. Using FITC doped silica nanoparticles that were synthesised using the microemulsion method they targeted CD45 and CD4 proteins on the surface of leukocytes. Interestingly, although targeting two proteins, they could detect the second CD4 protein using only one type of dye doped NP. Due to the substantial increase in fluorescence from the additional NPs bound to the second protein they could view this fluorescence increase from only one channel. This was measured on a microchip based flow cytometer that was built in house and used with a diode laser.

It appears that dye-doped silica nanoparticles for the detection of CTCs from blood cells on a flow cytometry system has not been carried out previously.

2.9 Grating coupled surface plasmon resonance

There has been much emphasis in the literature on high resolution imaging of cells using confocal microscopes, stimulated emission depletion microscopy (STED) and other complex imaging systems [88] and some work has been reported on cell imaging using plasmonic substrates [89]. This brief feasibility study focused on assessing the suitability of plasmon active grating structures for cell imaging. These substrates were developed and fabricated as part of a separate project and provided here for this exploratory imaging project. More details on the development of these substrates can be found in a paper published earlier this year [90].

2.9.1 Principle of plasmonic enhancement of fluorescence

A plasmon is a quantum of plasma oscillation, where a plasma oscillation is the collective oscillation of free electrons in a conducting material such as a metal. A plasmon is analogous to a photon, which is a quantum of light as alluded to earlier.

Surface plasmon resonance (SPR) occurs under certain conditions when light interacts with metal at a particular wavelength which resonates with the oscillations of the electrons, hence producing plasmons. Photons interact with the plasmons to form surface plasmon polaritons (SPPs), which travel along the dielectric / metal interface. This is the basis of the widely used technique of SPR, a label-free detection technique using, usually, planar gold surfaces on which the molecule to be detected is bound [91-93]. In order to achieve coupling, the momentum of the light must match the momentum of the surface plasmons which can be achieved using Kretschmann or Otto geometry for prism coupled SPR [94,95] or by using metal grating coupling as is used in this thesis.

A localised plasmon occurs when nanoparticles smaller or of similar size to the wavelength of incident light are used to trap or confine the plasmons and prevent them from propagating through the metal / dielectric interface. This can occur when metal nanoparticles are purposely deposited on a surface, such as a prism, or due to the intrinsic random surface roughness of the coated metal. The surface plasmon resonance causes the electric field near the surface to become enhanced due to the oscillating electron density but decays rapidly as a function of distance from the surface. Fluorophores that are within this metal enhanced electric field have enhanced signals and modified excited state lifetimes [96]. This can be explained by the reflected far-field radiation from the fluorophore back on itself which can induce a reduced excited state lifetime and an increase in the radiative decay rate thus producing enhanced fluorescence [97]. This effect depends on many parameters e.g. size, shape and composition of the nanostructure and dye-metal separation [98-101]. Incident light can be efficiently coupled into a metal grating to excite SPPs, which, in turn, can interact with fluorescent molecules to produce enhanced fluorescence. This principle is used here to explore grating enhanced cell imaging where the cells are bound to a plasmonic grating substrate which is mounted on a standard inverted epifluorescence microscope

2.10 Summary

This chapter discussed the theory behind the photo physical phenomena that were used in this thesis and detailed the rationale behind choice of nanoparticle design during synthesis steps. Also included in this chapter was a state-of-the-art on current fluorescence nanoparticles used for cell imaging and staining.

2.11 References

[1] S. Eaton-Magaña, C.M. Breeding, An introduction to photoluminescence spectroscopy for diamond and its applications in gemology, Gems Gemol. 52 (2016) 2-17.

[2] J. Franck, Elementary processes of photochemical reactions, Transactions of the Faraday Society. 21 (1926) 536-542.

[3] E. Condon, A theory of intensity distribution in band systems, Physical Review. 28 (1926) 1182-1201.

[4] J.R. Lakowicz, Introduction to Fluorescence, in: J.R. Lakowicz (Ed.), Principles of Fluorescence Spectroscopy, Third ed., Springer, United States of America, 2010, pp. 1-24.

[5] E.J. Bowen, A. Norton, The quenching of fluorescence in solution, Transactions of the Faraday Society. 35 (1939) 44-48.

[6] C. Eggeling, J. Widengren, R. Rigler, C.A.M. Seidal, Photobleaching of fluorescent dyes under conitions used for single-molecule detection: evidence of two-step photolysis. (1998) *Anal Chem* 70 2651-2659, Analytical Chemistry. 70 (1998) 2651-2659.

[7] F. Schaufele, I. Demarco, R.N. Day, FRET Imaging in the Wide-Field Microscope, in: Anonymous Molecular Imaging, 2005, pp. 72-94.

[8] Z.-. Li, W. Cai, X. Chen, Semiconductor quantum dots for in Vivo, J. Nanosci. Nanotechnol. 7 (2007) 2567-2581.

[9] ThermoFisher Scientific, The Molecular Probes Handbook, Spectral Data for B-PE, R-PE and APC Table 6.2., 2017 (2015).

[10] Atto-Tec, Fluorescent labels and dyes, catalogue 2009/2010, 2017 (2009).

[11] Dyomics, Dyomics, Red excitation, DY-647P1, 2017 (2015).

[12] ThermoFisher Scientific, The Molecular Probes Handbook, Fluorescence quantum yields and lifetimes for Alexa Fluor dyes, 2017 (2016).

[13] G. Lumiprobe, Cyanine5 NHS ester, 2015 (2015).

[14] B. Biosciences, Relative Fluorochrome Brightness, 2016 (2014).

[15] B. Biosciences, BD Horizon Brilliant™ Dyes, 2016 (2015).

[16] Larryisgood, Zeta Potential for a particle in dispersion medium, 2016 (2011).

[17] Beckman Coulter, User's Manual Delsa™Nano Submicron Particle Size and Zeta Potentia, 2015 (2011).

[18] Y. tambe, Immunoglobulin basic unit, 2015 (2007).

[19] C.A. Janeway, P.J. Travers, M. Walport, M.J. Shlomchik, Chapter 3The structure of a typical antibody molecule, in: Anonymous Immunobiology: The Immune System in Health and Disease, 5th ed., Garland Science, New York, 2001.

[20] ThermoFisher Scientific, Antibody labelling and immobilisation sites, 2017 (2014).

[21] American Cancer Society, Understanding Your Lab Test Results, 2017 (2016).

[22] H.W. Hou, M.E. Warkiani, B.L. Khoo, Z.R. Li, R.A. Soo, D.S.-. Tan, W.-. Lim, J. Han, A.A.S. Bhagat, C.T. Lim, Isolation and retrieval of circulating tumor cells using centrifugal forces, Sci. Rep. 3 (2013).

[23] V. Müller, N. Stahmann, S. Riethdorf, T. Rau, T. Zabel, A. Goetz, F. Jänicke, K. Pantel, Circulating tumor cells in breast cancer: Correlation to bone marrow micrometastases, heterogeneous response to systemic therapy and low proliferative activity, Clin. Cancer Res. 11 (2005) 3678-3685.

[24] D. Di Carlo, Inertial microfluidics, Lab Chip Miniaturisation Chem. Biol. 9 (2009) 3038-3046.

[25] G. Vona, A. Sabile, M. Louha, V. Sitruk, S. Romana, K. Schutze, F. Capron, D. Franco, M. Pazzagli, M. Vekemans, B. Lacour, C. Brechot, P. Paterlini-Brechot, Isolation by size of epithelial tumor cells: A new method for the immunomorphological and molecular characterization of circulating tumor cells, Am. J. Pathol. 156 (2000) 57-63.

[26] Barriere, G., Fici, P., Gallerani, G., Fabbri, F., Zoli, W., Rigaud,M., Circulating tumor cells and epithelial, mesenchymal and stemness markers: characterization of cell subpopulations, Annals of Translational Medicine. 2 (2014).

[27] CellSearch, How does the CellSearch system work? 2017 (2017).

[28] D. Kirby, M. Glynn, G. Kijanka, J. Ducrée, Rapid and cost-efficient enumeration of rare cancer cells from whole blood by low-loss centrifugo-magnetophoretic purification under stopped-flow conditions, Cytometry Part A. 87 (2015) 74-80.

[29] W. Stober, A. Fink, E. Bohn, Controlled growth of monodisperse silica spheres in the micron size range, Journal of colloid and interface science. 26 (1968) 62-69.

[30] V.M. Masalov, N.S. Sukhinina, E.A. Kudrenko, G.A. Emelchenko, Mechanism of formation and nanostructure of Stöber silica particles, Nanotechnology. 22 (2011).

[31] K. Osseo-Asare, F.J. Arriagada, Preparation of SiO2 nanoparticles in a non-ionic reverse micellar system, Colloids and Surfaces. 50 (1990) 321-339.

[32] F.J. Arriagada, K. Osseo-Asare, Synthesis of nanosize silica in a nonionic water-in-oil microemulsion: Effects of the water/surfactant molar ratio and ammonia concentration, J. Colloid Interface Sci. 211 (1999) 210-220.

[33] R. Nooney, C. O'Connell, S. Roy, K. Boland, G. Keegan, S. Kelleher, S. Daniels, C. McDonagh, Synthesis and characterisation of far-red fluorescent cyanine dye doped silica nanoparticles using a modified microemulsion method for application in bioassays, Sens Actuators, B Chem. 221 (2015) 420-479.

[34] R.I. Nooney, C.M.N. McCahey, O. Stranik, X. Le Guevel, C. McDonagh, B.D. MacCraith, Experimental and theoretical studies of the optimisation of fluorescence from near-infrared dye-doped silica nanoparticles, Anal. Bioanal. Chem. 393 (2009) 1143-1149.

[35] A.E. Nel, L. Mädler, D. Velegol, T. Xia, E.M.V. Hoek, P. Somasundaran, F. Klaessig, V. Castranova, M. Thompson, Understanding biophysicochemical interactions at the nano-bio interface, Nat. Mater. 8 (2009) 543-557.

[36] D. Walczyk, F.B. Bombelli, M.P. Monopoli, I. Lynch, K.A. Dawson, What the cell "sees" in bionanoscience, J. Am. Chem. Soc. 132 (2010) 5761-5768.

[37] M.P. Monopoli, D. Walczyk, A. Campbell, G. Elia, I. Lynch, F. Baldelli Bombelli, K.A. Dawson, Physical-Chemical aspects of protein corona: Relevance to in vitro and in vivo biological impacts of nanoparticles, J. Am. Chem. Soc. 133 (2011) 2525-2534.

[38] X.-. Xia, N.A. Monteiro-Riviere, J.E. Riviere, An index for characterization of nanomaterials in biological systems, Nat. Nanotechnol. 5 (2010) 671-675.

[39] M.P. Monopoli, F.B. Bombelli, K.A. Dawson, Nanobiotechnology: Nanoparticle coronas take shape, Nat. Nanotechnol. 6 (2011) 11-12.

[40] V. Gubala, X. Le Guevel, R. Nooney, D.E. Williams, B. MacCraith, A comparison of mono and multivalent linkers and their effect on the colloidal stability of nanoparticle and immunoassays performance, Talanta. 81 (2010) 1833-1839.

[41] Nanocs, PEG derivatives, Multi-arm PEG derivatives, 2017 (2014).

[42] B. Korzeniowska, R. Woolley, J. DeCourcey, D. Wencel, C.E. Loscher, C. McDonagh, Intracellular pH-sensing using core/shell silica nanoparticles, J. Biomed. Nanotechnol. 10 (2014) 1336-1345.

[43] Y. Gao, S. Gu, Y. Zhang, X. Xie, T. Yu, Y. Lu, Y. Zhu, W. Chen, H. Zhang, H. Dong, P.J. Sinko, L. Jia, The Architecture and Function of Monoclonal Antibody-Functionalized Mesoporous Silica Nanoparticles Loaded with Mifepristone: Repurposing Abortifacient for Cancer Metastatic Chemoprevention, Small. 12 (2016) 2595-2608.

[44] W. Fan, B. Shen, W. Bu, F. Chen, Q. He, K. Zhao, S. Zhang, L. Zhou, W. Peng, Q. Xiao, D. Ni, J. Liu, J. Shi, A smart upconversion-based mesoporous silica nanotheranostic system for synergetic chemo-/radio-/photodynamic therapy and simultaneous MR/UCL imaging, Biomaterials. 35 (2014) 8992-9002.

[45] O.S. Wolfbeis, An overview of nanoparticles commonly used in fluorescent bioimaging, Chem. Soc. Rev. 44 (2015) 4743-4768.

[46] M. Lundqvist, J. Stigler, G. Elia, I. Lynch, T. Cedervall, K.A. Dawson, Nanoparticle Size and Surface Properties Determine the Protein Corona with Possible Implications for Biological Impacts, Proc. Natl. Acad. Sci. U. S. A. 105 (2008) 14265-14270.

[47] S. Jambhrunkar, Z. Qu, A. Popat, J. Yang, O. Noonan, L. Acauan, Y. Ahmad Nor, C. Yu, S. Karmakar, Effect of surface functionality of silica nanoparticles on cellular uptake and cytotoxicity, Mol. Pharm. 11 (2014) 3642-3655.

[48] M.I. Papisov, Theoretical considerations of RES-avoiding liposomes: Molecular mechanics and chemistry of liposome interactions, Adv. Drug Deliv. Rev. 32 (1998) 119-138.

[49] V.C.F. Mosqueira, P. Legrand, R. Gref, B. Heurtault, M. Appel, G. Barratt, Interactions between a macrophage cell line (J774A1) and surface-modified Poly(D,L-lactide) nanocapsules bearing poly(ethylene glycol), J. Drug Targeting. 7 (1999) 65-78.

[50] E. Rampazzo, R. Voltan, L. Petrizza, N. Zaccheroni, L. Prodi, F. Casciano, G. Zauli, P. Secchiero, Proper design of silica nanoparticles combines high brightness, lack of cytotoxicity and efficient cell endocytosis, Nanoscale. 5 (2013) 7897-7905.

[51] T. Cedervall, I. Lynch, S. Lindman, T. Berggård, E. Thulin, H. Nilsson, K.A. Dawson, S. Linse, Understanding the Nanoparticle: Protein Corona Using Methods to Quantify Exchange Rates and Affinities of Proteins for Nanoparticles, Proc. Natl. Acad. Sci. U. S. A. 104 (2007) 2050-2055.

[52] I.-. Kim, E. Joachim, H. Choi, K. Kim, Toxicity of silica nanoparticles depends on size, dose, and cell type, Nanomed. Nanotechnol. Biol. Med. 11 (2015) 1407-1416.

[53] C.A. Deforest, B.D. Polizzotti, K.S. Anseth, Sequential click reactions for synthesizing and patterning three-dimensional cell microenvironments, Nat. Mater. 8 (2009) 659-664.

[54] A.E. Nel, L. Mädler, D. Velegol, T. Xia, E.M.V. Hoek, P. Somasundaran, F. Klaessig, V. Castranova, M. Thompson, Understanding biophysicochemical interactions at the nano-bio interface, Nat. Mater. 8 (2009) 543-557.

[55] F. Lu, S.-. Wu, Y. Hung, C.-. Mou, Size effect on cell uptake in well-suspended, uniform mesoporous silica nanoparticles, Small. 5 (2009) 1408-1413.

[56] S. Barua, K. Rege, Cancer-cell-phenotype-dependent differential intracellular trafficking of unconjugated quantum dots, Small. 5 (2009) 370-376.

[57] M.Z. Fahmi, J.-. Chang, Forming double layer-encapsulated quantum dots for bio-imaging and cell targeting, Nanoscale. 5 (2013) 1517-1528.

[58] K.E. Sapsford, T. Pons, I.L. Medintz, H. Mattoussi, Biosensing with luminescent semiconductor quantum dots, Sensors. 6 (2006) 925-953.

[59] L. Cao, X. Wang, M.J. Meziani, F. Lu, H. Wang, P.G. Luo, Y. Lin, B.A. Harruff, L.M. Veca, D. Murray, S.-. Xie, Y.-. Sun, Carbon dots for multiphoton bioimaging, J. Am. Chem. Soc. 129 (2007) 11318-11319.

[60] N. Puvvada, B.N.P. Kumar, S. Konar, H. Kalita, M. Mandal, A. Pathak, Synthesis of biocompatible multicolor luminescent carbon dots for bioimaging applications, Sci. Technol. Adv. Mater. 13 (2012).

[61] C. Wu, B. Bull, C. Szymanski, K. Christensen, J. McNeill, Multicolor conjugated polymer dots for biological fluorescence imaging, ACS Nano. 2 (2008) 2415-2423.

[62] C. Wu, S.J. Hansen, Q. Hou, J. Yu, M. Zeigler, Y. Jin, D.R. Burnham, J.D. McNeill, J.M. Olson, D.T. Chiu, Design of highly emissive polymer dot bioconjugates for in vivo tumor targeting, Angew. Chem. Int. Ed. 50 (2011) 3430-3434.

[63] F. Ye, C. Wu, Y. Jin, M. Wang, Y.-. Chan, J. Yu, W. Sun, S. Hayden, D.T. Chiu, A compact and highly fluorescent orange-emitting polymer dot for specific subcellular imaging, Chem. Commun. 48 (2012) 1778-1780.

[64] B. Korzeniowska, R. Nooney, D. Wencel, C. McDonagh, Silica nanoparticles for cell imaging and intracellular sensing, Nanotechnology. 24 (2013).

[65] W. Arap, R. Pasqualini, M. Montalti, L. Petrizza, L. Prodi, E. Rampazzo, N. Zaccheroni, S. Marchió, Luminescent silica nanoparticles for cancer diagnosis, Curr. Med. Chem. 20 (2013) 2195-2211.

[66] W. Wei, M. Wei, S. Liu, Silica nanoparticles as a carrier for signal amplification, Rev. Anal. Chem. 31 (2012) 163-176.

[67] C. Caltagirone, A. Bettoschi, A. Garau, R. Montis, Silica-based nanoparticles: A versatile tool for the development of efficient imaging agents, Chem. Soc. Rev. 44 (2015) 4645-4671.

[68] M.-. Estévez, M.B. O'Donoghue, X. Chen, W. Tan, Highly fluorescent dye-doped silica nanoparticles increase flow cytometry sensitivity for cancer cell monitoring, Nano. Res. 2 (2009) 448-461.

[69] L. Tao, K. Zhang, Y. Sun, B. Jin, Z. Zhang, K. Yang, Anti-epithelial cell adhesion molecule monoclonal antibody conjugated fluorescent nanoparticle biosensor for sensitive detection of colon cancer cells, Biosens. Bioelectron. 35 (2012) 186-192.

[70] R. Nooney, C. O'Connell, S. Roy, K. Boland, G. Keegan, S. Kelleher, S. Daniels, C. McDonagh, Synthesis and characterisation of far-red fluorescent cyanine dye doped silica nanoparticles using a modified microemulsion method for application in bioassays, Sens Actuators, B Chem. 221 (2015) 420-479.

[71] S. Biffi, L. Petrizza, E. Rampazzo, R. Voltan, M. Sgarzi, C. Garrovo, L. Prodi, L. Andolfi, C. Agnoletto, G. Zauli, P. Secchiero, Multiple dye-doped NIR-emitting silica nanoparticles for both flow cytometry and in vivo imaging, RSC Adv. 4 (2014) 18278-18285.

[72] W. Lian, S.A. Litherland, H. Badrane, W. Tan, D. Wu, H.V. Baker, P.A. Gulig, D.V. Lim, S. Jin, Ultrasensitive detection of biomolecules with fluorescent dye-doped nanoparticles, Anal. Biochem. 334 (2004) 135-144.

[73] A. Burns, H. Ow, U. Wiesner, Fluorescent core-shell silica nanoparticles: Towards "lab on a particle" architectures for nanobiotechnology, Chem. Soc. Rev. 35 (2006) 1028-1042.

[74] E. Herz, H. Ow, D. Bonner, A. Burns, U. Wiesner, Dye structure-optical property correlations in near-infrared fluorescent core-shell silica nanoparticles, J. Mater. Chem. 19 (2009) 6341-6347.

[75] M.J. Ruedas-Rama, J.D. Walters, A. Orte, E.A.H. Hall, Fluorescent nanoparticles for intracellular sensing: A review, Anal. Chim. Acta. 751 (2012) 1-23.

[76] A. Schulz, C. McDonagh, Intracellular sensing and cell diagnostics using fluorescent silica nanoparticles, Soft Matter. 8 (2012) 2579-2585.

[77] M. Al-Rawi, S. Diabaté, C. Weiss, Uptake and intracellular localization of submicron and nano-sized SiO 2 particles in HeLa cells, Arch. Toxicol. 85 (2011) 813-826.

[78] G.M. Cooper, Lysosomes, in: Anonymous The Cell: A Molecular Approach, 2nd ed., Sinauer Associates, Sunderland (MA), 2000.

[79] D. Ye, K.A. Dawson, I. Lynch, A TEM protocol for quality assurance of in vitro cellular barrier models and its application to the assessment of nanoparticle transport mechanisms across barriers, Analyst. 140 (2015) 83-97.

[80] A. Lesniak, F. Fenaroli, M.P. Monopoli, C. Åberg, K.A. Dawson, A. Salvati, Effects of the presence or absence of a protein corona on silica nanoparticle uptake and impact on cells, ACS Nano. 6 (2012) 5845-5857.

[81] R. Woolley, S. Roy, Ú Prendergast, A. Panzera, L. Basabe-Desmonts, D. Kenny, C. McDonagh, From particle to platelet: Optimization of a stable, high brightness fluorescent nanoparticle based cell detection platform, Nanomedicine: Nanotechnology, Biology and Medicine. 9 (2013) 540-549.

[82] X. He, J. Ge, K. Wang, W. Tan, H. Shi, C. He, FSiNPs mediated improved double immunofluorescence staining for gastric cancer cells imaging, Talanta. 76 (2008) 1199-1206.

[83] X. He, J. Duan, K. Wang, W. Tan, X. Lin, C. He, A novel fluorescent label based on organic dye-doped silica nanoparticles for HepG liver cancer cell recognition, J. Nanosci. Nanotechnol. 4 (2004) 585-589.

[84] J.P. Tiernan, N. Ingram, G. Marston, S.L. Perry, J.V. Rushworth, P.L. Coletta, P.A. Millner, D.G. Jayne, T.A. Hughes, CEA-targeted nanoparticles allow specific in vivo fluorescent imaging of colorectal cancer models, Nanomedicine. 10 (2015) 1223-1231.

[85] J. Peng, K. Wang, W. Tan, X. He, C. He, P. Wu, F. Liu, Identification of live liver cancer cells in a mixed cell system using galactose-conjugated fluorescent nanoparticles, Talanta. 71 (2007) 833-840.

[86] K. Treerattrakoon, W. Chanthima, C. Apiwat, T. Dharakul, S. Bamrungsap, Oriented conjugation of antibodies against the epithelial cell adhesion molecule on fluorescently doped silica nanoparticles for flow-cytometric determination and in vivo imaging of EpCAM, a biomarker for colorectal cancer, Microchim. Acta. (2017) 1-10.

[87] H. Yun, H. Bang, J. Min, C. Chung, J.K. Chang, D.-. Han, Simultaneous counting of two subsets of leukocytes using fluorescent silica nanoparticles in a sheathless microchip flow cytometer, Lab Chip Miniaturisation Chem. Biol. 10 (2010) 3243-3254.

[88] B. Turkowyd, D. Virant, U. Endesfelder, From single molecules to life: microscopy at the nanoscale, Anal. Bioanal. Chem. 408 (2016) 6885-6911.

[89] K. Tawa, C. Sasakawa, T. Fujita, K. Kiyosue, C. Hosokawa, J. Nishii, M. Oike, N. Kakinuma, Fluorescence microscopy imaging of cells with a plasmonic dish integrally molded, Jpn. J. Appl. Phys. 55 (2016).

[90] D. Byrne, P. Duggan, C. McDonagh, Controlled surface plasmon enhanced fluorescence from 1D gold gratings via azimuth rotations, Methods Applied Fluorescence. 5 (2017) 015004.

[91] E. Wijaya, C. Lenaerts, S. Maricot, J. Hastanin, S. Habraken, J.-. Vicot, R. Boukherroub, S. Szunerits, Surface plasmon resonance-based bionsensors:From the development of different

SPR structures to novel surface functionalization strategies, Current Opinion in Solid State and Materials Science. 15 (2011) 208-224.

[92] S.P. Yadav, S. Bergqvist, M.L. Doyle, T.A. Neubert, A.P. Yamniuk, MIRG survey 2011: Snapshot of rapidly evolving label-free technologies used for characterizing molecular interactions, J. Biomol. Tech. 23 (2012) 94-100.

[93] A. Olaru, C. Bala, N. Jaffrezic-Renault, H. Aboul-Enein, Surface Plasmon Resonance (SPR) Biosensors in Pharmaceutical Analysis, Crit. Rev. Anal. Chem. 45 (2015) 97-105.

[94] P.P. Markowicz, W.C. Law, A. Baev, P.N. Prasad, S. Patskovsky, A.V. Kabashin, Phase-sensitive time-modulated surface plasmon resonance polarimetry for wide dynamic range biosensing, Optics Express. 15 (2007) 1745-1754.

[95] C. Caucheteur, T. Guo, J. Albert, Review of plasmonic fiber optic biochemical sensors: improving the limit of detection, Anal Bioanal Chem. 407 (2015) 3883-3897.

[96] K.H. Drexhage, Influence of a dielectric interface on fluorescence decay time, J Lumin. 1-2 (1970) 693-701.

[97] J.R. Lakowicz, Radiative decay engineering 5: Metal-enhanced fluorescence and plasmon emission, Anal. Biochem. 337 (2005) 171-194.

[98] O. Stranik, R. Nooney, C. McDonagh, B.D. MacCraith, Optimization of nanoparticle size for plasmonic enhancement of fluorescence, Plasmonics. 2 (2007) 15-22.

[99] O. Stranik, D. Iacopino, R. Nooney, C. McDonagh, B.D. MacCraith, Optical properties of micro-patterned silver nanoparticle substrates, J. Fluoresc. 20 (2010) 215-223.

[100] Y. Zhang, G.L. Keegan, O. Stranik, M.E. Brennan-Fournet, C. McDonagh, Highly sensitive C-reactive protein (CRP) assay using metal-enhanced fluorescence (MEF), J. Nanopart. Res. 17 (2015).

[101] J. Langer, S.M. Novikov, L.M. Liz-Marzán, Sensing using plasmonic nanostructures and nanoparticles, Nanotechnology. 26 (2015).

Chapter 3: Instrumentation

3.1 Introduction

A range of instruments were used in this largely multidisciplinary work in various aspects of the project. In this chapter, the instrumentation used throughout the work is described and the methods of operation explained in detail.

3.2 Microscopy

3.2.1 Transmission electron microscope

Transmission electron microscopy (TEM) is used to image samples at the low-micron and nano scale. There are a number of components in a TEM that distinguish it from optical microscopes, and these are described in conjunction with the theory of operation of a TEM. TEMs make use of electrons instead of photons for imaging samples. An electron gun, that can consist either of a heated filament or field electron gun, is used as the 'illumination' source. The electrons are accelerated towards an anode. While accelerating, the electrons pass through a number of magnetic fields which act like an objective lens in an optical microscope, whereby they focus the electron beam onto the sample specimen being investigated. The electrons pass through the sample and through another 'condenser lens' or magnetic field to focus the scattered electrons onto a screen, where they are collected and converted into images. Depending on the type of TEM, some will have more condensers than others.

TEM micrographs were obtained in this work using a Tecnai Transmission Electron Microscope (FEI, Oregon, USA). The FEI Tecnai F30 TWIN field emission gun was operated at 300 kV with a Twin lens, a field emission gun and a Gatan Ultrascan 895 CCD camera (Gatan, Oregon, USA). Specimens were prepared by dropping ethanol solutions of the nanoparticles onto a formvar carbon coated copper grid.

3.2.2 Fluorescence microscope

The light microscope has been used to view cells on the micron scale. This has been possible with the use of objective lenses, whose numerical aperture is the limiting factor for optical focusing, the smaller the aperture the shorter the wavelength needed to enter the objective. Organelles inside the cell and other submicron sized objects can be viewed using the optical microscope with the use of water or oil immersion lenses to change the refractive index and bend the light into the lens. A fluorescence microscope uses the same lenses as those used in the light microscope. However, they are usually inverted, lying below the sample so as to excite the sample and allow the collection of the emitted fluorescence through the same lens. These are called inverted microscopes. To allow a range of fluorescent dye imaging, the sample is illuminated with a lamp which first passes through a filter cube before illuminating the sample. Each filter cube has an excitation filter which functions much like a band pass filter allowing light of a certain bandwidth through and once the light has passed through this it then encounters a dichroic mirror. This dichroic mirror reflects light up to a certain wavelength and after the cut-off point transmits the light through the mirror instead. The initial excitation wavelength light is reflected up through an objective lens of the microscope which then focuses the excitation light on the sample. The sample fluoresces and the light passes back through the objective lens where it goes through the dichroic mirror and passes through the emission filter, which prevents unwanted light from reaching the CCD camera, see Fig 3.1 below for a schematic of this.
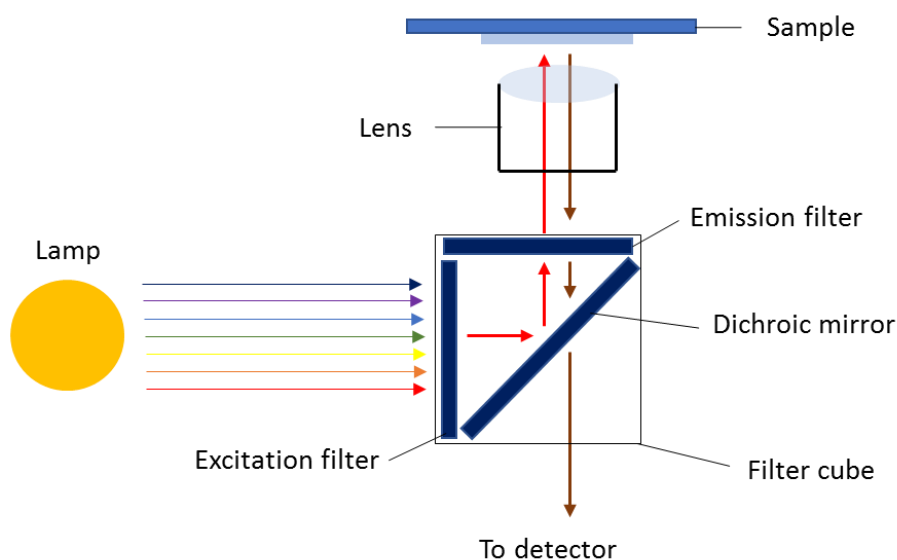
Fig 3.1: Schematic of optical set up of an inverted microscope with filter cube.

There are a broad range of fluorophores which can be used in the visible spectrum for cell imaging and, depending on the excitation and emission wavelengths of these fluorophores, filter cubes can be tailored to suit each one. The cubes can be added or removed from the microscope easily.

Fluorescence imaging was performed on an Olympus IX71 (Tokyo, Japan) inverted epifluorescence manual microscope with a JVC TK-1460 colour video camera (Yokohama, Japan) and using an Excelitas X-Cite series 120 excitation lamp (Technologies Corp, MA, USA). Images were taken at 20x magnification and using a 4',6-Diamidino-2-phenylindole (DAPI), FITC or Cy5 filter cube. The Olympus DAPI filter cube set had an excitation wavelength transmission of 352-402 nm and emission at 417-477 nm with the dichroic mirror at 409 nm. The FITC filter had an excitation wavelength transmission of 460-495 nm and emission of 515-550 nm with a dichroic mirror at 505 nm. The Cy5^{TM} filter cube set had an excitation range of 604-644 nm and emission of 672-712 nm with the dichroic mirror at 660 nm.

3.2.3 Confocal fluorescence microscopy

Confocal microscopy operates similarly to fluorescence microscopy except the excitation source is a laser instead of a lamp and, importantly, uses a pinhole in the collection optics to obtain high resolution images. Mirrors in the system are rotatable and are used to focus the lasers on a sample or to be scanned over an area. Any collected light passes up through the objective and through a dichroic mirror onto photomultiplier tubes (PMTs), where the signal is amplified. This method allows for scanning through cell specimens and a number of scans can be compiled in the Z axis to form a reconstructed 3D image of the sample. Confocal microscopes employ the use of a pinhole on the conjugate focal point so as to prevent unfocused photons from hitting the PMT which allows for better resolved images than from fluorescence microscopy alone [1]. As fewer photons reach the PMT than with a normal fluorescence microscope, an improved light source is required, such as a laser, for illuminating the specimen. See Fig 3.2 for a schematic representation of a confocal microscope.
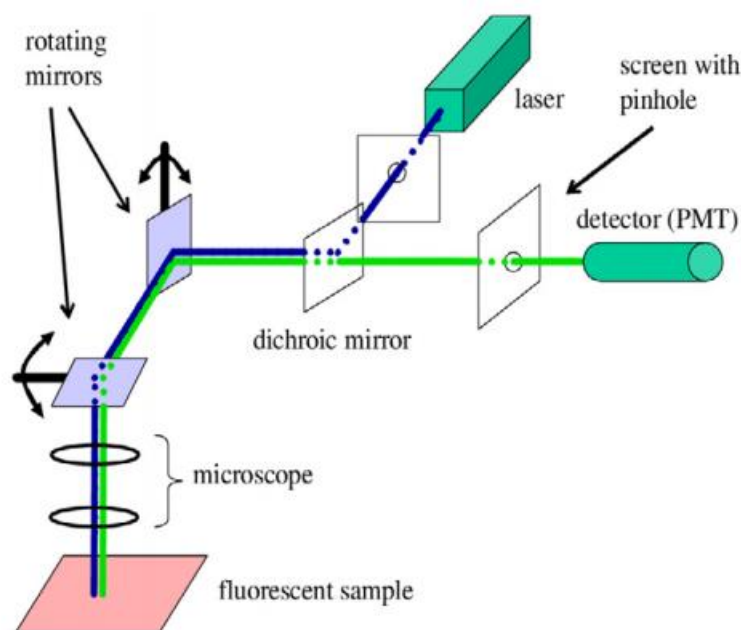
Fig 3.2: Configuration of a laser scanning confocal microscope [1] © IOP Publishing. Reproduced with permission. All rights reserved. doi:10.1088/0953-8984/19/11/113102

Confocal microscopy was carried out using a Leica Microsystems TCS SP8 microscope (Leica Microsystems, Wetzlar, Germany) using an 86x oil immersion lens and hybrid detectors. The excitation source was a Leica tuneable white light laser which is a pulsed IR-fibre laser that takes advantage of an acousto-optical filter that allows user orientated selection of excitation wavelengths [2].

3.3 Microplate reader (photospectrometer)

Microplate fluorescence measurements were performed using a Infinite® M200 PRO microplate reader (Tecan, Männedorf, Switzerland). For Cyanine5 dye doped nanoparticles, the excitation wavelength was set at 649 nm and the emission wavelength set at 679 nm. This particular micro plate reader operates without the use of filters but instead uses a monochromator.

A typical monochromator uses a Xenon flash lamp which is directed onto condenser optics after which it is focused back through a slit. See Fig 3.3 for a visual aid behind the operation of the microplate reader. The light then is incident on the monochromator grating which disperses the light into its component wavelengths. This light then passes through a 2nd slit to narrow the bandwidth of light selected after which the light is

dispersed once again on a 2nd monochromator and finally passes through an exit slit that is incident on the sample in the plate reader. The emission collection is done by passing the light through an entrance slit to prevent stray light and noise entering the detector. It then is incident on a 3rd monochromator, where the light is dispersed again and passes through another slit to select a bandwidth containing the desired emission wavelength.The light is dispersed once more on the 4th and final monochromator where the light goes through the last slit at the selected wavelength onto condensor optics which focus it onto a photomultiplier tube.
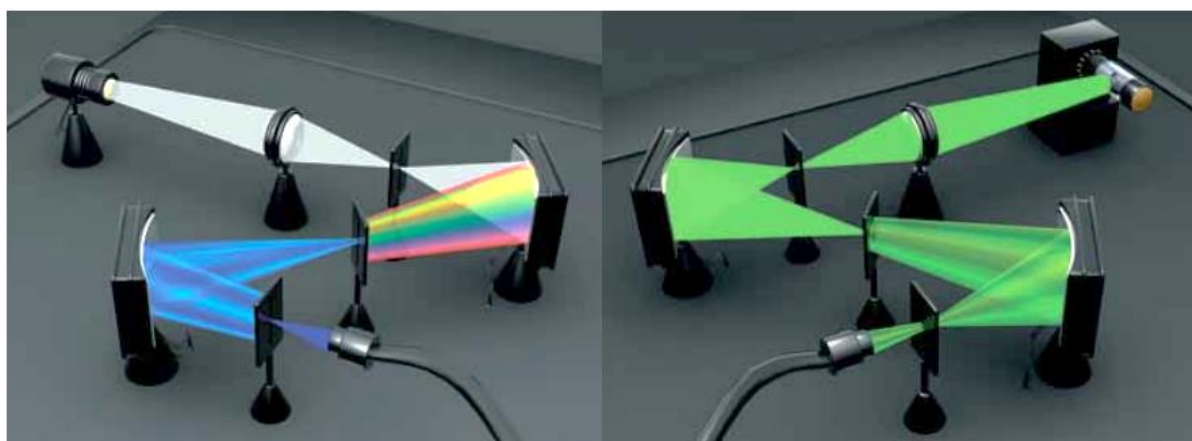
Fig 3.3: The optical setup of the Quad$_4$ Monochromators^{TM} in the Tecan Saphire Infinite PRO. Excitation optic setup (left) and collection optic setup (right) © Tecan 2012. Reproduced with permission. All rights reserved [3].

3.4 UV-vis photo spectrometer

UV-Vis photospectrometers are used to measure the absorption of photons through samples in liquid phase or for thin film solid samples. Light of a broad spectrum, 190 - 840 nm in some spectrophotometers [4], is passed through the sample in a cuvette of a certain length. The amount of light transmitted is calculated to give the number of photons that were absorbed by the sample across a range of wavelengths. Using the Beer-Lambert equation, *A=εcl* (Eq. 2.2), the sample concentration can be determined. It can be used to determine where the absorption maximum is and where fluorescent dyes should be excited. The spectrophotometer can determine protein, DNA or ribonucleic acid (RNA) concentration based on a ratiometric value of absorption at 280 nm [5,6]. It can also be used for colorimetric protein assays such as the Pierce bicinchoninic acid (BCA) test at 562 nm [7]. It is not recommended for use with samples that are highly

coloured and concentrated due to inner filtering effects or for highly scattering samples which could skew the results.

In this research, UV-Vis spectra were obtained of Cyanine5 and Cyanine3 free dye, synthesised Cyanine5 nanoparticles and dye labelled antibody conjugates. They were measured with a Nanodrop 2000c UV-Vis photo spectrometer (ThermoScientific, Delaware, USA) with a spectral range of 190-840 nm and used with a 1cm cuvette path length or the nanodrop function for dye labelled antibody with a 1 mm path length [4].

3.5 Dynamic light scattering instrument

A dynamic light scattering instrument (DLS) is capable of measuring the size of particles in a solution sample and/or their zeta potential. With the use of a monochromatic light source, such as a laser, the light is first polarised before entering the sample. The scattered light then exits the sample, is collected and passes through a second polariser after which the light is focused onto a photo multiplier tube (PMT) detector. The scattered light gives rise to interference patterns, bright spots for constructive interference and dark spots corresponding to destructive interference. An initial pattern is recorded of the sample at t=0 and taken at successive time points after this. As time progresses the interference pattern will change with the scattering of light due to the movement of particles. The movement is caused by Brownian motion. Smaller particles will create larger changes in the pattern as they move faster than larger particles and thus the instrument can correlate these changes to sizes of particles in solution using photon correlation spectroscopy.

Zeta potential can be measured by the electrophoretic light scattering. Laser light is directed through the particle suspension where the light will be scattered. A frequency shift occurs in the scattered light that is proportional to the velocity of the particles in solution (See section 2.4 for the theory of zeta potential). Because the frequency shift of the light is proportional to this velocity, the electrophoretic mobility of the particles can be measured [8].

All particle size and zeta potential measurements of samples in solution phase were performed on a Delsa™Nano C from Beckman Coulter. All samples were measured at a concentration of 0.3 mg/mL. The optical setup for zeta potential measurements is

shown in Fig 3.4, in which there are two lasers, one used as the incident beam that passes through the sample and one as a reference beam.
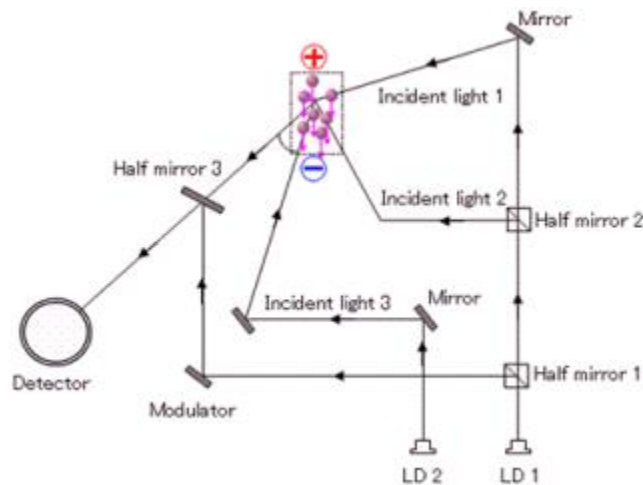
3.6 Flow Cytometer

Flow cytometers have been used for more than 50 years for cell analysis [9]. Their function is to measure cell size and granularity alongside protein expression using fluorophores. There has been a huge investment in the technology over this time and what initially started out as a one colour fluorescence cell cytometer, has now dramatically increased to counters that are capable of detecting 20 colours [10]. All cytometers contain at least two lasers; blue 488 nm laser and red 635 nm laser. However, more recent cytomers are capable of housing five lasers. These can include an ultraviolet laser at 355 nm, a violet laser at 405 nm and a green laser at 561 nm. This allows more fluorophores to be used when carrying out flow cytometry as the lasers are spatially separated by their positioning in the instrument. This means the photons will reach the detectors at different times and will prevent crossover between two fluorophores which have the same emission wavelength but different excitation wavelengths. As well as cell analysers, there are cell sorters, instruments capable of separating cell populations based on distinguishing between different fluorophores on the cells. But for the basis of the experiments carried out for this project, only a cell analyser was needed. Different systems from SonyBiotechnology, Beckman Coulter, BD Biosciences and Merck

Millipore offer different configurations with regards to laser, microfluidics and optical collection set up.

A Merck Millipore Guava EasyCyte[TM] 8HT analyser was used for the duration of this work. This cytometer has a 75mW 488 nm blue laser and 40mW 635 nm red laser [11]. It is capable of measuring 6 fluorescence channels as well as forward and side scatter. Forward scatter is used to measure the size of the beads/cells and the side scatter measures the granularity of the beads/cells. The Guava cytometer uses a microcapillary to take samples from a 96 well microtitre plate and at a point along the capillary the red and blue laser pass through the sample. Based on the diagram in Fig 3.5, it can be seen how the Guava can distinguish between different fluorescence emission through the use of band pass filters, which only allow light of certain wavelengths through and reflects the rest of the light onto a photomultiplier and photo diode. InCyte[TM] software allows manipulation and analysis of data to focus and separate certain populations of cells from background noise based on forward scatter and fluorescence of cells. The first four bandpass filters are for use with the blue laser and the last two for the red laser.
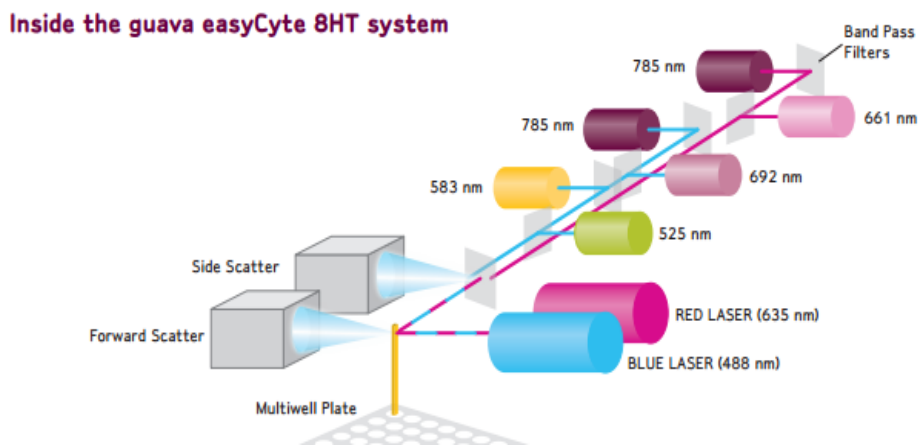
Fig 3.5: Guava EasyCyte[TM] benchtop flow cytometer laser excitation and photon collection system. © Merk Millipore. Adapted from [11].

3.7 Haematological analyser

Haematological analysers are very useful tools in blood laboratories owing to their rapid testing, high throughput and accurate cell counting. The haematological counter used in this thesis was the Coulter AcT diff2 analyser (Beckman Coulter, CA, USA). This particular blood analyser counts the blood cells based on the Coulter Principle for cell

counting and sizing. This method measures the change in resistance across a circuit when blood cells suspended in fluid pass through two electrodes and from this change in resistance both the size and number of cells can be obtained [12]. This is possible as the cells are suspended in a conductive fluid and cells are insulating, the resulting impedance is related to the volume of the particle that has passed through an aperture which are connected to electrodes. As several types of cells have varying sizes, the distribution pattern of impedance can be correlated to blood cell sub-types.

3.8 References

[1] V. Prasad, D. Semwogerere, E.R. Weeks, Confocal microscopy of colloids, Journal of Physics: Condensed Matter. 19 (2007) 113102.

[2] R.T. Borlinghaus, L. Kuschel, Leica Microsystems, White light laser the ultimate source for confocal microscopy, 2017 (2012).

[3] Tecan, Tecan Infinite® 200 PRO, 2016 (2012).

[4] Thermo Scientific, Nanodrop 2000c UV-Vis spectrophotometer, 2015 (2013).

[5] E. Layne, [73] Spectrophotometric and turbidimetric methods for measuring proteins, Methods Enzymol. 3 (1957) 447-454.

[6] C.M. Stoscheck, Quantitation of protein, Methods Enzymol. 182 (1990) 50-68.

[7] P.K. Smith, R.I. Krohn, G.T. Hermanson, A.K. Mallia, F.H. Gartner, M.D. Provenzano, E.K. Fujimoto, N.M. Goeke, B.J. Olson, D.C. Klenk, Measurement of protein using bicinchoninic acid, Anal. Biochem. 150 (1985) 76-85.

[8] Beckman Coulter, User's Manual Delsa™Nano Submicron Particle Size and Zeta Potentia, 2015 (2011).

[9] M.J. Fulwyler, Electronic separation of biological cells by volume, Science. 150 (1965) 910-911.

[10] BD Biosciences, BD LSRFORTESSA X-20, 2015 (2016).

[11] Millipore, guava® Flow Cytometry easyCyte™ Systems, 2016 (2010).

[12] W.H. Coulter, High speed automatic blood cell counter and cell size analyzer., Procedings of the National Electron Conference. 12 (1956) 1034-1040.

Chapter 4: Nanoparticle synthesis and characterisation

This chapter describes the synthesis and characterisation of Cyanine5 dye-doped silica particles. Measurements were made to evaluate their size, stability, fluorescence and biological affinity, all of which are fundamental to understanding their properties.

4.1 Introduction

Dye-doped silica nanoparticles have previously been used for biomedical applications such as cell imaging and immunoassays [1]. They have advantages such as ability to carry hundreds of dye molecules, chemical stability, hydrophilicity, biocompatibility and relative non-toxicity [2]. Their facile surface chemistry means that targets such as aptamers, antibodies and DNA can be conjugated to the NPs to allow them to function as biosensors [3,4]. The NPs have been shown to easily incorporate a range of dyes across the spectrum including Rubpy, FITC, Cyanine5 and Cy7, to name but a few [3-7]. Models of fluorescence ratio of dye-doped NPs in comparison to the free dye molecule at the same concentration have shown that an increase in signal can be achieved of up to at least two orders of magnitude, despite the effects of homo-Förster Resonance energy transfer (h-FRET) which limits the dye loading of NPs [5]. Dyes in the red and near infrared spectrum (650–950 nm) have become increasingly popular for use in biological detection systems. At these wavelengths, there is less inherent autofluorescence because light absorption of blood and tissue are minimal and for this reason these dyes are good candidates for use in cell staining and imaging [8].

Key parameters to prevent non-specific binding include a negative zeta potential, PEG functionalisation and protein stabilisation of NPs, as discussed in section 2.7.2. It has been reported that, to prevent NPs from crossing the cell membrane, they need to be negatively charged because phospholipid membranes are also negatively charged, leading to electrostatic repulsion, whereas positively charged NPs are more regularly up taken [9,10]. PEG has been used to increase circulation times of NPs in vivo due to reduction in aggregation of opsonins and proteins from blood serum on the surface of

NPs that cause endocytosis [11,12]. It has been shown that proteins can help to stabilise NPs by creating a protein layer around the particles, also known as a protein corona, which aids in preventing aggregation sterically in protein rich sample media such as serum [13-15]. Taking all these factors into consideration, I have developed a negatively charged PEGylated NP, that is colloidally stable, for specific targetting of EpCAM antigens on cancer cells.

4.2 Materials and methods

4.2.1 Materials

Cyanine5-NHS ester dye (Cyanine5) was obtained from Lumiprobe GmbH (Hannover, Germany). Formvar grids for TEM were purchased from Agar Scientific (United Kingdom). 8-arm PEG (10,000 mW) was purchased from Nanocs (Boston, MA, USA). Anti-EpCAM purified monoclonal antibody was obtained from BioLegend (SanDiego, CA, USA). All other materials were obtained from Sigma-Aldrich, unless otherwise stated.

4.2.2 NP synthesis:

The theory behind NP synthesis has been described in section 2.7. Cyanine5 was incorporated into silica nanoparticles at two different weight percents using the reverse microemulsion method as described previously [6]. In brief, dye was added at a concentration of 0.108mg and 0.218mg to give theoretical yields of dye at 0.5% and 1%, respectively. The dye was conjugated with aminopropyltrimethoxysilane (APTMS) in a molar ratio of 5:1 to achieve covalent attachment to the silica. This conjugate was added to 10mL of cyclohexane, 260mg of dioctyl sulfosuccinate sodium salt (AOT), 230mL of polyoxyethylene nonylphenylether (NP5), 80μL of tetraethyl orthosilicate (TEOS), 70μL water and 60μL of ammonium hydroxide for 24 h. The resulting emulsion was broken using ethanol and the NPs washed three times with ethanol using centrifugation. After this, the yield of NPs was calculated from drying and weighing 1 mL solutions. From TEM, the size of NPs was determined and subsequently the weight of one NP found using a density of 1.6g/cm^3 for silica [16]. Knowing the dried weight of NPs and the corresponding weight of one NP, the number of particles in solution was also determined.

The initial synthesis step was followed by the addition of a double silica shell coating

using the Stöber method, in order to obtain a uniform silica surface to functionalise [17]. Firstly, 20μL of TEOS was added to 5.2mg of NPs in ethanol and water solution followed by 100μL of ammonium hydroxide and left for 24 h. Another 20μL was added after this time to coat a second shell. Following this, an amine layer was coated onto the surface of 6mg of particles in ethanol using 20μL of bis(3-triethoxysily) propylamine (dipodal APTES).

4.2.3 Functionalisation and antibody conjugation:

Methods used for conjugating DNA to the surface of NPs described by Kelleher et al. were modified to conjugate EpCAM to the surface of NPs [18]. In short, 2mg of 8-arm $PEG_{10,000}$ was incubated with 2mg of NPs for 24 h in 0.1 M 2-(N-morpholino)ethanesulfonic acid (MES) pH 4.7 and 50mM 1-Ethyl-3-(3-dimethylaminopropyl) carbodiimide (EDC) and purified in ethanol. Post PEGylation the carboxyl groups on the NPs were reactivated with 50mM EDC and 12.5mM N-hydroxysulfosuccinimide sodium (NHS) salt in MES pH 4.7 buffer for 15 min and were then left to react with antibody in 0.1 M MES pH 7.2 buffer for 24 h. After this, the NPs were resuspended into phosphate buffer saline (PBS) containing 1% Bovine Serum Albumin (BSA) for 24 h before being washed in PBS three times and finally placed into PBS containing 1% BSA, 0.05% Tween®20 and 0.01% sodium azide for short term storage at 4 °C. This solution was chosen, as previous studies of colloidal stability of silica nanoparticles indicated that this was an optimal solution [19]. The sodium azide was added to prevent the growth of microbes.

4.2.4 Fluorescence characterisation methods:

4.2.4.1 TEM size analysis

Transmission electron microscope (TEM) size measurements were carried out using a FEI Tecnai F30 (FEI, Oregon, USA) twin field emission gun operated at 300 kV with a Twin lens and an Ultrascan 895 CCD camera (Gatan, Oregon, USA). See section 3.2.1 in relation to the operation of a TEM. NP diameters were determined by analysis of images on Image J software from the National Institutes of Health (Bethesda, MD, USA) on 100 NPs on Formvar grids.

4.2.4.2 Modelling dye-loading and number of dye molecules per NP

Models were produced using MATLAB (MathWorks Inc, Natick, MA, USA). Two programmes were modified from previous NIR dye molecules models [20]. The first

programme was run to produce the Förster radius for FRET between two Cyanine5 dye molecules, required for Eq. 2.4 in section 2.2.5. The Förster radius can be calculated by equation 4.1 and the programme that was run can be found in Appendix A1.

$$R_0^6 = \frac{9ln10}{128\pi^5 N_a} \frac{\kappa^2 Q_D}{n^4} J \qquad \text{(Eq. 4.1)}$$

where N_a is Avogadro's number, κ is the dipole orientation of the dye molecules, Q_D is the fluorescence quantum yield, n is refractive index and J is the spectral overlap between the absorption and emission of dye molecules. A value of 0.2 is used for Q_D, 2/3 for κ and 1.5 for n. The code for the second programme, to find the effects of FRET within a nanoparticle, was theoretically calculated using Eq. 2.3 for NPs with different radii and the code for that programme can be found in Appendix A2. Weight percent loading of dye in the NP was calculated by dividing the mass of one NP by the mass of the dye inside it. The molecular weight of the dye used in this calculation is 616.19 g/mol. The brightness ratio was a comparison of the photon emission of one NP compared to one cyanine5 free dye molecule.

4.2.4.3 Experimental determination of dye loading and number of dye molecules

The dye loading and number of dye molecules per NP were determined experimentally by measuring the absorption on the UV-vis of dissolved NPs. NPs at 0.5 mg/mL were placed in a silica dissolving buffer at pH 10 containing 0.5% sodium dodecyl sulphate and the absorbance of the NPs was measured every minute until t=60 min using a Nanodrop 2000c (ThermoScientific, DE, USA). See section 3.4 in relation to the optical range of this particular instrument. It was apparent that the dissolution had finished at t=60 mins as the absorbance at short wavelengths ~400 nm, due to the silica scattering, had stopped decreasing. The absorbance graphs were background subtracted and the absorbance at 650 nm was used to calculate both the weight percent and number of dye molecules.

4.2.4.4 Fluorescence comparison to single dye molecule

Fluorescence properties of the NPs were measured on an Infinite 200 microplate reader (Tecan, Männedorf, Switzerland). See section 3.3 regarding the optical setup of the microplate reader. By making a cascade dilution of the two sets of NPs in ethanol, and

also of Cyanine5 free dye, the fluorescence enhancement could be determined when comparing the concentration of NPs to the concentration of free dye.

4.2.4.5 DLS size and zeta measurements

Size and zeta measurements of the NPs were taken on a dynamic light scattering instrument (DLS) Delsa Nano C from (Beckman Coulter, CA, USA). See section 2.4 and 3.5 in relation to zeta potential theory and DLS optical setup. All measurements were carried out at the same concentration (0.3 mg/mL) using a glass cuvette for size and a disposable flow cell for zeta measurements.

4.2.5 Protein-dye labelling and quantitative measurement of the number of antibodies on a nanoparticle

Human IgG was labelled with sulfonated Cyanine3 dye (Lumiprobe GmbH, Hannover, Germany). 1 mg of dye was added to 0.5 mg of human IgG which was buffer exchanged into MES pH 7.2 and left to react for 2 hours. The molar ratio of dye to antibody was 20:1. The dye conjugate was then filtered into MES pH 7.2 for reaction with PEG coated nanoparticles. The actual dye to antibody ratio was calculated using a corrected absorbance concentration of the dye molecule compared to the antibody and is given by

$$[Dye] = \frac{A_{Max}}{Molar\ coefficient} \quad \text{and} \quad [Antibody] = \frac{A_{280} - (0.08 x A_{Max})}{Ab\ molar\ coefficient} \qquad \text{(Eq. 4.2)}$$

where A_{Max} is the absorbance maximum of the Cyanine3 dye found at 551nm, the *molar coefficient* is the molar extinction coefficient found to be 162,000 $M^{-1}cm^{-1}$ for Cyanine3, A_{280} is the absorbance of the IgG protein and 0.08 is the correction factor for the absorbance of Cyanine3 at 280nm and *Ab molar coefficient* is the molar attenuation coefficient for IgG which is 210,000 $M^{-1}cm^{-1}$. The final dye to antibody ratio is given by [Dye]/[Antibody]. Using $A_{551}=0.130$, $A_{280}=0.271$, measured from absorbance, and molar coefficients mentioned above, a dye labelling of 0.675 dyes was obtained per antibody.

A calibration curve was obtained for both the Cyanine3 labelled antibody and Cyanine5 PEG coated NPs. This was done using a cascade dilution of known concentrations of antibody and NPs and measured on the microplate reader exciting at 546nm for Cyanine3 IgG and 649nm for cyanine5 NPs. PEG coated NPs were incubated with different concentrations of labelled IgG overnight before the supernatant was measured the next day in the microtitre plate reader. The NPs were measured fluorescently,

directly from the sample, and compared to a fluorescence vs concentration calibration curve previously generated for the NPs to obtain the concentration of NPs in the sample. Based on the fluorescence of both the NPs and the IgG the concentration of both could be back calculated and was determined.

4.3 Results and discussion

Two sets of NPs with ab initio Cyanine5 dye loadings of 0.5% and 1% were characterised using TEM, fluorescence and absorbance measurements, the results of which are presented in the following pages.

4.3.1 Nanoparticle size analysis: TEM

From TEM images, the nanoparticles, as synthesised, had an average radius of 23.2 ± 2.0 nm and 20.4 ± 1.0 nm for 0.5% and 1% respectively (n= > 100 in all measurements and see Fig B1 in appendix B for 1% TEM images). The smaller particle size for higher dye loadings is due to classic nucleation theory where changes in supersaturation point directly affect the number of nucleation points. When the concentration of the hydrophobic dye increases, it leads to lowering of the supersaturation point resulting in more nucleation points and smaller NPs [21]. After synthesis of the bare NP, the 0.5% NPs were analysed at every step in the functionalisation process using TEM. As expected, the NPs increased significantly in radius after the addition of a TEOS shell and surface amination to 31.8 ± 1.5 nm. Upon PEGylation and antibody conjugation no further size increase was observed within standard deviation (see Fig. 4.1). Also the NPs were of similar size between the two sets after PEGylation with 0.5% NPs measured to be 33.3 ± 1.6 nm and 1%, 29.0 ± 1.3 nm.

It is interesting to note the difference in appearance of the antibody conjugated NP set (Fig. 4.1(d)). The NPs in this image show a surface roughness when compared to Figs 4.1(a)-(c) which is indicative of the presence of the antibody layer. Previously published TEM pictures of mesoporous silica NPs coated with monoclonal antibodies do not appear to show this roughness [22]. However, these particles were synthesised using a templating method which produces a hexagonal structure on the surface, so it is difficult to compare to the NPs reported here. In another previous study, TEM images of iron oxide NPs conjugated with antibodies show much clearer definition between antibody

and NP due to the better contrast between the electron-poor antibody and the electron-rich oxide particle [23]. The monodispersity of the NPs could not be implied from TEM due to aggregation of NPs during preparation of TEM grids but was investigated later using DLS.
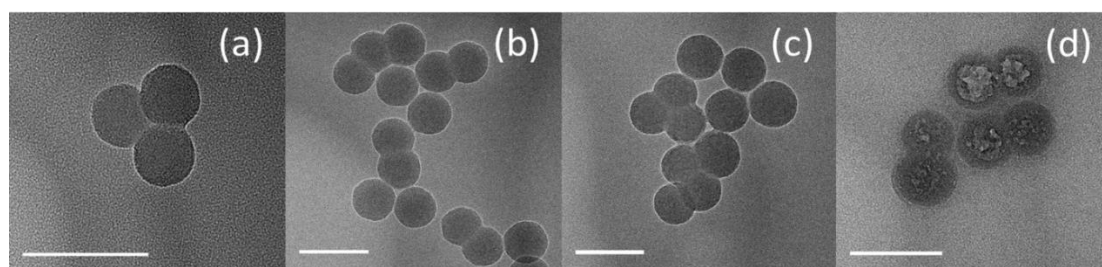
Fig 4.1: TEM images of 0.5% NPs at different steps throughout the synthesis method: (a) as synthesised, 23.2 ± 2.0 nm radius; (b) amine functionalised, 31.9 ± 1.5 nm radius; (c) PEGylated, 33.3 ± 1.6 nm radius; and (d) antibody conjugated, 30.0 ± 3.5 nm radius. The scale bar is 100 nm in each image. Previously published by author [24].

Table 4.1: Characterisation of 0.5% (w/w) and 1% (w/w) Cyanine5-doped NPs using TEM.

NP set	Radius as synthesised [nm] (from TEM)	Radius + amine layer [nm]	Radius + PEG layer [nm]	Radius + anti-EpCAM layer [nm]
0.5%	23.20 ± 1.96	31.8 ± 1.5	33.3 ± 1.6	30.0 ± 3.5
1%	20.38 ± 1.00	N/A	29.0 ± 1.3	N/A

4.3.2 Colloidal stability: Nanoparticle hydrodynamic radius and zeta potential

To investigate the colloidal stability and if the dye-doped silica NPs were monodispersed, the NPs hydrodynamic radius and zeta potential were measured at each functionalisation step. In most cases, NPs were analysed at a concentration of 0.3 mg/mL in deionised water. However, antibody coated NPs were also measured in conditions that were reported previously for the stabilisation of NPs in immunoassays; PBS containing 1% BSA and 0.05% Tween®20 [19]. Fig 4.2 contains data for both measurements of the particles at each step and the next paragraph is based on these results.

Newly synthesised dye-doped silica NPs have a negative zeta potential and after the addition of two silica shells the potential did not differ significantly. This indicates that the dye encapsulated does not interfere with surface charge. They appear to be relatively monodisperse and stable in water, as indicated by the low hydrodynamic radius, which

is 52.3 ± 13.9 nm for 0.5% NPs and 75.2 ± 18.6 nm for 1%. When the NPs are coated in amine groups, there is an increase in hydrodynamic radius which would indicate some aggregation of NPs. The zeta potential has also become positive but from the DLS measurement the particles are aggregating somewhat in solution. It is most likely, that the static repulsion between NPs is not sufficiently positive enough to generate stabilisation, via surface charge. After the addition of PEG molecules to the NPs, there is a reduction in hydrodynamic radius of statistical significance (P<0.05) for both sets of NPs. As the zeta potential remains statistically unchanged it appears that PEG acts as a stabilising agent due to the reduced hydrodynamic radius. Upon the covalent attachment of antibody and BSA to the surface of the NP, the hydrodynamic radius is statistically insignificantly changed (P>0.05) showing stability in both water and PBS containing 1% BSA and 0.05% Tween®20 and the zeta potential of the particles has become negative. Interestingly, there is a statistically significant difference (P<0.05) in zeta potential between the two sets of NPs which were similar at each functionalisation step until the antibody was introduced. As the two sets were functionalised in the exact same way and the only difference between them is the radius and number of dye molecules per NP it is possible that more antibody could attach to the surface of the 0.5% as they have a larger surface area. Importantly, although they differ significantly in zeta potential, the two sets of NPs do not aggregate in the PBS solution which indicates that it is a suitable working solution for cell staining and imaging protocols.
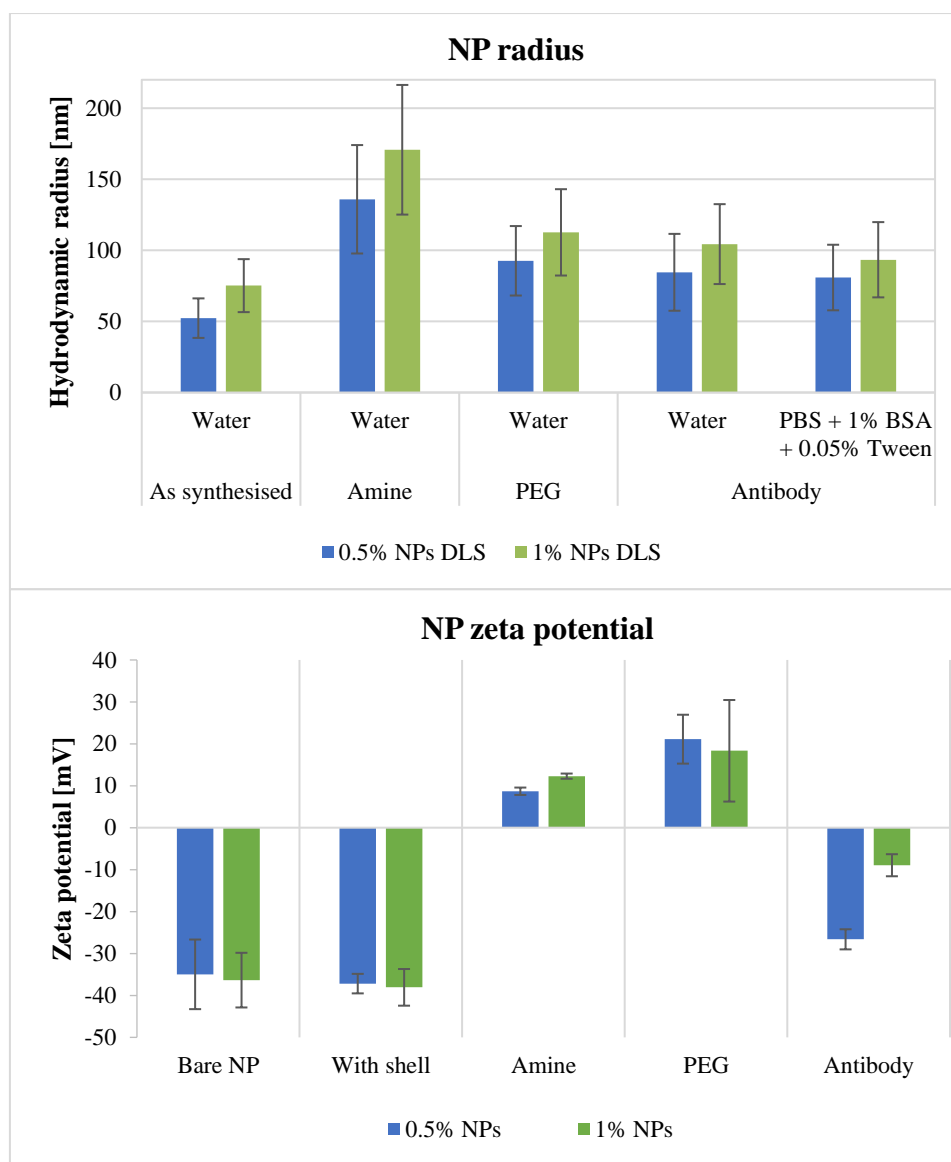
Fig 4.2: Hydrodynamic radius (top) and zeta potential (bottom) of 0.5% (blue) and 1% (green) NPs at different stages in the functionalisation process measured in water on the DLS except the Antibody sample in the zeta and NP size graph, measured in PBS containing 1% BSA + 0.05% Tween®20.

4.3.3 Number of dye molecules per nanoparticle

To achieve a more accurate estimate of the actual weight percent dye loading in the NPs and to calculate the number of dye molecules per NP, the NPs were dissolved using a carbonate buffer, to release the dye molecules from the silica matrix. Both sets of NPs were placed in a carbonate buffer at pH 10 and, when the silica was dissolved, the absorbance of the dye was measured at t=60 min. The results were used to calculate the actual weight percentage loading of NPs (see Fig B2 in appendix B). It was found that the nominal 0.5% particles actually contained 0.168% dye while the nominal 1%

contained 0.279% dye. This indicates that only roughly 30% of dye added was encapsulated and is due to the reverse microemulsion synthesis method. Previous work to incorporate another red dye, FR664, with a quaternary microemulsion method resulted in a less than 20% yield which is lower than the quaternary method used here [20]. The dissolution absorbance also allows for a more accurate calculation of the number of dye molecules inside each NP. Based on the absorbance, the number of dyes inside the two sets of NPs was calculated to be 137 for 0.168% and 155 for 0.279% as seen in Table 4.2.

Table 4.2: Characterisation of 0.5% (w/w) and 1% (w/w) Cyanine5-doped NPs using TEM, UV-Vis and fluorescence

NP set	Absorbance	Actual Weight % loading	Dye molecules per NP (from absorbance)	Brightness ratio of NPs to Cyanine5 at same conc. from model	Brightness ratio of NPs to Cyanine5 at same conc. measured
0.5%	0.340	0.168	137 ± 7	116	129
1%	0.566	0.279	155 ± 8	109	113

The brightness ratio of the two sets of NPs was investigated. This is the measure of the fluorescence of the NP labels divided by the fluorescence of Cyanine5 dye molecules at the same concentration and is a measure of the relative brightness of the NP compared to the dye molecule (see Fig B3 in appendix B). The measurements, which were made after NP synthesis before addition of shell, yielded a ratio of 129 for the 0.168% to Cyanine5 free dye and 113 for the larger dye concentration of 0.279% (see Table 1). This data was compared to a previously published h-FRET model of NP dye loading that has been modified for Cyanine5 dye (Förster radius of 5.55 nm and a quantum efficiency of 0.2) [20]. The model is based on standard Förster energy transfer equations in which both donor and acceptor are Cyanine5 molecules and the h-FRET takes place as a result of the small Stokes shift of the dye. A reduction in fluorescence happens as the dye concentration is increased leading ultimately to saturation of the fluorescence of the dye molecules in the silica matrix and causes a decrease in emitted intensity. This is illustrated in Fig. 4.3, which represents the theoretical behaviour of the emission of NPs of a particular size as a function of dye loading. The y-axis of the graph represents the brightness ratio defined above. The predicted ratios for the two dye concentrations are 116 for 0.168% and 109 for 0.279% compared to measured values of 129 and 113 as

seen in Table 4.2. The theoretical maximum ratio is 166 and 118 for the 23 nm radius NP and 20.5 nm radius NP respectively, both approximately occurring at 0.41% dye loading. From the experimental results, the 20.5 nm NPs (0.279%) are close to the maximum ratio. Clearly, the experimental data does not fit exactly to the model, as there are a number of assumptions. For example, in the model only nearest neighbour transfer is considered, the molecules are assumed to be homogenously distributed in the particles, any dye aggregation effects are ignored, and any changes in dye quantum efficiency are not taken into account. As noted above, the size of the higher concentration NP with larger number of dye molecules, is smaller than that of the lower concentration particle. This accounts for the lower predicted ratios which is consistent with the measured value and consistent with a larger h-FRET effect in these particles due to the closer proximity of the dye molecules.
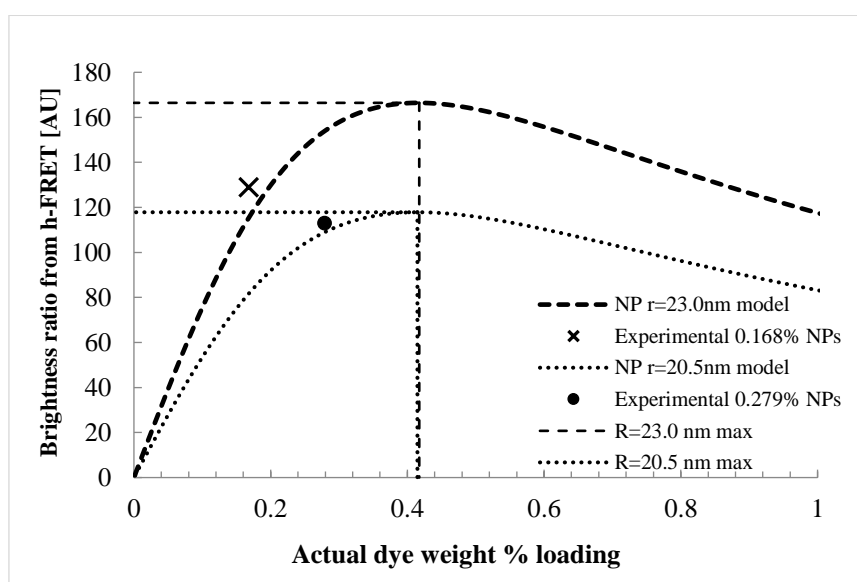
Fig 4.3: H-FRET model of fluorescence ratio compared with Cyanine5 free dye for 23.0 nm and 20.5 nm NPs. Previously published by author [24].

4.3.4 Antibody functionality and number per nanoparticle

It is important to be certain, when using the NPs as biosensors that firstly, the antibody is conjugated to the surface of the NP and secondly, the antibody retains its affinity for the antigen of interest after conjugation to the surface. 0.5% NPs were tested to ensure that the NPs were coated with antibody and also to determine quantitatively how many antibodies are on each nanoparticle. Cyanine3 labelled human IgG was covalently attached to the NPs as per the protocol described in section 4.2.5. NPs were incubated with different amounts of antibody in solution for conjugation. The number of antibodies

on each particle was determined through the supernatant once the particles had been centrifuged and were in a pellet. In this method, the number of labelled antibodies on the nanoparticle is equal to the initial amount of antibody added minus the amount found in the supernatant, see section 4.2.5 for methodology.
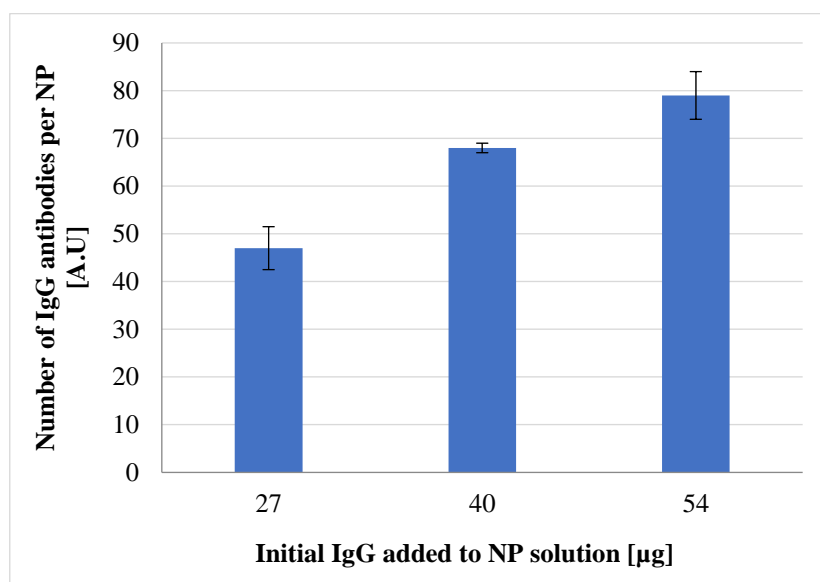
Fig 4.4: The number of human IgG antibodies per NP based on the μg amount added initially at conjugation. Concentrations of cyanine3 labelled IgG were calculated from fluorescence based measurements on the supernatant. 0.5mg of NPs added initially, accurate NP concentration was measured using fluorescence directly from sample.

The results in Fig 4.4 reflect the average of three different sets of NPs that were conjugated with Cyanine3 labelled human-IgG. Each experiment was carried out with 0.5mg of NPs. The highest number of antibodies per NP was achieved with the highest amount of starting antibody as was expected. The trend appears to be decreasing proportionally to the amount of antibody added, the 27μg of IgG having almost half the number of antibodies per NP as the 54μg set. It is assumed that, at some point, the surface of the NP must reach saturation however, the saturation point does not lie within this range of concentration. Accurate calculations of the IgG that was directly on the NP surface could not be carried out due to self-quenching effects of the Cyanine3 fluorophores, conjugated to the antibody, in close proximity to each other. This direct sampling method was tested on the 54μg set for comparison purposes and there was found to be 16 antibodies per NP using this method, compared with 79 antibodies from the supernatant method. The direct fluorescence measurement yields a lower concentration of antibody from FRET effects and highlights the importance of using the supernatant for analysis.

Knowing how many antibodies are on the surface of each nanoparticle is useful information, but more relevant information is knowing how many are available to bind to an antigen. This is dependent on antibody orientation on the surface of the nanoparticle and also assumes that the antibodies do not denature when conjugated to the NP. The antibodies are covalently attached to the NP through NH_2 groups, which are found on lysine residues throughout the structure of the antibody and so the location of the amine group bound to the NP cannot be known. To investigate this, two sets of 0.5% NPs were conjugated with 27μg of antibody and conjugated with either unlabelled human-IgG or unlabelled anti-human IgG as the EpCAM antigen is commercially unavailable to purchase. These NPs were incubated with Cyanine3 labelled human IgG and the number of specifically bound antibodies determined. The human IgG NPs were used to investigate the amount of non-specific binding that occurs on the NPs. The experiment was repeated in a high protein media, which was PBS containing 10% FBS, to determine the functionality of the particle in a high salt and protein environment. The results of this can be seen in Table 4.3.

Table 4.3: The number of cyanine3 labelled human IgG antibodies bound to anti-human IgG NPs or human IgG NPs

	Anti-human IgG NPs	Human IgG NPs
No. of h-IgG bound (active antibodies)	52 ± 2	2 ± 1
No. of h-IgG bound- high protein (active antibodies)	50 ± 3	2 ± 1

From the work previously presented in this section, Fig. 4.4, 27μg of antibody shows 47 ± 5 antibodies binding to the surface of a NP. The results from the functionality experiment show that there were 52 Cyanine3 human IgG antibodies bound to the particle, indicating that all antibodies on the particle surface were available to bind to the appropriate antibody. This does not necessarily translate for cellular sensing because the antigen, on the surface of the cell in this case, will be unable to freely move in solution, which should be taken into consideration. With regard to the human IgG NPs, it can be seen that two antibodies bound non-specifically to the particle. As the number is very low, it implies that the surface of the NP is suitable for the current application.

Similar results were obtained for the NPs that were incubated in high protein media and this is an indication of how the NPs will react in biological milieu. The conjugated antibody on the NP appears to have retained its functionality and to be unhindered by the protein in the solution, showing a promising outlook for use in biological environments.

4.4 Conclusion

Cyanine5 dye-doped silica NPs at two different weight percent loadings, 0.168% and 0.279% were successfully synthesised and functionalised with antibody. Their size, zeta and fluorescence properties have been characterised and they appear stable in water and in PBS containing 1% BSA and 0.05%Tween®20, a buffer that can be used for cell staining and imaging. The antibodies conjugated to the NP have been verified as functional and the number of antibodies on the surface calculated. This knowledge will be useful throughout the remaining results chapters of the thesis and an essential understanding of the particles has been achieved to move on to the next steps of evaluating specificity in the cellular environment.

4.5 References

[1] W. Wei, M. Wei, S. Liu, Silica nanoparticles as a carrier for signal amplification, Rev. Anal. Chem. 31 (2012) 163-176.

[2] C. Caltagirone, A. Bettoschi, A. Garau, R. Montis, Silica-based nanoparticles: A versatile tool for the development of efficient imaging agents, Chem. Soc. Rev. 44 (2015) 4645-4671.

[3] M.-. Estévez, M.B. O'Donoghue, X. Chen, W. Tan, Highly fluorescent dye-doped silica nanoparticles increase flow cytometry sensitivity for cancer cell monitoring, Nano. Res. 2 (2009) 448-461.

[4] L. Tao, K. Zhang, Y. Sun, B. Jin, Z. Zhang, K. Yang, Anti-epithelial cell adhesion molecule monoclonal antibody conjugated fluorescent nanoparticle biosensor for sensitive detection of colon cancer cells, Biosens. Bioelectron. 35 (2012) 186-192.

[5] R.I. Nooney, C.M.N. McCahey, O. Stranik, X. Le Guevel, C. McDonagh, B.D. MacCraith, Experimental and theoretical studies of the optimisation of fluorescence from near-infrared dye-doped silica nanoparticles, Anal. Bioanal. Chem. 393 (2009) 1143-1149.

[6] R. Nooney, C. O'Connell, S. Roy, K. Boland, G. Keegan, S. Kelleher, S. Daniels, C. McDonagh, Synthesis and characterisation of far-red fluorescent cyanine dye doped silica nanoparticles using a modified microemulsion method for application in bioassays, Sens Actuators, B Chem. 221 (2015) 420-479.

[7] S. Biffi, L. Petrizza, E. Rampazzo, R. Voltan, M. Sgarzi, C. Garrovo, L. Prodi, L. Andolfi, C. Agnoletto, G. Zauli, P. Secchiero, Multiple dye-doped NIR-emitting silica nanoparticles for both flow cytometry and in vivo imaging, RSC Adv. 4 (2014) 18278-18285.

[8] Z.-. Li, W. Cai, X. Chen, Semiconductor quantum dots for in Vivo, J. Nanosci. Nanotechnol. 7 (2007) 2567-2581.

[9] O.S. Wolfbeis, An overview of nanoparticles commonly used in fluorescent bioimaging, Chem. Soc. Rev. 44 (2015) 4743-4768.

[10] S. Jambhrunkar, Z. Qu, A. Popat, J. Yang, O. Noonan, L. Acauan, Y. Ahmad Nor, C. Yu, S. Karmakar, Effect of surface functionality of silica nanoparticles on cellular uptake and cytotoxicity, Mol. Pharm. 11 (2014) 3642-3655.

[11] V.C.F. Mosqueira, P. Legrand, R. Gref, B. Heurtault, M. Appel, G. Barratt, Interactions between a macrophage cell line (J774A1) and surface-modified Poly(D,L-lactide) nanocapsules bearing poly(ethylene glycol), J. Drug Targeting. 7 (1999) 65-78.

[12] M.I. Papisov, Theoretical considerations of RES-avoiding liposomes: Molecular mechanics and chemistry of liposome interactions, Adv. Drug Deliv. Rev. 32 (1998) 119-138.

[13] M.P. Monopoli, D. Walczyk, A. Campbell, G. Elia, I. Lynch, F. Baldelli Bombelli, K.A. Dawson, Physical-Chemical aspects of protein corona: Relevance to in vitro and in vivo biological impacts of nanoparticles, J. Am. Chem. Soc. 133 (2011) 2525-2534.

[14] M. Lundqvist, J. Stigler, G. Elia, I. Lynch, T. Cedervall, K.A. Dawson, Nanoparticle Size and Surface Properties Determine the Protein Corona with Possible Implications for Biological Impacts, Proc. Natl. Acad. Sci. U. S. A. 105 (2008) 14265-14270.

[15] T. Cedervall, I. Lynch, S. Lindman, T. Berggård, E. Thulin, H. Nilsson, K.A. Dawson, S. Linse, Understanding the Nanoparticle: Protein Corona Using Methods to Quantify Exchange Rates and Affinities of Proteins for Nanoparticles, Proc. Natl. Acad. Sci. U. S. A. 104 (2007) 2050-2055.

[16] V.M. Masalov, N.S. Sukhinina, E.A. Kudrenko, G.A. Emelchenko, Mechanism of formation and nanostructure of Stöber silica particles, Nanotechnology. 22 (2011).

[17] S. Roy, R. Woolley, B.D. MacCraith, C. McDonagh, Fluorescence lifetime analysis and fluorescence correlation spectroscopy elucidate the internal architecture of fluorescent silica nanoparticles, Langmuir. 26 (2010) 13741-13746.

[18] S.M. Kelleher, R.I. Nooney, S.P. Flynn, E. Clancy, M. Burke, S. Daly, T.J. Smith, S. Daniels, C. McDonagh, Multivalent linkers for improved covalent binding of oligonucleotides to dye-doped silica nanoparticles, Nanotechnology. 26 (2015).

[19] R.I. Nooney, A. White, C. O'Mahony, C. O'Connell, S.M. Kelleher, S. Daniels, C. McDonagh, Investigating the colloidal stability of fluorescent silica nanoparticles under isotonic conditions for biomedical applications, J. Colloid Interface Sci. 456 (2015) 50-58.

[20] R.I. Nooney, C.M.N. McCahey, O. Stranik, X. Le Guevel, C. McDonagh, B.D. MacCraith, Experimental and theoretical studies of the optimisation of fluorescence from near-infrared dye-doped silica nanoparticles, Analytical & Bioanalytical Chemistry. 393 (2009) 1143-1149.

[21] R.I. Nooney, E. McCormack, C. McDonagh, Optimization of size, morphology and colloidal stability of fluorescein dye-doped silica NPs for application in immunoassays, Anal. Bioanal. Chem. 404 (2012) 2807-2818.

[22] C.P. Tsai, C.Y. Chen, Y. Hung, F.H. Chang, C.Y. Mou, Monoclonal antibody-functionalized mesoporous silica nanoparticles (MSN) for selective targeting breast cancer cells, J. Mater. Chem. 19 (2009) 5737-5743.

[23] Y. Xu, D.C. Baiu, J.A. Sherwood, M.R. McElreath, Y. Qin, K.H. Lackey, M. Otto, Y. Bao, Linker-free conjugation and specific cell targeting of antibody functionalized iron-oxide nanoparticles, J. Mater. Chem. B. 2 (2014) 6198-6206.

[24] C.L. O'Connell, R. Nooney, C. McDonagh, Cyanine5-doped silica nanoparticles as ultra-bright immunospecific labels for model circulating tumour cells in flow cytometry and microscopy, Biosens. Bioelectron. 91 (2017) 190-198.

Chapter 5: Primary antibody nanoparticle cell staining

5.1 Introduction

There are two main techniques to stain cells or detect antigens. They are through primary or secondary antibodies (see section 2.5 for more details of the structure of antibodies and differences between primary and secondary antibodies). To summarise, primary antibodies are easy to work with, as the antibody directly binds to the target antigen. The primary antibody is labelled with dye molecules and so fluorescence measurements can easily elucidate where the antigens are positioned. Secondary antibodies require two steps. The first consists of incubating cells with an unlabelled primary antibody, and after a number of wash steps, the fluorescently labelled secondary antibody is introduced to the cells that is specific to the primary antibody. To reduce the number of variables, a primary antibody detection system was initially employed for use with NPs.

One of the motivations for carrying out this work is to benchmark the performance of the NPs against other dyes to evaluate whether they can be competitive with the conducting polymer dyes discussed in section 2.3. These labels require ultra violet or violet excitation [1,2]. APC and AlexaFluor®647 are the most common dyes used that are excited and emit in the red and in this chapter the performance of the NPs is benchmarked against these two fluorophores as they have a similar spectral range and, therefore, they do not require adjusting microscope filter sets or laser lines.

One of the challenges in using nanoparticles for targeted cell imaging or staining is the high degree of non-specific interactions between the cells and particles followed by endocytosis. The internalisation of NPs by cells can be useful for investigating pH, toxicity and drug delivery applications; however, for the work presented in this chapter, it is imperative that the nanoparticles are not absorbed or taken up non-specifically [3-5]. In this work, multiple layers were placed on the surface of the NP to reduce the effect of non-specific binding. A PEG layer was placed on the NP because PEG has been

shown to aid in reducing endocytosis [6]. In a detailed study, Rampazzo et al. investigated the use of PEG molecules on the surface of silica NPs with different charged functional groups to reduce particle up take in cells [7,8]. Results indicated that PEG only nanoparticles had reduced uptake in the cell compared to positively charged amino-PEG-NPs but that overall the highly negative carbo-PEG-NPs, were least effective at entering the cell membrane, emphasising the point that the overall negative charge of the NP helps to prevent its endocytosis.

As protein also appears to aid in prevention of endocytosis, the NPs were placed in a BSA solution after conjugation with antibody. Proteins help to stabilise NPs through the formation of a protein corona which blocks non-specific binding through steric hindrance. Cedervall et al., Monopoli et al. and Lundgvist et al., to name but a few, have studied in detail how proteins adsorb onto and desorb from the surface of NPs and the kinetic rates of such processes [9-11]. Lesniak et al. have shown that, without serum, NPs are internalised by cells much more effectively because of the lack of protein in solution and similarly Kim et al. have shown that at low concentrations of protein, NP uptake is greater than at higher concentrations [12,13].

Immunospecific direct binding NP cell staining work has been reported previously [14,15]. Yun et al. incorporated Fluorescein isothyocyanate (FITC), into silica NPs and conjugated anti-CD4 to their surface in order to detect subpopulations of leukocytes on a microchip [14]. In another study, by Tao et al., silica NPs were doped with Rubpy dye and the efficiency was investigated of the $NaIO_4$ oxidation method of conjugating antibodies to the NP compared with the glutaraldehyde method [15]. They investigated direct binding NPs as biosensors for the detection of EpCAM in colorectal cancer.

It is important to know the fate of the NPs once incubated with cells, for example, in cell staining when detecting surface markers, to ensure that the targeting antibody is functional and not endocytosed by the cell. This is also important in drug delivery, to verify that the drugs are targeting a specific cell organelle. Different microscopy methods can be used to identify where the NPs are located [13,16]. In this work, confocal fluorescence microscopy was chosen to determine the fate of NPs in both MCF-7 and HeLa cell lines, as the NPs are highly fluorescent. Staining the membrane with a different fluorophore will help identify whether the NPs are on the surface of the cell. This method also allows the position of individual and aggregate NPs to be determined

as a whole cell is imaged using scans compiled in a z-stack so that any slice through the cell can be examined for signs of internalisation.

5.2 Materials and methods

5.2.1 Materials

Purified anti-EpCAM, anti-EpCAM AlexaFluor®647, anti-EpCAM APC, were obtained from Biolegend. Wheat germ agglutinin (WGA) conjugated Oregon Green®488, ProLong® Gold antifade mountant and Hoechst 33342 Stain was obtained from Thermo Pierce. All other materials were obtained from Sigma Aldrich.

5.2.2 Cell culture

HeLa, MCF-7, PNT1A and LNCaP cells were cultured in 75 cm^2 flasks in Dulbecco's Modified Eagle's Medium (DMEM) with 10% uninactivated fetal bovine serum (FBS), 100units/mL penicillin and 100µg/mL streptomycin. Cultures were maintained at 37 °C with 5% CO$_2$. Harvesting of HeLa, MCF-7, PNT1A and LNCaP cells was carried out by incubation in 5mL 0.25% trypsin/0.1% ethylenediaminetetraacetic acid (EDTA) at 37 °C for 5 min followed by neutralization with 5mL DMEM culture medium. Cells were centrifuged at $300 \times g$ for 5 min and resuspended in supplemented DMEM culture media.

5.2.3 Immunospecific cell staining

Cells were washed twice in PBS before being resuspended into PBS containing 1% BSA and 0.05% Tween®20. They were left to incubate in the solution at room temperature for an hour while cell counting was performed on a haemocytometer. Cells were distributed so as to obtain 125,000 cells per test. Anti-EpCAM labelled NPs were added to cells that had previously been suspended in PBS containing 1% BSA and 0.05% Tween®20 and were at a concentration of 1mg/mL. 10µg or less of NPs were used per test with cells or, depending on the experiment, 3µL of anti-EpCAM AlexaFluor®647 or APC. Any other stains that were used such as the Oregon Green® 488- WGA for staining the cell membrane or Hoechst 33342 Stain for staining the nucleus were also added at this stage. 2µL of each stain (1µg/µL) was added to each test. The nanoparticles were left with the cells to incubate for 1 h at room temperature. After this, they were washed 3 times in PBS and then taken to be analysed either by flow cytometry or microscopy. For confocal microscopy, cells were fixed with paraformaldehyde for 15 min after the

incubation with NPs and washing steps. They were then washed in PBS, placed on a microscope cover slip and mounted in ProLong® Gold.

5.2.4 Microscopy

Cells were imaged using an IX71 (Olympus, Tokyo, Japan) inverted epifluorescence manual microscope with a TK-1460 colour video camera (JVC, Yokohama, Japan) and using a X-Cite series 120 excitation lamp (Excelitas Technologies Corp, MA, USA). See section 3.2.2 for the optical set up of the inverted epifluorescence microscope. Images were taken at 20x magnification and using a dapi or Cyanine5 filter cube. Confocal microscopy was carried out using a Leica TCS SP8 microscope (Leica Microsystems, Wetzlar, Germany) using an 86x oil immersion lens and hybrid detectors. The excitation source was a tuneable white light laser set at 488 nm for WGA conjugated Oregon Green® 488 and at 650 nm for Cyanine5 or AlexaFluor®647 dyes. See section 3.2.3 on optical set up and operation of a laser confocal microscope.

5.2.5 Cell imaging analysis

Images were analysed to quantify the fluorescence using Image J software. For an image of a cell in bright field, a region of interest (ROI) was selected that tightly enclosed the cell. That ROI was then superimposed over the fluorescent image, and the fluorescence measured, ensuring that the ROI in the fluorescent image corresponded to the cell from the bright field image. The raw integrated density value of the ROI was measured using the "RawIntDen" measurement in Image J, as this measurement is the sum of the grey pixel value in the region and prevents dark, background pixels, that may get incorporated in the ROI, to interfere with the measurement. A background value for each cell was obtained by taking a measurement where no cell was present with the same area as that of the measured cell. This background value was subtracted from the original cell value to give a normalised value of fluorescence from the cell.

5.2.6 Flow cytometry

Flow cytometry was carried out using a Millipore EasyCyte 8HT with loading in the form of a 96 well plate. Parameters were kept consistent between each run and include the event count 20,000, forward scatter and side scatter gain of 1.0, all fluorescence channels were at 8.0 and forward scatter threshold of 30.0. These were unchanged for both cell lines. See section 3.6 for the theory behind flow cytometry and the optical detection system for this particular flow cytometer. The median values of the measured

fluorescence was chosen for comparison purposes as the median values take into account the asymmetry or the skewness of the data plots.

The flow cytometry plots in this chapter are based on the data from the red2 fluorescence channel of the flow cytometer and represents the amount of EpCAM expression per cell and is found on the x-axis of the plots. The y-axis represents the number of cells that have the same red2 fluorescence/EpCAM expression values.

5.3 Results and discussion

5.3.1 Immunospecific staining microscopy results

In this section, antibody conjugated NP labels were incubated with EpCAM positive and negative cells to investigate specificity and brightness. The results were compared to commercially available anti-EpCAM conjugates AlexaFluor®647 and APC. Initially, the optimal concentration of NPs needed per test was determined. Three different concentrations of NPs were incubated with 125,000 cells. This optimal particle concentration was determined when the non-specific binding of the NPs to HeLa cells was minimal and confirmed using flow cytometry (see Fig C1 appendix C for example of 0.279% optimisation). As the number of particles in solution with cells increases, there is also an increase in non-specific binding, most likely due to particle-particle interactions and possibly aggregation of NPs which could effectively stick to the cell's membrane. The optimal NP mass needed per test was found to be 10μg of 0.168% and 7.5μg of 0.279% NPs. Taking the particle size into consideration the number of particles in the case of 0.168% NPs equates to 1.2×10^{11} particles for the optimal number and for 0.279% NPs, the 7.5μg equates to 1.3×10^{11} particles. This is comparable to the number of antibodies present in 3μL of dye conjugated anti-EpCAM labels where there are 5.8×10^{11} antibodies for AlexaFluor®647 and 1.4×10^{11} for APC.

Cells were viewed under the microscope to check their performance for the application of cell imaging. Both NP and red conjugate labels bound to MCF-7 cells generate high fluorescence signals, whereas almost no binding was observed on the HeLa cells (See Fig 5.1). Therefore, the NPs show high specificity in cell staining. The NPs appear to cluster into specific regions on the cell surface which is consistent with images presented by Tiernan et al. who used NIR-664 doped silica NPs to target colorectal cancer cells [17]. For the AlexaFluor®647 and, to a lesser extent, the APC conjugated antibodies in

Fig 5.1 (f) and (h), an uneven fluorescence emission signal was observed from the non-uniform distribution of EpCAM receptors. However, signal was also observed across the entire surface of the cell. It is not clear why the NP labels do not cover the entire surface, since the concentration of NP and dye conjugates added were similar and good mixing was used. It could be that the NP are binding preferentially to clusters of EpCAM receptors, which would enable more than one anti-EpCAM antibody on the NP to bind to more than one EpCAM receptor and therefore increase the overall avidity of the NP label [18]. This is because antibodies (~5-15 nm in size) appear quite small relative to the size of the NPs and, because of this size difference, could also be causing steric hindrance, preventing other NPs from binding to EpCAM receptors within the vicinity of the first receptor.
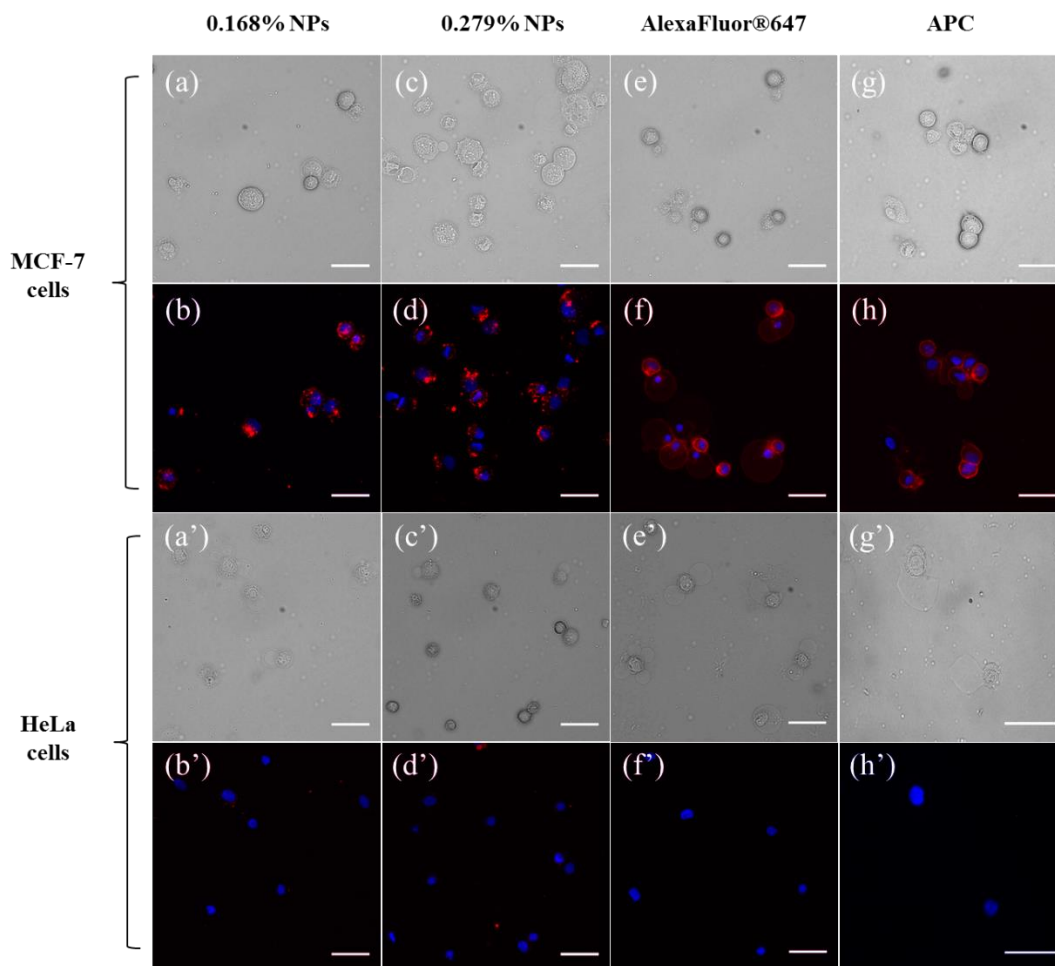
Fig 5.1: Bright field and corresponding fluorescence images of MCF-7 and HeLa cell lines incubated with different red dye anti-EpCAM conjugates. The nucleus of the cells (blue) is stained with Hoechst 33342. The scale bar represents 50µm. Previously published by the author [19].

The performance of the NPs in cell imaging was analysed quantitatively using image analysis methods and compared to that of cells stained with the other red conjugates, the results of which are summarised in Fig 5.2. The average fluorescence from Alexaflour®647 was higher than the other labels but all were similar within statistical error given the size of the error bars. The error bars are large because each cell is non-identical in size, shape and EpCAM expression, which contributes to the variability in the fluorescence from each cell. The analysis was carried out on over 50 cells from each experiment. This is still a very small sample set and to get a more accurate insight into the trend of the whole population of cells, flow cytometry was carried out and discussed in section 5.3.2.
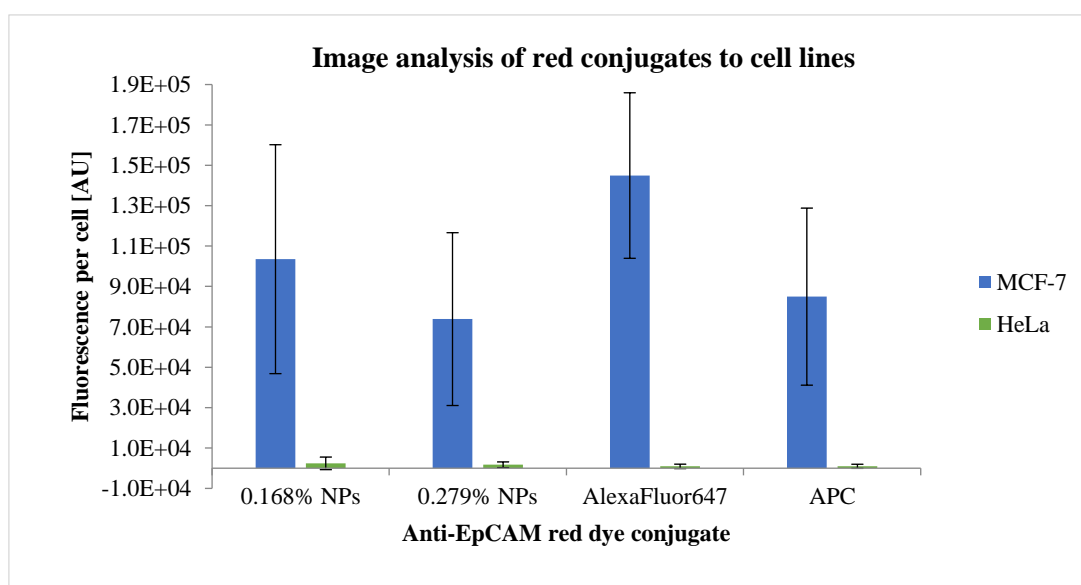
Fig 5.2: Image analysis of cell staining using anti-EpCAM red conjugates on two cell lines; MCF-7 (EpCAM +) and HeLa (EpCAM -). The analysis was carried out on over 50 cells from each experiment.

Non-specific binding, i.e., the measure of the fluorescence from HeLa cells is low not only for the antibody conjugated fluorophores but also for the two sets of NPs. This is particularly valuable in microscopy as it allows a very distinguishable positive and negative population and leaves little room for misidentification. This low non-specific binding is attributed to the functionalisation steps during synthesis and the preparation steps of the NPs before incubation with cells, in particular, zeta potential, PEGylation of NPs and protein incubation. The potential at the cell membrane for HeLa cells has been measured to be -19.4 ± 0.8 mV and is assumed to be due to the phospholipids and proteins found on the cell surface [20]. In order to prevent electrostatic attraction between the NPs and cells, the NPs must be negative. This is vital in preventing non-

specific binding and allowing specific antibody-antigen interactions. Both sets were measured and a summary of these can be found in section 4.3.2. To recap, 0.168% NPs with antibody had a zeta potential of −25.46 ± 1.85 mV and the 0.279% NPs had a potential of −8.95 ± 2.63 mV. The exact reason for variability in zeta potential between NP samples of different dye loading is not known. According to Roy et al., far red dyes are found in two distinct regions of silica NPs, at or near the surface or in the core of the particle [21]. It could be postulated that, at higher loading, the hydrophobic cyanine dye nearer the surface reduces the overall zeta potential. However, upon zeta potential measurements at the amination step, the results were similar with +8.69 ± 0.88 mV for 0.168% NPs and +12.29 ± 0.62 mV for the 0.269% NPs and thus does not appear to affect the zeta potential. Therefore, further work involving the synthesis of more NPs with varied dye loadings is required to understand the origin of these differences.

5.3.2 Flow cytometry results

Flow cytometry was performed on the Merck Millipore Guava EasyCyte 8HT system to obtain a statistically relevant set of results. Originally, the gain was optimised for APC, however after testing some NPs at this setting, they were off the scale and this required re-optimising so that all the red conjugates could be viewed at the same gain settings. Once the different gains were optimised for both cells and NPs, such as forward and side scatter, threshold and fluorescence channels, all these parameters were kept constant throughout and performed on 20,000 events for both cell lines. NPs or red conjugates were incubated with cells using the same methods that were used for cell imaging.

From the data presented in Fig. 5.3, it is clear that the nanoparticles are both bright and specific to the EpCAM positive cell line. If we view the median of the fluorescence intensity of the MCF-7 cell population, the NPs clearly outperform the antibody conjugates comparing graphs (B) or (C) to (D) or (E). The 0.168% NPs have over twice the fluorescence signal compared to APC, which is the brighter of the two commercially available conjugates for flow cytometry and the 0.279% NPs show a higher median fluorescence to the APC. The fluorescence characterisation measurements indicate that the 0.168% NPs are brighter, due to h-FRET effects, and this is reinforced in the flow cytometry results. The zeta potential of the NPs, mentioned previously in the cell staining section 5.3.1, showed that the 0.279% NPs were less negative than the 0.168%. Due to this potential, they are less likely to be repelled by the negative charge on the cell

membrane. However, as the difference is small and the antibody-antigen bond is strong, this effect is not observed.
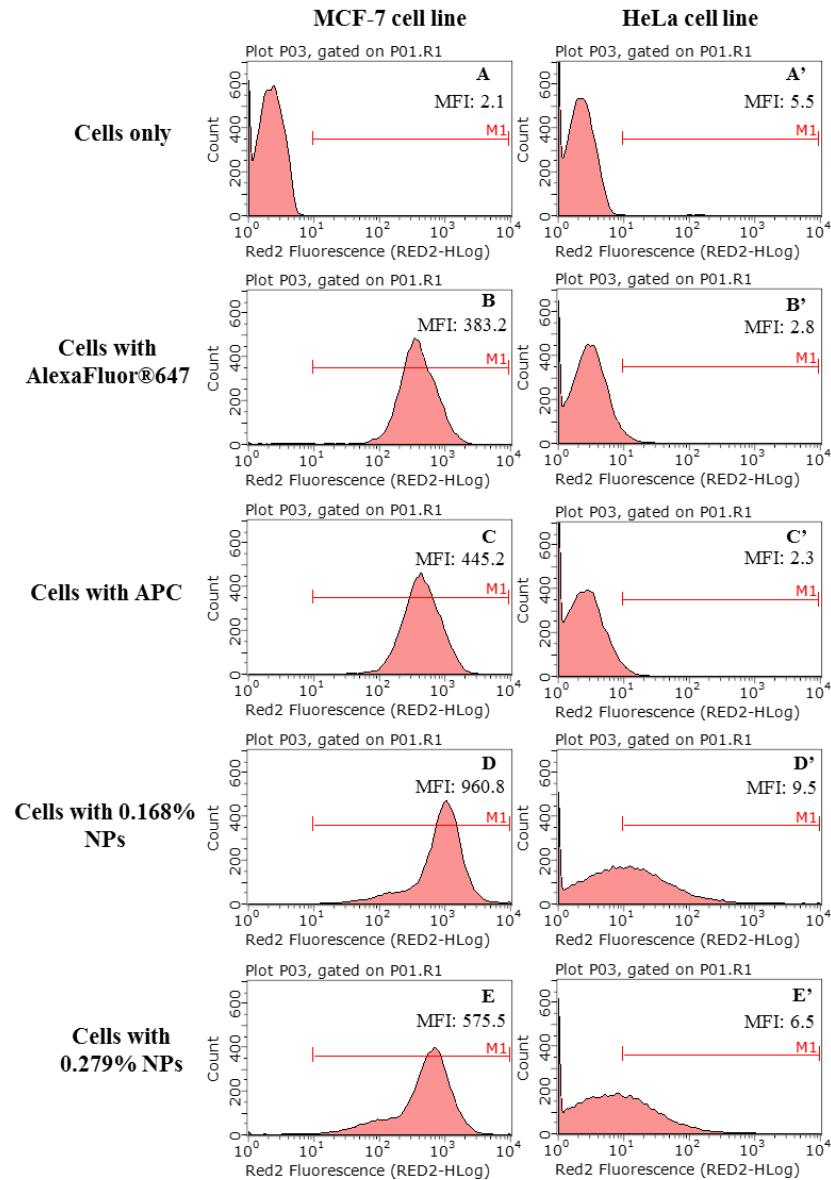
Fig 5.3: Flow cytometry results for MCF-7 cells and HeLa where the top row (A and A') are cells only and rows B-E and B'-E' correspond to cells incubated with anti-EpCAM red conjugates. MFI stands for median fluorescence intensity value. Previously published by the author [19].

Assessing non-specific binding with the HeLa cell line, from graphs D' and E' in Fig. 5.3, the cell population lies largely to the left of the region M1 and the median values almost match those obtained for APC and AlexaFluor®647. The median value for the 0.168% NPs incubated with HeLa cells is slightly higher than the 0.279% NPs and this is attributed to the brighter particle and does not imply there are more particles adhered

to the surface of the cell. As there are roughly 10^{11} particles in solution with the cell sample there is a possibility that some cells will have NPs bound to them and the results confirm this as both graphs (D') and (E') trail partially to the right. However, despite the small amount of non-specific binding, it can be concluded that the NPs are specific to the MCF-7 cells and the positive and negative cell lines' median value lies far enough apart that each population can be easily distinguished.

These results were compared to previous results reported. Yun et al. found that their anti-CD4 FITC doped NPs were approximately 50 times brighter than anti-CD4 free FITC dye [14]. As they were comparing the dye incorporated in the NPs to an antibody labelled version of the dye for analysis of subpopulations of white blood cells, the results cannot be directly compared to the work presented in this chapter. However, work more similar to this work was published by Tao et al., who conjugated anti-EpCAM to Rupby NPs for cell staining using a direct binding method [15]. Their work focused on a new antibody conjugation method using a $NaIO_4$ oxidative method compared with glutaraldehyde. They observed a tenfold increase in signal detecting the EpCAM marker from colo205, a colorectal cancer and another metastatic carcinoma, using NP labels, compared with an anti-EpCAM antibody conjugated with FITC. They achieved a signal enhancement within the same order of magnitude as is reported here and likewise, they also found low non-specific binding with an EpCAM negative cell line.

It is noted that the flow cytometry results do not exactly match those obtained from the cell imaging analysis. In imaging analysis, all red conjugates had a similar fluorescence; however, in flow cytometry the 0.168% NPs performed best closely followed by 0.279% NPs, then APC and last was AlexaFluor®647. The trend is similar in the imaging results for the two sets of NPs and the APC. However, the AlexaFluor®647 does not perform as well. Given the significantly higher number of cells that can be analysed, flow cytometry is a more statistically relevant measure of the performance of each label. Therefore, flow cytometry lends a more complete picture compared with cell microscopy in terms of quantification.

5.3.3 Location of NPs on cells using confocal microscopy

Confocal microscopy was employed to identify the location of the NPs in/on the cell and also to determine whether the NPs were aggregating on the cell surface, as is suggested from the cell staining images. If the NPs are attached to the cell surface, as is

hypothesised, they should overlap with a stain for the cell membrane. A wheat germ agglutinin (WGA) stain was chosen that was conjugated with Oregon Green® 488 dye and the cells were incubated with both this stain and the NPs for one hour at the same concentration as per the protocol for both flow cytometry and cell staining. Following this the cells were fixed and mounted to be viewed in confocal microscopy. The whole cell was imaged and reconstructed from the compilation of z-stack images and this was carried out to investigate whether the NPs were internalised by the cells in a mechanism of endocytosis and/or entrapment in an organelle.

From the images obtained from confocal, as seen in Fig. 5.4 (1a-d), the red fluorescence overlaps strongly with the green, confirming that the NPs are bound to the surface of the cell. As there is no red fluorescence in the centre of the cell (1c) there is no internalisation of the NPs. In the confocal microscopy images, there are some small regions of clustering but also significant distribution of NPs across the whole surface. There is also an uneven distribution of EpCAM receptors on the cell surface, comparing the images of the cells incubated with AlexaFluor®647 (2a-d) to those incubated with the NPs in this case, in agreement with previous microscopy images. In images (3a-d) of a HeLa cell incubated with NPs, there are only one or two NPs bound to the cell, see Fig C2 in appendix C for enlargement of HeLa cell image (3a). This demonstrates the level of nonspecific binding of NPs, which in this case, is very low. If the NPs were aggregating non-specifically, in solution phase or to NPs already bound to cell, a much higher signal from the one or two NPs that had bound to the HeLa cell would be expected to be observes, which is not the case. If this were true, it would also be noticeable in the DLS size distribution measurements. Thus, it can be concluded, that the NPs are not aggregated on the surface of the cells.
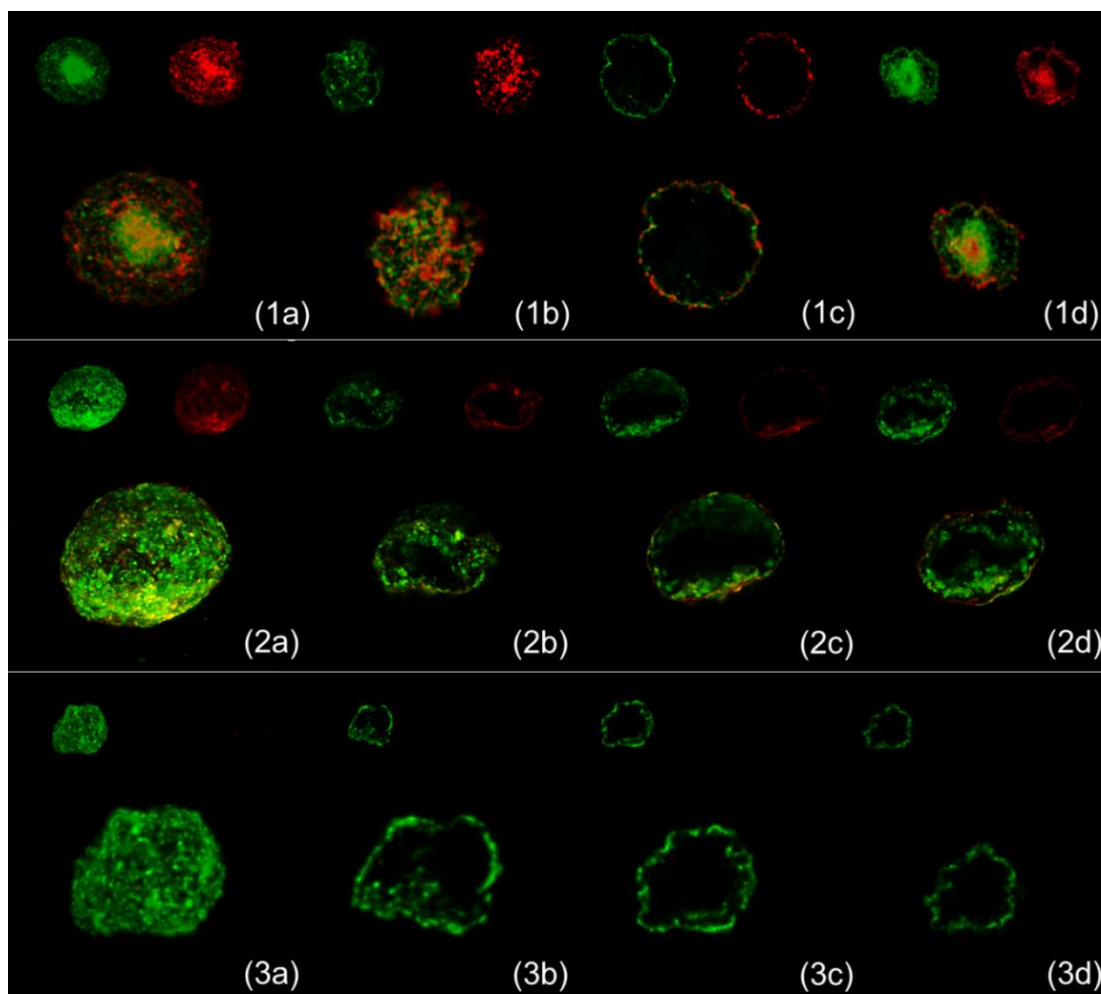
Fig 5.4: Confocal images of cells showing the location of NPs or AlexaFluor®647 (red) and cell membrane (green) using WGA conjugated Oregon Green® 488, post incubation for one hour. Column (a) shows the complete z-stack through the entire cell, (b) slice through the top of the cell, (c) slice through the centre of the cell and (d) through the bottom of the cell. Row 1 is a MCF-7 cell incubated with 0.168% NPs, row 2 is a MCF-7 cell incubated with AlexaFluor®647 and row 3 is a HeLa cell incubated with 0.168% NPs. The sample has been fixed with paraformaldehyde and cured in ProLong® Gold. Previously published by the author [19].

5.3.4 Testing of NPs on a prostate cell line

The NPs were tested on another EpCAM positive cell line to explore their applicability for use with other cell lines. This time a prostate adenocarcinoma line (LNCaP) was chosen as the EpCAM positive cell line and was compared with a prostate non-cancerous cell line, PNT1A. This cancer cell line expresses one third less EpCAM antigens than MCF-7 cells. Despite this, a high fluorescence emission signal from cells tagged with NPs would be expected [22]. The NPs and cells were tested in flow cytometry, and results are presented and discussed in this section. Cells were incubated with either 0.168% or 279% dye doped (w/w%) anti-EpCAM conjugated silica NPs or anti-EpCAM conjugated AlexaFluor®647. The methods used for flow cytometry and cell staining

were kept identical to the protocols used for MCF-7 and HeLa cell lines. The results of the flow cytometry are presented below in Fig 5.5.
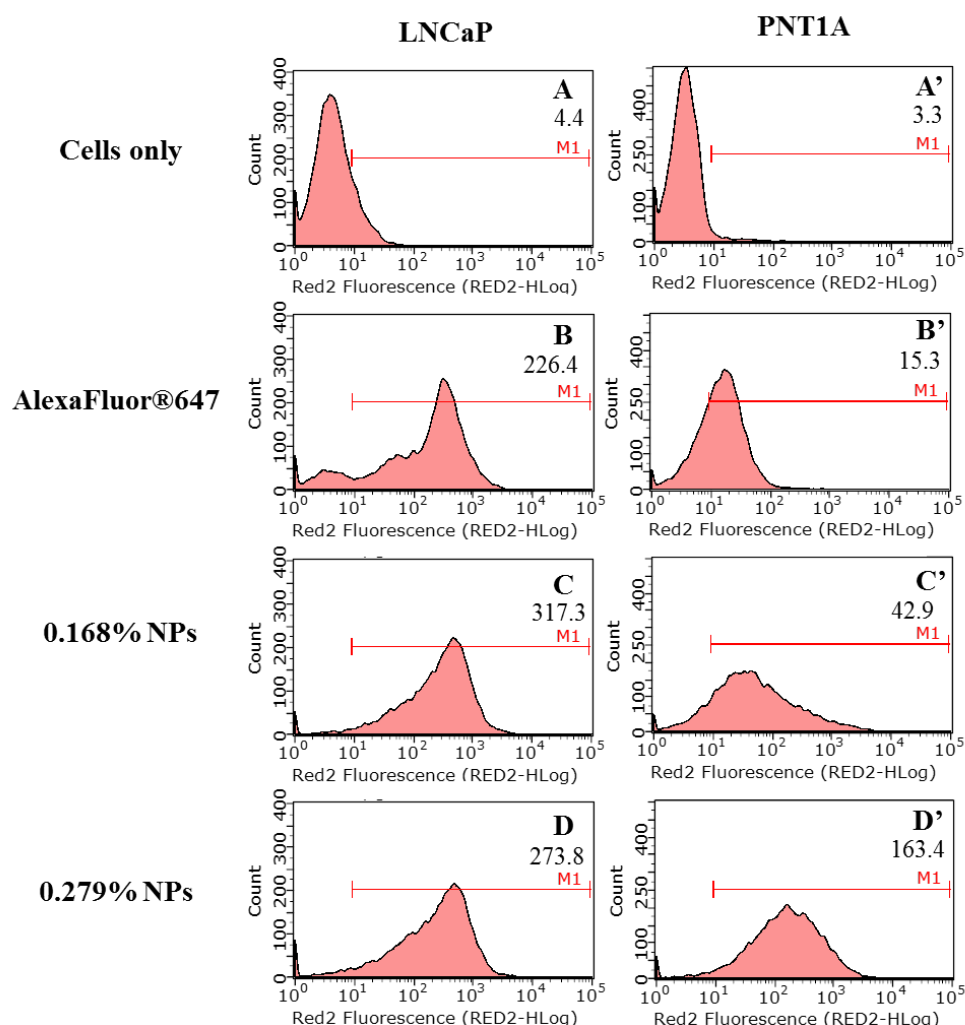
Fig 5.5: Flow cytometry results for PNT1A cells and LNCaP where the top row (A and A') are cells only and rows B-D and B'-D' correspond to cells incubated with anti-EpCAM red conjugates. The median fluorescence intensity value is written below the figure letter.

The following observations were made regarding the data from flow cytometry. Median values for both sets of NPs with LNCaP cells are higher than that of AlexaFluor®647, although, not double the signal that is observed when using the NPs with MCF-7 cells. This could be due to two main factors, one of which is that the LNCaP cells do not express as many EpCAM receptors as their MCF-7 counterparts. A study by Rao et al. found that LNCaP cells expressed 336,667 receptors compared with 509,500 on MCF-7 cells [22]. If the EpCAM receptors have grouped together, then using NPs will be a disadvantage, because two receptors in close proximity will either both be bound to one NP or another NP will be unable to bind to the second EpCAM receptor due to steric hindrance. Cells that express EpCAM in clusters and have low expression of that

particular marker will not be able to benefit fully from using nanoparticles. The second factor could be that the NPs have photobleached to some extent, but every care was taken to try and prevent this.

In terms of non-specific interactions, it can be observed from the PNT1A data that there is a higher signal from the NPs compared to AlexaFluor®647, in particular with the 0.279% NPs. The median value for PNT1A using the 0.279% NPs is 163.4 and for the LNCaP cell line 273.8. This difference is not particularly large and the overlap of the two curves would suggest that there is not much specificity from this set of NPs. Such a difference from the results of the HeLa and PNT1A cell lines was unforeseen and would suggest that several variables have changed. Some of these variables include antibody denaturation on the NPs, aggregation of the NPs in the buffer perhaps caused by denaturation of BSA in the PBS solution containing 1% BSA and 0.05% Tween and also the change in cell line may have required a re-optimisation of the concentration of NPs needed per test. Imaging of the cells can provide further insight into this and is investigated in Fig 5.6. Some potential tests that could be used to investigate which of these variables is at fault include; conjugating antibody to newly PEGylated NPs from 'as synthesised' NPs, re-titrating the concentration of NPs used in the LNCaP test and purchasing brand new BSA to use with solutions. All of these would provide an insight into what the underlying issue with the LNCaP cell line and 0.279% NPs are in this case. The 0.168% NPs, although they have a higher median than would be desired, the median fluorescent values between the EpCAM positive and negative lines are large enough to distinguish the two populations from each other. This is in line with work carried out on the MCF-7 line and appears that the 0.168% can be used for further studies with blood samples.

Some imaging was carried out also to observe the NPs on the surface of the cells and investigate whether aggregation is occurring with the 0.279% set of NPs. The immunospecific staining results are presented in Fig 5.6.
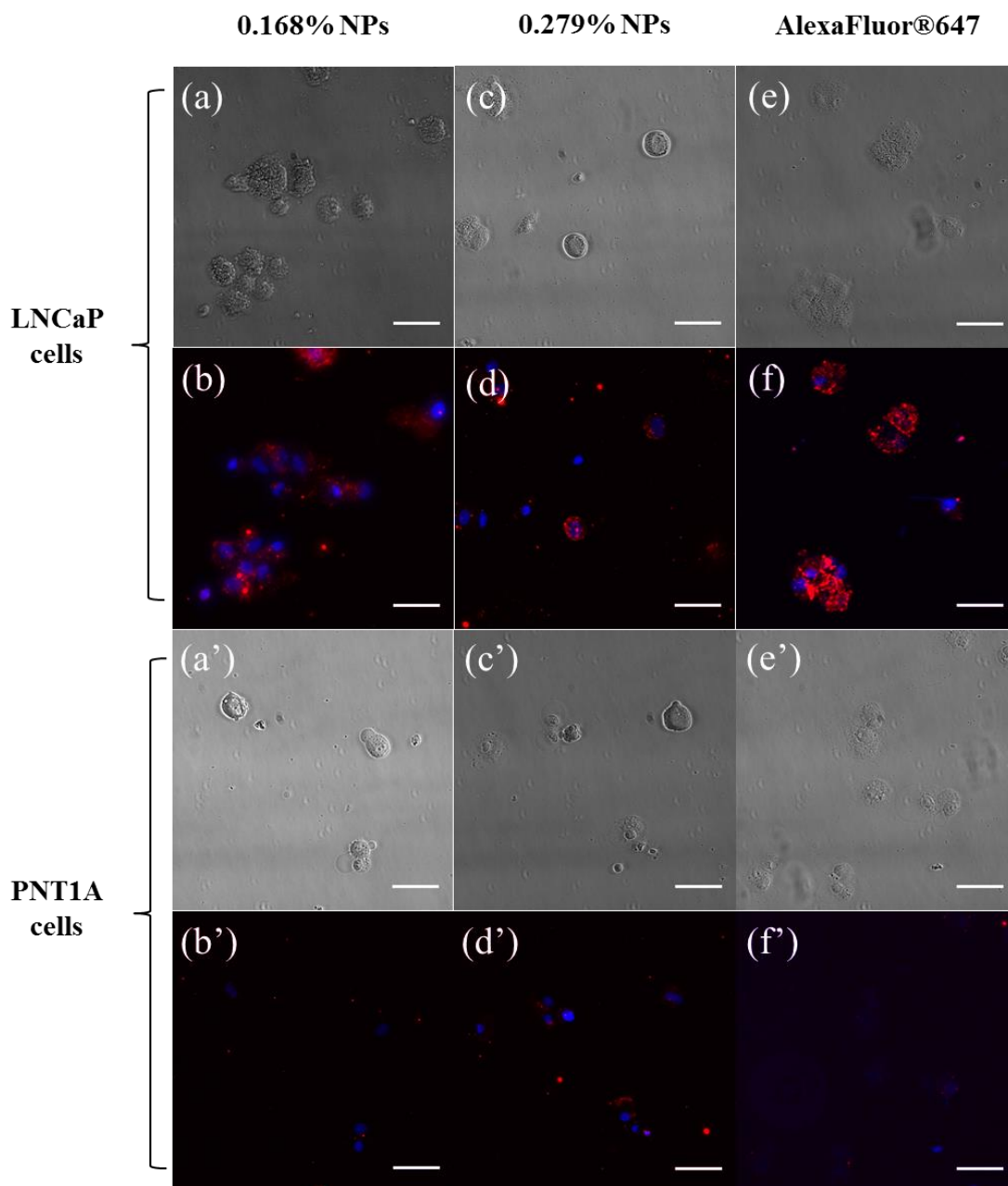
Fig 5.6: Bright field and corresponding fluorescence images of LNCaP and PNT1A cell lines incubated with different red dye anti-EpCAM conjugates. The nucleus of the cells (blue) is stained with Hoechst 33342. The scale bar represents 50µm.

Images obtained for the prostate lines are similar to those acquired for MCF-7 and HeLa cell lines. Again, small clustering spots of NPs and AlexaFluor® labels are observed on the surface of the LNCaP cell line but, as it occurs on all samples, it can be concluded that they are largely attributed to clustering of EpCAM receptors rather than aggregation of NPs. This would support the theory discussed in the previous paragraph that there is less of an amplitude in signal from using NPs than AlexaFluor®647 because of this

clustering due to steric hindrance between NP labels preventing high NP binding. Observing Fig 5.6 (d'), there are several nanoparticles adhered to the surface of PNT1A cells, clearly reflecting the results from flow cytometry of high non-specific interactions with the 0.279% NPs. The NPs appear not to be aggregating on the surface of the cells but perhaps the anti-EpCAM on the surface of the NPs has denatured for this set of NPs. There is not a clear-cut reason for this non-specific interaction but further study would have to be carried out in order to determine the exact cause.

5.4 Conclusions

Cyanine5-doped silica NPs were used for the specific tagging of model CTCs using an EpCAM surface marker target. The results from flow cytometry show that the NPs are twice as bright as the widely-used APC conjugated anti-EpCAM for MCF-7 experiments. Excellent binding specificity was also observed for the NPs in cell imaging experiments for this cell line. From confocal microscopy, it was confirmed that the NPs are not endocytosed in the time frame of a number of hours but are located on the cell surface and bound via EpCAM antibody to the EpCAM surface marker. Experiments with prostate cell lines LNCaP and PNT1A indicated that the 0.168 (w/w%) dye loaded NPs are suitable for experimentation with blood samples as they performed well on this cell line also. This work shows that the NPs can be used in the application of cell staining and could allow researchers to use commonly available dyes, which have lower quantum yields than commercial dyes, to synthesize equally bright if not brighter antibody NP labels. This could close the gap on UV-excited dyes in terms of brightness without the need to add a new excitation source as required for the conducting polymer dyes. While the specificity and brightness of the NPs has been established in buffer, the next step in this investigation is to test NP performance when incubated with real blood samples and to investigate whether the NPs will maintain their CTC targeting ability in a protein rich environment and is addressed in chapter 6.

5.5 References

[1] B. Biosciences, Relative Fluorochrome Brightness, 2016 (2014).

[2] B. Biosciences, BD Horizon Brilliant^{TM} Dyes, 2016 (2015).

[3] Y. Gao, S. Gu, Y. Zhang, X. Xie, T. Yu, Y. Lu, Y. Zhu, W. Chen, H. Zhang, H. Dong, P.J. Sinko, L. Jia, The Architecture and Function of Monoclonal Antibody-Functionalized Mesoporous Silica Nanoparticles Loaded with Mifepristone: Repurposing Abortifacient for Cancer Metastatic Chemoprevention, Small. 12 (2016) 2595-2608.

[4] W. Fan, B. Shen, W. Bu, F. Chen, Q. He, K. Zhao, S. Zhang, L. Zhou, W. Peng, Q. Xiao, D. Ni, J. Liu, J. Shi, A smart upconversion-based mesoporous silica nanotheranostic system for synergetic chemo-/radio-/photodynamic therapy and simultaneous MR/UCL imaging, Biomaterials. 35 (2014) 8992-9002.

[5] B. Korzeniowska, R. Woolley, J. DeCourcey, D. Wencel, C.E. Loscher, C. McDonagh, Intracellular pH-sensing using core/shell silica nanoparticles, J. Biomed. Nanotechnol. 10 (2014) 1336-1345.

[6] M.I. Papisov, Theoretical considerations of RES-avoiding liposomes: Molecular mechanics and chemistry of liposome interactions, Adv. Drug Deliv. Rev. 32 (1998) 119-138.

[7] E. Rampazzo, R. Voltan, L. Petrizza, N. Zaccheroni, L. Prodi, F. Casciano, G. Zauli, P. Secchiero, Proper design of silica nanoparticles combines high brightness, lack of cytotoxicity and efficient cell endocytosis, Nanoscale. 5 (2013) 7897-7905.

[8] V.C.F. Mosqueira, P. Legrand, R. Gref, B. Heurtault, M. Appel, G. Barratt, Interactions between a macrophage cell line (J774A1) and surface-modified Poly(D,L-lactide) nanocapsules bearing poly(ethylene glycol), J. Drug Targeting. 7 (1999) 65-78.

[9] M.P. Monopoli, D. Walczyk, A. Campbell, G. Elia, I. Lynch, F. Baldelli Bombelli, K.A. Dawson, Physical-Chemical aspects of protein corona: Relevance to in vitro and in vivo biological impacts of nanoparticles, J. Am. Chem. Soc. 133 (2011) 2525-2534.

[10] M. Lundqvist, J. Stigler, G. Elia, I. Lynch, T. Cedervall, K.A. Dawson, Nanoparticle Size and Surface Properties Determine the Protein Corona with Possible Implications for Biological Impacts, Proc. Natl. Acad. Sci. U. S. A. 105 (2008) 14265-14270.

[11] T. Cedervall, I. Lynch, S. Lindman, T. Berggård, E. Thulin, H. Nilsson, K.A. Dawson, S. Linse, Understanding the Nanoparticle: Protein Corona Using Methods to Quantify Exchange Rates and Affinities of Proteins for Nanoparticles, Proc. Natl. Acad. Sci. U. S. A. 104 (2007) 2050-2055.

[12] J.A. Kim, A. Salvati, C. A°berg, K.A. Dawson, Suppression of nanoparticle cytotoxicity approaching in vivo serum concentrations: Limitations of in vitro testing for nanosafety, Nanoscale. 6 (2014) 14180-14184.

[13] A. Lesniak, F. Fenaroli, M.P. Monopoli, C. Åberg, K.A. Dawson, A. Salvati, Effects of the presence or absence of a protein corona on silica nanoparticle uptake and impact on cells, ACS Nano. 6 (2012) 5845-5857.

[14] H. Yun, H. Bang, J. Min, C. Chung, J.K. Chang, D.-. Han, Simultaneous counting of two subsets of leukocytes using fluorescent silica nanoparticles in a sheathless microchip flow cytometer, Lab Chip Miniaturisation Chem. Biol. 10 (2010) 3243-3254.

[15] L. Tao, K. Zhang, Y. Sun, B. Jin, Z. Zhang, K. Yang, Anti-epithelial cell adhesion molecule monoclonal antibody conjugated fluorescent nanoparticle biosensor for sensitive detection of colon cancer cells, Biosens. Bioelectron. 35 (2012) 186-192.

[16] D. Ye, K.A. Dawson, I. Lynch, A TEM protocol for quality assurance of in vitro cellular barrier models and its application to the assessment of nanoparticle transport mechanisms across barriers, Analyst. 140 (2015) 83-97.

[17] J.P. Tiernan, N. Ingram, G. Marston, S.L. Perry, J.V. Rushworth, P.L. Coletta, P.A. Millner, D.G. Jayne, T.A. Hughes, CEA-targeted nanoparticles allow specific in vivo fluorescent imaging of colorectal cancer models, Nanomedicine. 10 (2015) 1223-1231.

[18] V. Gubala, C. Crean, R. Nooney, S. Hearty, B. McDonnell, K. Heydon, R. O'Kennedy, B.D. MacCraith, D.E. Williams, Kinetics of immunoassays with particles as labels: Effect of antibody coupling using dendrimers as linkers, Analyst. 136 (2011) 2533-2541.

[19] C.L. O'Connell, R. Nooney, C. McDonagh, Cyanine5-doped silica nanoparticles as ultra-bright immunospecific labels for model circulating tumour cells in flow cytometry and microscopy, Biosens. Bioelectron. 91 (2017) 190-198.

[20] O.V. Bondar, D.V. Saifullina, I.I. Shakhmaeva, I.I. Mavlyutova, T.I. Abdullin, Monitoring of the Zeta Potential of Human Cells upon Reduction in Their Viability and Interaction with Polymers, Acta Naturae. 4 (2012) 78-81.

[21] S. Roy, R. Woolley, B.D. MacCraith, C. McDonagh, Fluorescence lifetime analysis and fluorescence correlation spectroscopy elucidate the internal architecture of fluorescent silica nanoparticles, Langmuir. 26 (2010) 13741-13746.

[22] C.G. Rao, D. Chianese, G.V. Doyle, M.C. Miller, T. Russell, R. Sanders Jr, L. Terstappen, Expression of epithelial cell adhesion molecule in carcinoma cells present in blood and primary and metastatic tumors, Int. J. Oncol. 27 (2005) 49-57.

Chapter 6: Detection of CTCs in blood

6.1 Introduction

The previous chapters have described the functionalisation and development of NPs for the detection of antigens on the surface of cells. This chapter will address the application of detection of an antigen on a cell population within a mixed cell population, which is the next step when addressing the main research objective of the detection of CTCs from whole blood. Whole blood is abundant with proteins: in the plasma, on the surface of cells and released by cells in the blood. There have been recent investigations carried out on the adsorption kinetics of those proteins onto the surface of functionalised nanoparticles [1-5]. As blood is such a complex system, protocols for use with cyanine5-doped NPs, that were described in the previous chapters, were developed with the aim of reducing the complexity of the system. With this in mind, it was decided to lyse red blood cells, as they are not necessary for the detection of CTCs and are the largest cell population. So, to mimic patient blood samples, laboratory cultured EpCAM expressing CTCs, MCF-7s or LNCaPs, were spiked into a healthy lysed blood samples. As there are quite a large variation of the number of CTCs in a patient sample depending on stage and type of cancer, CTCs were spiked into samples at numerous ratios [6].

Some groups have investigated using dye-doped silica nanoparticles for the identification of a target cell population in a mixed cell system previously [7-10]. Tao et al. identified EpCAM positive colo205 colon cancer cells from EpCAM negative sw480 colon cancer cells using Rubpy doped silica NPs. They visualised the mixed cell population by microscope, but not by flow cytometry, and the NPs were synthesised via the microemulsion method [7]. Estevez et al. spiked Ramos human Burkitt's lymphoma cells into CEM human acute lymphoblastic leukaemia cells at different percentages and detected them using flow cytometry. This was achieved using a biotin-avidin secondary labelling system, whereby they first incubated the cells with sgc8-polyT10-biotin aptamer and then introduced neutravidin conjugated FITC doped silica NPs that were made via the Stöber method for detection of cells [8]. Another mixed cell population study by Peng et al. looked at the detection of BEL-7404 liver cancer cells from green

fluorescence protein (GFP) transfected MCF-7 cells. They spiked the liver cancer cells at a range of different ratios and detected them with galactose conjugated Rubpy-doped NPs, synthesised by the microemulsion method. The cells were analysed via flow cytometry, whereby they achieved specificity of the cells down to 1% of cell population [9]. Also in this paper, they reported the detection of the liver cancer cells from white blood cells (WBCs). They detected the BEL-7404 liver cancer cells using the galactose RuBPY silica NPs via confocal laser microscopy and distinguished them from WBCs but did not analyse the cells via flow cytometry [9]. It appears that dye-doped silica nanoparticles for the detection of CTCs from blood cells on a flow cytometry system has not been carried out previously.

6.2 Materials and methods

6.2.1 Materials

Purified anti-human EpCAM antibody, AlexaFluor®647 conjugated anti-human EpCAM and Fluorescein Isothiocyanate conjugated anti-human CD45 were obtained from BioLegend. Hoechst 33342 Stain was obtained from Thermo Pierce. BD Pharm™ Lyse (10x) and EDTA vacutainers were obtained from BD Biosciences All other materials were obtained from Sigma-Aldrich.

6.2.2 Anti-EpCAM dye-doped silica nanoparticles

Protocols for the synthesis and conjugation of anti-EpCAM to the surface of the cyanine5 doped NPs have previously been detailed in section 4.2.2 and 4.2.3. NPs used in these protocols were the previously characterised 0.168% dye-doped NPs.

6.2.3 Cell preparation and staining

Cell lines MCF-7 and LNCaP were grown in 75cm^2 flasks in DMEM containing 10% heat uninactivated FBS as described in section 5.2.2, 1% L-glutamine and 1% penicillin-streptomycin. The cells were detached from the bottom of the flask using trypsin. Cells were centrifuged (300 x g, 5 mins) and resuspended in PBS containing 1% BSA and 0.05% Tween®20. Following this, cells were counted by the haemocytometer.

A blood sample was obtained from vein and collected in an EDTA vacutainer. The sample was brought to a Coulter AcT diff2 analyser (Beckman Coulter, CA, USA), see section 3.8, where blood component analysis was performed. For this application, the

WBC count was of interest and following this the red blood cells were lysed as per protocol from BD Biosciences [11].The final solution of WBCs and platelets was suspended in PBS containing 1% BSA and 0.05% Tween®20 and the volume adjusted so that there were 125,000 WBCs per test.

CTCs, MCF-7 or LNCaP, were spiked at ratios ranging from 1:1-200:1 to simulate patient blood samples. 3µL of AlexaFluor®647 anti-EpCAM or 10µg of 0.168% anti-EpCAM NPs were added to the solution. 3µL of FITC anti-CD45 stain for WBCs were added to each test solution as a secondary distinguishing parameter. The samples were then made up to 300µL using PBS containing 1% BSA and 0.05% Tween®20. The cells were left to incubate for forty minutes before being washed twice in PBS and finally resuspended in PBS before flow cytometry analysis or microscopic imaging.

6.2.4 Flow cytometry

Cells were analysed using a Millipore Guava EasyCyte8HT instrument and InCyte™ software (see section 3.6), with blue laser and green filter, and red laser and red2 filter. Gain settings were optimised for MCF-7 and LNCaP and were kept constant throughout the run. Forward scatter and side scatter were kept constant at 5.0 and 1.0 respectively and a threshold cut off value of below 100. 30,000 events were used for the initial proof of concept low ratios and then 15,000 events were counted per test for higher ratios. Controls for flow cytometry were used to optimise green and red2 gain settings. The green settings were optimised by monitoring WBC and platelet fluorescence in a number of scenarios: (i) with no fluorophores and (ii) with only anti-CD45 and the red2 settings optimised using CTCs with (i) only anti-CD45 and (ii) with only NPs.

Flow cytometry plots in this chapter are two parameter plots. Those that are of side scatter vs forward scatter represent the relative size and granularity of cells. Where one of the axis mentions green fluorescence, this represents CD45 expression on cells and for red2 fluorescence, this represents EpCAM expression.

6.3 Results and discussion

6.3.1 Low ratio (high CTC number) proof of concept spiking tests

Experiments were carried out using either 0.168% NPs or AlexaFluor®647 to stain CTCs in a mixed cell population of WBCs, platelets and CTCs. Low ratios were tested initially to determine whether CTCs can be distinguished from WBCs as a proof of concept. As

non-specific binding was a concern, a second stain was introduced, FITC conjugated anti-CD45, which will stain only WBCs. This time, during flow cytometry, two fluorescence channels were monitored; green and red2. The green channel was optimised via a WBC and platelet sample that were stained with anti-CD45 and the red2 channel optimised using CTCs stained with 0.168% NPs. Initial ratios of 1:1 and 2:1 WBC to CTC were carried out for both MCF-7 and LNCaP cells. The results of the optimised blood, CTC and mixed cell population for MCF-7s can be seen below in Fig 6.1.
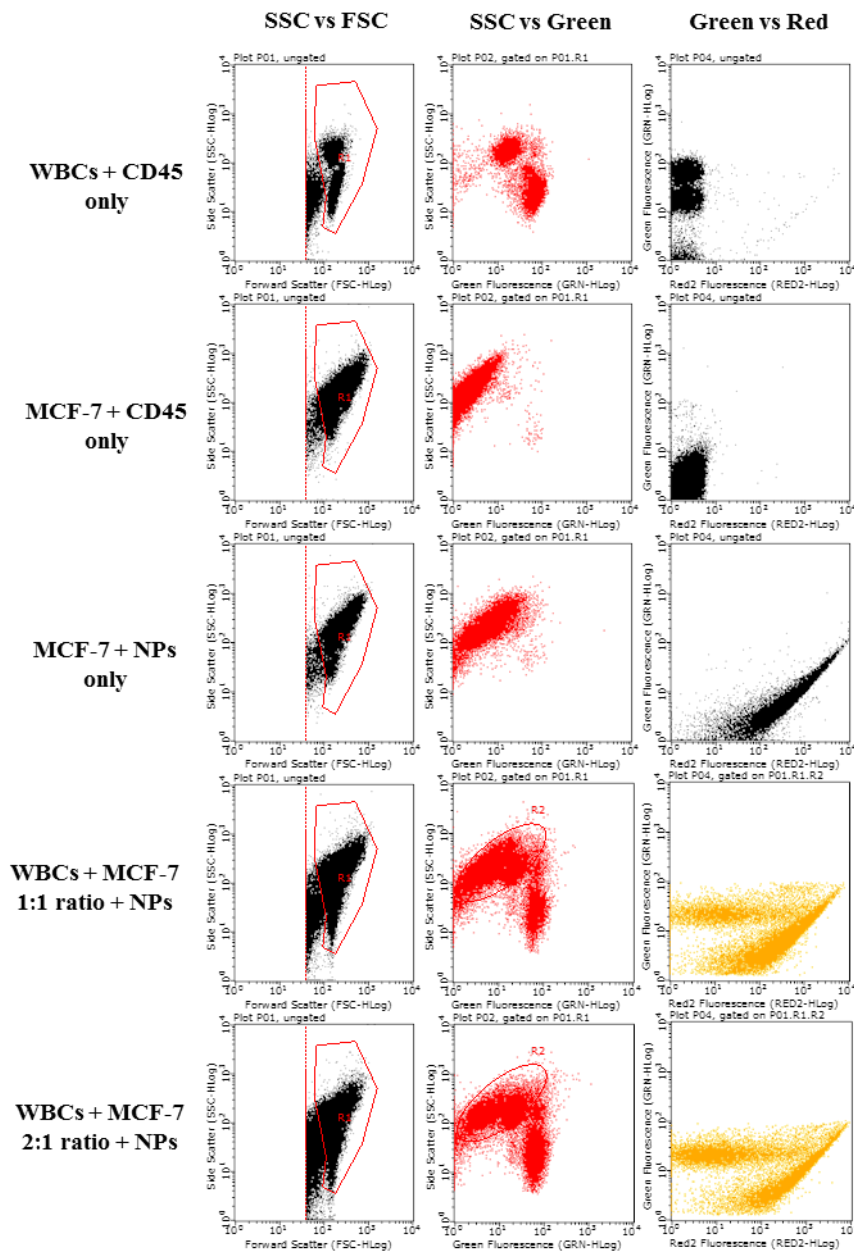
Fig 6.1 Flow cytometry plot results for WBC, platelets and MCF-7 cells incubated with anti-CD45 FITC and/or anti-EpCAM NPs.

Regions were gated in the first column plot of side scatter vs forward scatter (SSC vs FSC) to select for white blood cells and CTCs. The second column of SSC vs green fluorescence (Green) shows some distinction between CTCs and WBCs. There is some overlap between the two, as seen in row 4of Fig 6.1, and this is discussed in detail in section 6.3.2. A region was gated on the SSC vs Green plots, visible in Fig 6.1 on the 4th and 5th rows, of mixed cell population runs. This region encompasses both CTCs and some WBCs and was gated on for cells with low/no expression of anti-CD45. As granulocytes have a lower expression of anti-CD45 than monocytes or lymphocytes (the three main cell clouds observed in Fig 6.1; column 2, row 1), and there was some overlap between CTCs and this population, it was included in the gate to ensure all CTCs could be identified [12]. The final column, of green fluorescence vs red2 fluorescence is the most important column as it displays the NPs distinguishing between the two main cell populations. There are two distinct clouds of cells visible in these plots in row 4 and 5, as predicted, and there should be two if the NPs are specific to the CTCs. There appears to be some binding of the NPs to the WBCs non-specifically but using a combination of the anti-CD45 and NPs has allowed the two populations to be distinguishable, thus concluding that the NPs can be used to identify EpCAM positive CTCs at these ratios. Listed in Table 6.1 are the numbers and statistics corresponding to the plots in Fig 6.1 including CTC number and median red2 value and green median value for WBCs and CTCs.

Table 6.1: corresponding flow cytometry data for Fig 6.1 with MCF-7 cells

Sample	MCF-7 + NPs	WBC + MCF-7 1:1 ratio	WBC + MCF-7 2:1 ratio
Total cell count in R1	18755	30000	30000
CTC count in R2	-	14183	8240
Theoretical WBC ratio	-	1	2
Actual WBC ratio	-	1.12	2.64
CTC median red2 value	411.0 ± 409.8	330.6 ± 328.1	457.2 ± 471.7
CTC median green value	5.9 ± 4.9	5.5 ± 4.4	6.2 ± 5.4
WBC median red2 value in R2	-	19.9 ± 20.1	13.4 ± 21.6
WBC median green value in R2	-	21.1 ± 4.1	20.6 ± 3.9

The total cell count in each case was set to 30,000 cells within region R1, including a mixed population of WBCs and CTCs. The number of CTCs correctly identified was enumerated from the green vs red2 fluorescence plot, in which the cloud of cells with higher red2 median value and lower green value was assumed to be CTCs. For the 1:1 and 2:1 ratios, the number of CTCs recovered were close to the theoretical values and resulted in an actual ratio of 1.12:1 and 2.64:1. At both ratios, the median red2 value of the WBC cloud was 19.9 and 13.4 respectively and compared to the CTC cloud median which was 330.6 and 457.2, indicating low non-specific staining. However, what is not captured by the median value is the variability in the red2 fluorescence or 'the spread' of the cloud plot across the red2 fluorescence or x-axis. This is enumerated in the standard deviation. Ideally, there would be a dense cloud around one particular spot but that was not observed here. Despite this, the two clouds are distinguishable. The corresponding green value of the MCF-7 was similar for the two ratios and also the CTCs by themselves indicating that there is little, if no, non-specific staining of the CTCs by the anti-CD45.
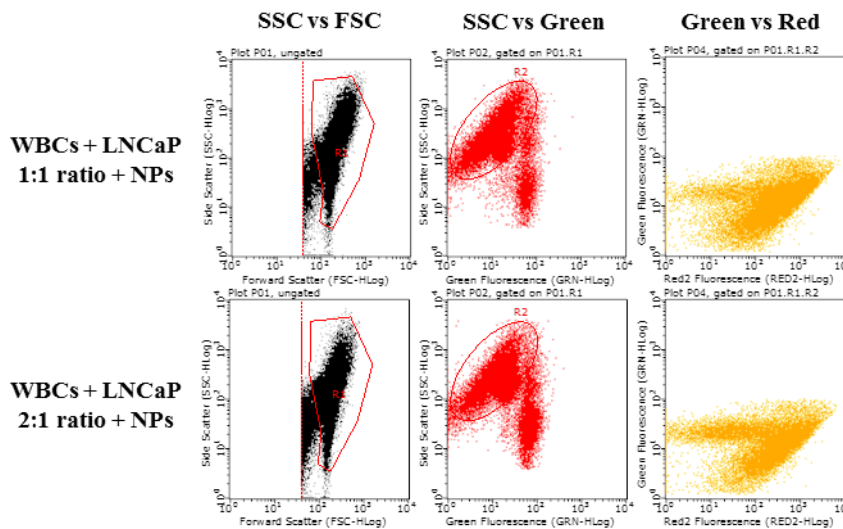
**Fig 6.2:** Flow cytometry plot results for WBC, platelets and LNCaP cells incubated with anti-CD45 FITC and anti-EpCAM NPs.

The results for LNCaP cells is not so clearly defined as those for MCF-7 cells as seen in Fig 6.2. In the third column, of green fluorescence vs red2 fluorescence plots for the two ratios, the WBC cloud is almost merged with the CTC cloud and it appears that there are fewer WBCs than CTCs. This is verified in the numbers presented in Table 6.2. The actual ratios of spiked cells were 0.72:1 and 1.32:1, as opposed to 1:1 and 2:1. The WBC cloud is more visible in the 2:1 ratio plot due to the higher numbers of WBCs in the

region R2. But, in the case of LNCaPs, there are two clouds that can be distinguished, but what is more interesting is how this evolves with higher ratios of WBCs, as explored in section 6.3.3.

Table 6.2: Flow cytometry data for Fig 6.2 with LNCaP cells

Sample	WBC + LNCaP 1:1 ratio	WBC + LNCaP 2:1 ratio
Total cell count R1	30000	30000
CTC count R2	17466	12919
Theoretical ratio	1	2
Actual ratio	0.72	1.32
CTC median red2 value	315.8 ± 283.1	322.9 ± 289.6
CTC median green value	9.9 ± 6.5	10.1 ± 6.6
WBC median red2 value R2	45.4 ± 40.6	34.1 ± 33.0
WBC median green value R2	19.1 ± 4.4	21.6 ± 4.81

6.3.2 High ratio spiking tests with MCF-7s and comparison of NPs to AlexaFluor®647

Experiments were repeated as in section 6.3.1 with higher ratios of WBCs to CTCs, ranging from 5:1-200:1, to identify the lower limit of detection of MCF-7s by the NPs. This was compared with anti-EpCAM AlexaFluor®647. WBCs were stained with anti-CD45 as a secondary parameter check of the correct identification of CTCs. Fig 6.3 shows how both NPs and AlexaFluor®647 plots were gated to determine the number of MCF-7s that were identified. These plots represent a 5:1 ratio of WBCs to MCF-7s. Region R1 represents a mix of both WBCs and CTCs. Region R2 encloses MCF-7s and some WBCs of similar side scatter. Region R3 represents the CTCs that are considered correctly identified due to their higher red2 median values.
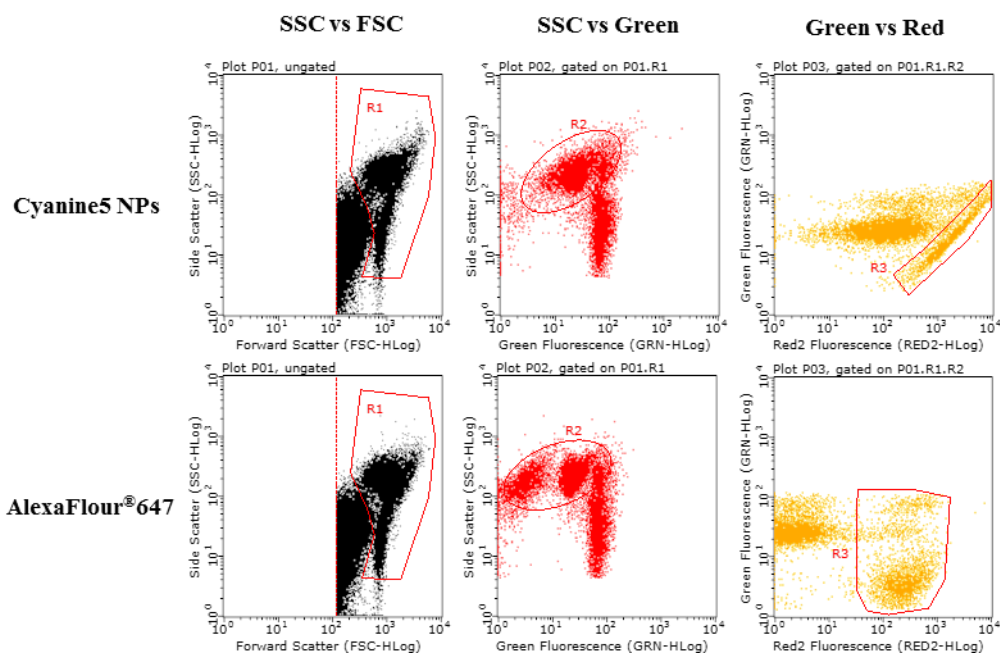
Fig 6.3: Plots of MCF-7s spiked in blood samples: side scatter (SSC) vs forward scatter (FSC) showing the gating of region R1; SSC vs green fluorescence showing gating on region R2 and green vs red2 fluorescence showing R3 assumed identification of CTCs.

Experimental data plots of green vs red2 fluorescence at 5:1-200:1 ratios with spiked MCF-7s are shown in Fig 6.4 and corresponding data for NPs and AlexaFluor®647 is shown in separate tables, Table 6.3 and 6.4. Two distinct clouds were observed for NPs at all ratios, even at ratios as low as 200:1, in the green fluorescence vs red2 fluorescence plots. For AlexaFluor®647, the cloud of identified MCF-7s is more clearly visible than for NPs. The tables include the number of MCF-7s that were identified and also displays the median green and red2 values of these cells. Also included in the tables are the green and red2 median fluorescence values for the WBCs that were in region R2 to evaluate the specificity of the NPs and AlexaFluor®647. The red2 median for WBCs was averaged over all tests with NPs in Table 6.3 and was found to be 128.9, which is almost two orders of magnitude higher than the average WBC red2 median for AlexaFluor®647 in Table 6.4, which has a value of 1.8. This implies that there is a high level of non-specific binding of NPs. However, despite this, the MCF-7s have a larger red2 median fluorescence of 2,088.8, on average, compared with 179.9 for AlexaFluor®647. For NPs, the signal from MCF-7 cells is 16 times higher than that of the WBCs and for AlexaFluor®647, it is 100 times higher. The issue with non-specific binding needs to be addressed to improve the sensitivity of the NPs.
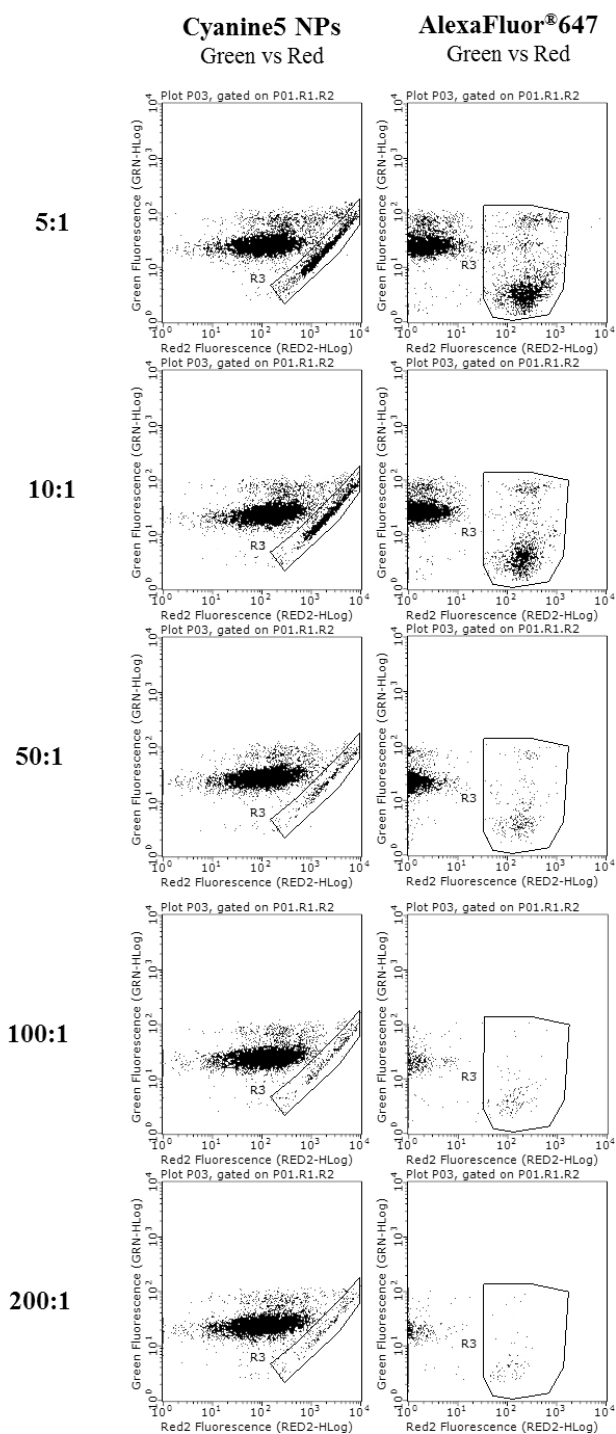
Fig 6.4: Flow cytometry green fluorescence vs red2 fluorescence plots for blood spiked at different ratios with MCF-7s and stained with either anti-EpCAM Cyanine5 NPs (left column) or AlexaFluor®647 (right column) and WBCs stained with anti-CD45. Shown in black and white to elucidate a sharper contrast.

The paper by Peng et al. had a mixed cell population study where they spiked liver cancer cells, BEL-7404, into green fluorescent protein expressing MCF-7s and incubated RuBpy NPs with the mixed cell population [9]. The cells, analysed via flow cytometry, showed the ability of the NPs to detect cells down to 1% spiking of the cell

population. This is comparable with results obtained here where MCF-7 cells can be distinguished from WBCs at a theoretical ratio of 200:1, but, in practice, resulted in an actual detection of CTCs at 50:1. Putting this in the format that Peng et al. presented in their paper, it is equivalent to a 2% detection rate.

It was observed when the MCF-7 cells were incubated with NPs that they appear to have a higher green median than when they were incubated with AlexaFluor®647. This was also observed when they were viewed under the microscope, as shown in Fig 6.5. The reason for this is inherent in the cyanine5 nanoparticle itself. UV-vis has shown there to be a small absorption peak in the region of 460-490nm, (please see Fig D1 in appendix D), that is not present in either Cyanine5 free dye or pure silica nanoparticles. This was also observed previously in other work and the reason for this peak has been concluded to be the interaction and aggregation of dye with surfactants during the nanoparticle synthesis process [13,14]. The blue laser in the flow cytometer excites fluorophores at 488nm, which lies exactly within this band and produces some fluorescence, as seen in Fig D2 in appendix D.

There appears to be some amount of non-specific binding of the anti-CD45 in conjunction with the green emission of the NPs, and is most visible in the 5:1 and 10:1 plots of AlexaFluor®647 in Fig 6.4, in which some cells are stained both with NPs and anti-CD45 as seen in the small clouds above the main MCF-7 cloud. A combination of non-specific anti-CD45 and green emission from the NPs contribute to the higher green median fluorescence observed for NP samples in flow cytometry.

Table 6.3: Data results for spiked MCF-7s using cyanine5 NPs at different ratios

Sample with cyanine5 NPs	5:1	10:1	50:1	100:1	200:1
Total Count R1	15000	15000	15000	15000	15000
Total CTC count R3	2019	1443	501	392	289
Theoretical WBC ratio	5	10	50	100	200
Actual WBC ratio	6.4	9.4	28.9	37.3	50.9
CTC median red2 value	1550.0 ± 1304.6	2204.7 ± 1603.7	2229.7 ± 1634.6	2438.8 ± 1697.9	2020.6 ± 1526.2
CTC median green value	16.9 ± 14.6	22.4 ± 17.0	25.4 ± 18.8	26.8 ± 19.8	24.1 ± 18.0
WBC median red2 value in R2	125.9 ± 94.3	150.8 ± 105.8	119.8 ± 91.8	128.9 ± 98.1	118.9 ± 931.2
WBC median green value in R2	24.9 ± 5.4	22.8 ± 5.2	26.4 ± 5.4	24.0 ± 5.1	23.6 ± 5.2

Table 6.4: Data results for spiked MCF-7s at different ratios using AlexaFluor®647

Sample with AlexaFluor®647	5:1	10:1	50:1	100:1	200:1
Total Count R1	15000	15000	15000	15000	15000
Total CTC count R3	2937	1858	493	180	117
Theoretical WBC ratio	5	10	50	100	200
Actual WBC ratio	4.1	7.1	29.4	82.3	127.2
CTC median red2 value	240.4 ± 174.1	213.7 ± 138.7	181.2 ± 120.8	143.4 ± 87.8	120.6 ± 62.8
CTC median green value	4.1 ± 6.6	4.3 ± 6.8	4.6 ± 7.6	4.1 ± 7.5	4.4 ± 7.3
WBC median red2 value in R2	2.4 ± 1.5	2.0 ± 1.3	1.5 ± 1.1	1.6 ± 1.2	1.5 ± 1.1
WBC median green value in R2	24.5 ± 7.3	25.3 ± 7.1	21.3 ± 6.2	21.4 ± 6.3	19.2 ± 5.9

6.3.2.1 Imaging of MCF-7 spiked blood cells

Shown in Fig 6.5 are the corresponding brightfield and fluorescence images obtained from preparing the cells under the same conditions used for spiked blood flow cytometry experiments using MCF-7 cells with NPs and AlexaFluor®647. Images were made of 5:1, 10:1 and 50:1 samples. The WBCs are shown stained green with FITC conjugated anti-CD45 and MCF-7s are in red and their nucleus is shown in blue, stained with Hoechst 33342.
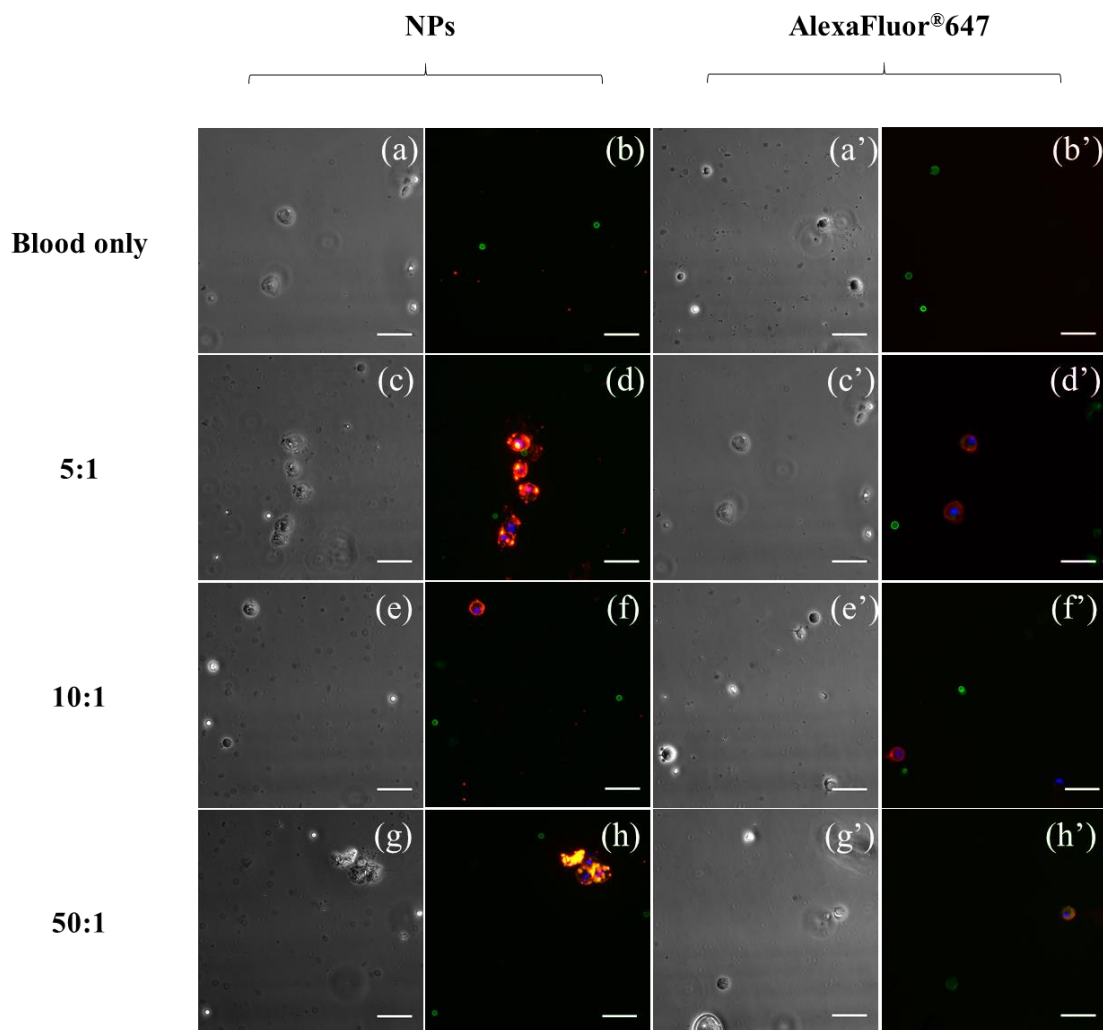
Fig 6.5: Images of MCF-7s spiked in blood cells at three different ratios. WBCs stained green with FITC anti-CD45 and MCF-7s stained red with anti-EpCAM NPs or AlexaFluor®647. Nucleus stained blue with Hoechst 33342 and scale bar is 50μm.

One of the most interesting features to note in these images is the lack of red stain on the WBCs. This is a good thing, because, visually, the WBCs are very distinguishable from the CTCs, which of course is the overall aim of this work. The other is the fact the MCF-7s, particularly those stained with NPs, appear to be yellow due to the mixing of

wavelengths from green and red. This corresponds to the inherent green emission of the NPs from the Cyanine5 dye-surfactant aggregation discussed earlier in section 6.3.2 and is visible in Fig 6.5 (d) and (h). This can be observed in these images due to the presence of the FITC filter cube which has an excitation band of 475 ± 17.5 nm and emission of 530 ± 21.5 nm. The non-specific staining of the anti-CD45, can be observed most notably in Fig 6.5 (h'), in which the AlexaFluor®647 does not emit in the green and most likely also contributes to the green emission for NP samples.

6.3.3 High ratio spiking tests with LNCaP cells and comparison of NPs to AlexaFluor®647

The experiments reported in section 6.3.2 were repeated with a different cancer cell line, LNCaP, which were spiked into WBCs and platelets at increasing ratios from 5:1 to 200:1, as in the previous section. Fig 6.6 shows how both NPs and AlexaFluor®647 were gated on R1; SSC vs FSC for WBCs and CTCs, R2; SSC vs Green for CTCs and some WBCs and R3; assumed CTCs.
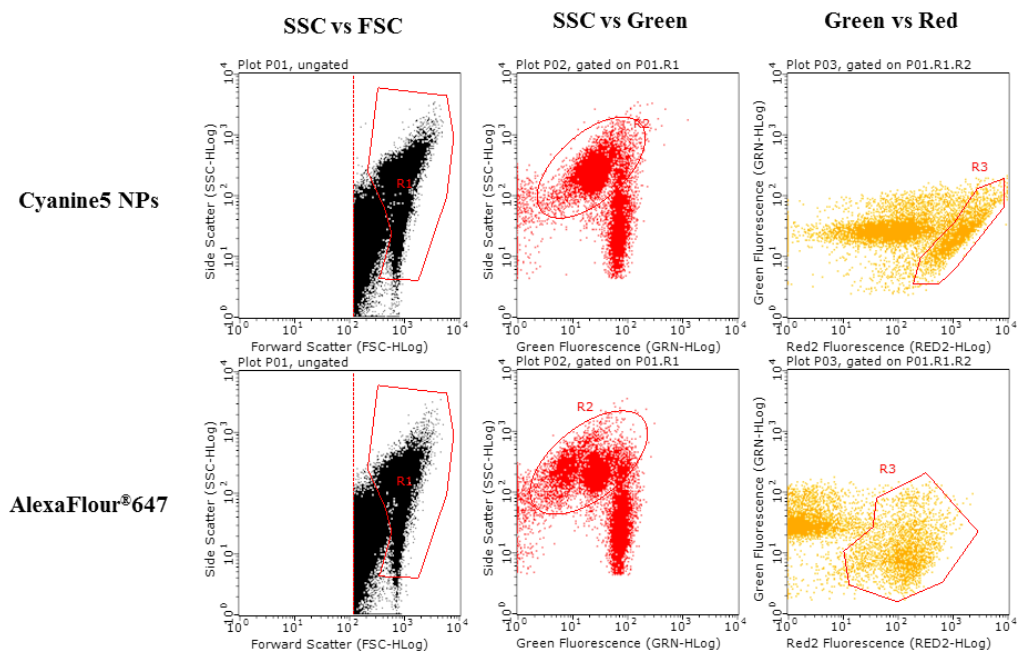
Fig 6.6: Plots of LNCaPs spiked in blood samples: side scatter (SSC) vs forward scatter (FSC) showing the gating of region R1; SSC vs green fluorescence showing gating on region R2 and green vs red2 fluorescence showing R3 assumed identification of CTCs.

Fig 6.7 shows plots of green fluorescence vs red2 fluorescence for both NPs and AlexaFluor®647 at each ratio 5:1-200:1. For NPs, two clouds can be observed again for WBCs and CTCs and a more distinct CTC cloud for AlexaFluor®647. Tables 6.5 and 6.6 show the data corresponding to the plots in Fig 6.7. The average red2 median for

WBCs across all ratios that were incubated with NPs from Table 6.5 is 88.5, which corresponds to the level of non-specific binding of the NPs and from Table 6.6 the average red2 median fluorescence value was 1.0 for AlexaFluor®647. This is compared with the average red2 median value of LNCaPs incubated with NPs of 1349.5 and with AlexaFluor®647 119.6. Spiked LNCaPs exhibit a 15.2-fold increase in signal from WBCs when using NPs and 119.6 with AlexaFluor®647 which is the same order of magnitude difference as was achieved previously in section 6.3.2 with MCF-7 cells.

As was the case for MCF-7 cells, with LNCaP cells, there is a higher green median value due to the emission of the NPs at green wavelengths, which can be seen in the SSC vs green plot in Fig 6.6. There is some non-specific staining of the anti-CD45 visible in the 5:1 and 10:1 ratio plots of Fig 6.7 with AlexaFluor®647 where cells are stained both green and red again.
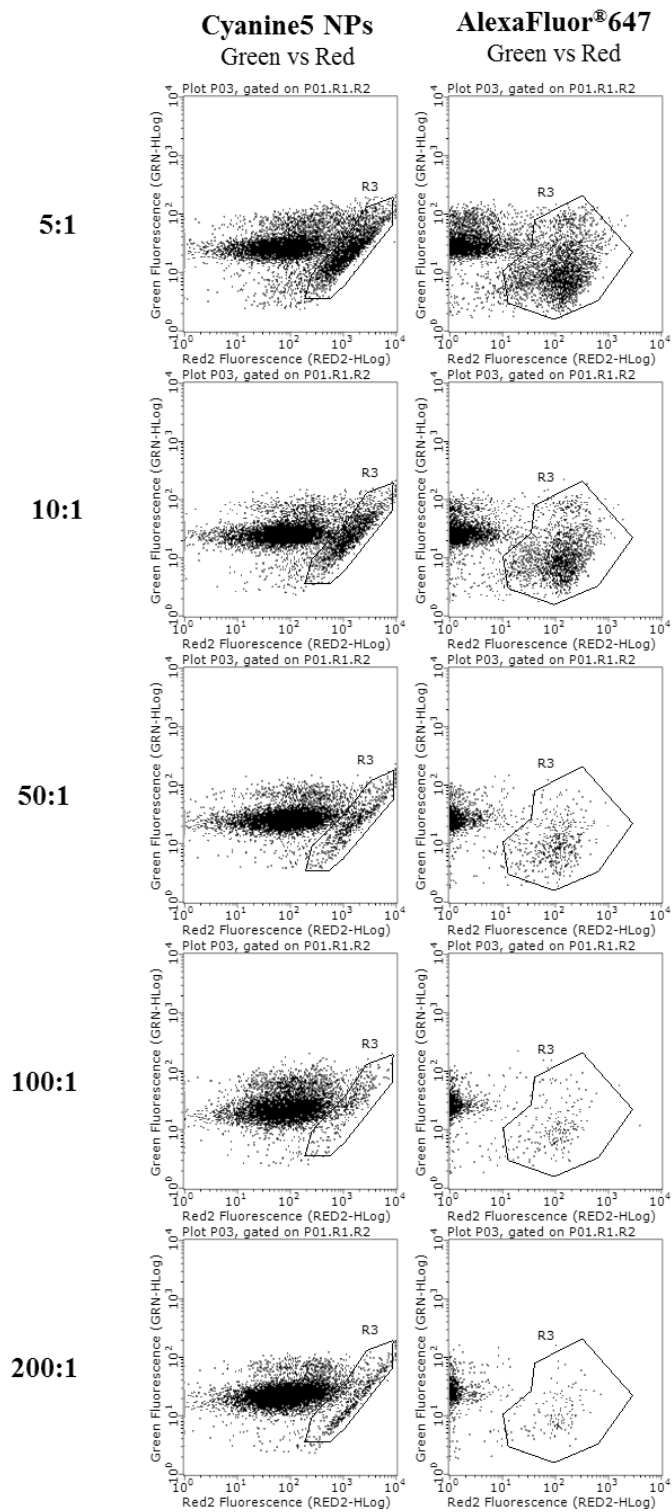
Fig 6.7: Flow cytometry green fluorescence vs red2 fluorescence plots of LNCaPs spiked in to blood at different ratios stained with anti-EpCAM NPs (left) or AlexaFluor®647 (right). Shown in black and white to elucidate a sharper contrast.

Table 6.5: Data results for spiked LNCaP cells in blood at different ratios and stained with cyanine5 NPs

Sample with cyanine5 NPs	5:1	10:1	50:1	100:1	200:1
Total Count R1	15000	15000	15000	15000	15000
Total CTC count R3	2509	1695	776	408	689
Theoretical WBC ratio	5	10	50	100	200
Actual WBC ratio	5.0	7.8	18.3	35.8	20.8
CTC median red2 value	1280.2 ± 940.4	1363.3 ± 926.5	1494.0 ± 1015.2	1341.8 ± 845.2	1268.4 ± 840.9
CTC median green value	22.0 ± 13.4	23.0 ± 13.0	24.4 ± 12.9	25.5 ± 12.2	20.7 ± 12.3
WBC median red2 value	81.6 ± 62.3	85.4 ± 63.6	98.6 ± 71.6	90.5 ± 66.1	86.3 ± 66.2
WBC median green value	25.0 ± 5.4	24.3 ± 5.2	24.9 ± 5.2	20.9 ± 4.8	21.8 ± 4.7

Table 6.6: Data corresponding to LNCaP spiked into blood at different ratios and stained with AlexaFluor®647

Sample with AlexaFluor®647	5:1	10:1	50:1	100:1	200:1
Total Count R1	15000	15000	15000	15000	15000
Total CTC count R3	2981	1924	486	206	129
Theoretical WBC ratio	5	10	50	100	200
Actual WBC ratio	4.0	6.8	29.9	71.8	115.3
CTC median red2 value	137.6 ± 108.0	135.0 ± 97.6	105.8 ± 77.0	107.4 ± 73.4	112.3 ± 8.08
CTC median green value	9.6 ± 10.3	9.1 ± 10.3	8.9 ± 8.2	9.6 ± 10.9	9.8 ± 7.7
WBC median red2 value	1.2 ± 0.9	1.0 ± 0.7	1.0 ± 0.7	1.0 ± 0.7	1.0 ± 0.7
WBC median green value	27.4 ± 7.4	25.0 ± 7.0	25.3 ± 6.6	25.1 ± 6.7	24.6 ± 6.7

6.3.3.1 LNCaP spiked blood cell images

Images were obtained for cells that were spiked at 5:1, 10:1 and 50:1 using NPs and AlexaFluor®647 to stain CTCs and are presented in Fig 6.8. Again, in these images there appears to be no NPs bound to the WBCs. There is some yellow colour appearing in Fig 6.8 (f) from the emission of the NPs in green. The non-specific staining of the anti-CD45, mentioned in section 6.3.2, with AlexaFluor®647 is visible, particularly, in Fig 6.8 (d') and (f').
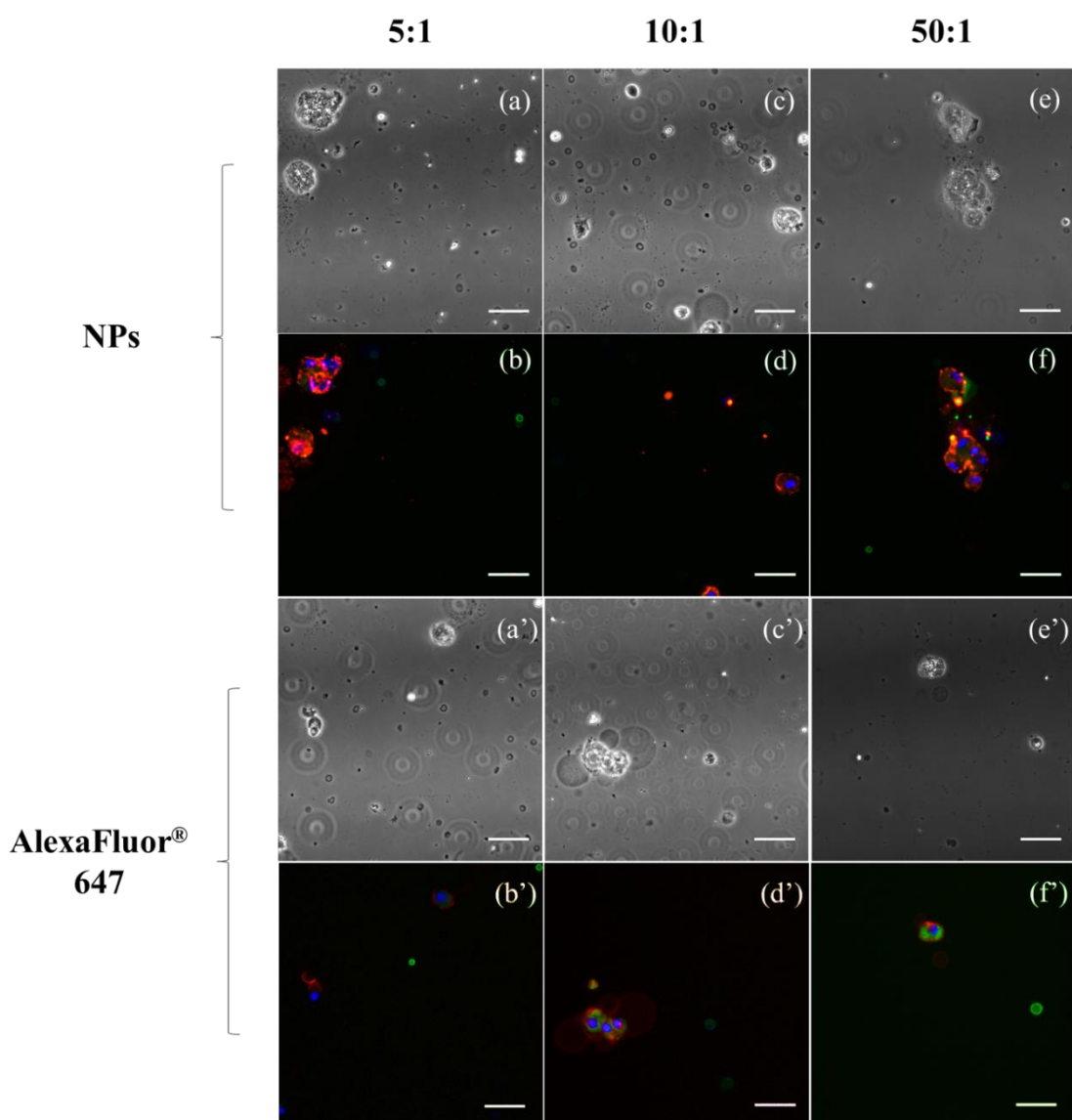
Fig 6.8: Images of LNCaP spiked in blood cells at three different ratios. WBCs stained green with FITC anti-CD45 and LNCaPs stained red with anti-EpCAM NPs or AlexaFluor®647. Nucleus stained blue with Hoechst 33342 and scale bar is 50µm.

6.4 Conclusions

Staining with 0.168% w/w Cyanine5-doped NPs enabled distinction between white blood cells and CTCs via EpCAM surface marker. Initial low ratios looked promising for both MCF-7s and LNCaPs that were spiked in with WBCs and platelets. The NPs could distinguish the CTCs down to actual ratios of ~50:1 for MCF-7 cells and 20:1 for LNCaP cells compared with 127:1 and 115:1 respectively for AlexaFluor®647. Imaging experiments show little or no binding on the surface of white blood cells. Further work must be done in order to improve specificity of the NPs, but, as it stands, they show a good potential for the application at hand for the detection of CTCs from blood.

6.5 References

[1] A. Lesniak, F. Fenaroli, M.P. Monopoli, C. Åberg, K.A. Dawson, A. Salvati, Effects of the presence or absence of a protein corona on silica nanoparticle uptake and impact on cells, ACS Nano. 6 (2012) 5845-5857.

[2] M. Lundqvist, J. Stigler, G. Elia, I. Lynch, T. Cedervall, K.A. Dawson, Nanoparticle Size and Surface Properties Determine the Protein Corona with Possible Implications for Biological Impacts, Proc. Natl. Acad. Sci. U. S. A. 105 (2008) 14265-14270.

[3] M.P. Monopoli, D. Walczyk, A. Campbell, G. Elia, I. Lynch, F. Baldelli Bombelli, K.A. Dawson, Physical-Chemical aspects of protein corona: Relevance to in vitro and in vivo biological impacts of nanoparticles, J. Am. Chem. Soc. 133 (2011) 2525-2534.

[4] T. Cedervall, I. Lynch, S. Lindman, T. Berggård, E. Thulin, H. Nilsson, K.A. Dawson, S. Linse, Understanding the Nanoparticle: Protein Corona Using Methods to Quantify Exchange Rates and Affinities of Proteins for Nanoparticles, Proc. Natl. Acad. Sci. U. S. A. 104 (2007) 2050-2055.

[5] A. Salvati, A.S. Pitek, M.P. Monopoli, K. Prapainop, F.B. Bombelli, D.R. Hristov, P.M. Kelly, C. Åberg, E. Mahon, K.A. Dawson, Transferrin-functionalized nanoparticles lose their targeting capabilities when a biomolecule corona adsorbs on the surface, Nat. Nanotechnol. 8 (2013) 137-143.

[6] S. Nagrath, L.V. Sequist, S. Maheswaran, D.W. Bell, D. Irimia, L. Ulkus, M.R. Smith, E.L. Kwak, S. Digumarthy, A. Muzikansky, P. Ryan, U.J. Balis, R.G. Tompkins, D.A. Haber, M. Toner, Isolation of rare circulating tumour cells in cancer patients by microchip technology, Nature. 450 (2007) 1235-1239.

[7] L. Tao, K. Zhang, Y. Sun, B. Jin, Z. Zhang, K. Yang, Anti-epithelial cell adhesion molecule monoclonal antibody conjugated fluorescent nanoparticle biosensor for sensitive detection of colon cancer cells, Biosens. Bioelectron. 35 (2012) 186-192.

[8] M.-. Estévez, M.B. O'Donoghue, X. Chen, W. Tan, Highly fluorescent dye-doped silica nanoparticles increase flow cytometry sensitivity for cancer cell monitoring, Nano. Res. 2 (2009) 448-461.

[9] J. Peng, K. Wang, W. Tan, X. He, C. He, P. Wu, F. Liu, Identification of live liver cancer cells in a mixed cell system using galactose-conjugated fluorescent nanoparticles, Talanta. 71 (2007) 833-840.

[10] H. Yun, H. Bang, J. Min, C. Chung, J.K. Chang, D.-. Han, Simultaneous counting of two subsets of leukocytes using fluorescent silica nanoparticles in a sheathless microchip flow cytometer, Lab Chip Miniaturisation Chem. Biol. 10 (2010) 3243-3254.

[11] B.D. Biosciences, Lysing buffer recommended assay, 2017 (2017).

[12] M. Im, H. Chae, T. Kim, H.-. Park, J. Lim, E.-. Oh, Y. Kim, Y.-. Park, K. Han, Comparative quantitative analysis of cluster of differentiation 45 antigen expression on lymphocyte subsets, Kor. J. Lab. Med. 31 (2011) 148-153.

[13] R. Nooney, C. O'Connell, S. Roy, K. Boland, G. Keegan, S. Kelleher, S. Daniels, C. McDonagh, Synthesis and characterisation of far-red fluorescent cyanine dye doped silica nanoparticles using a modified microemulsion method for application in bioassays, Sens Actuators, B Chem. 221 (2015) 420-479.

[14] S.J. Khouri, V. Buss, Circular dichroism and derivative spectra study of the excitonic aggregation of pinacyanol by aerosol-OT, Open Journal of Physical Chemistry. 2 (2012) 34-40.

Chapter 7: Secondary antibody cell staining

7.1 Introduction

Secondary antibody approaches are employed in cell staining when antigens or receptors are expressed in low numbers. Secondary assays, in principle, are more sensitive because multiple secondary labels can bind to the primary antibody and also the primary antibody is not modified through bioconjugation with a label (see section 2.5 for more detail about secondary antibody systems). To summarise, there are two types of secondary staining detection systems; antibody-antibody systems, and biotin-avidin detection system. As the work on conjugation of antibodies to the surface of the NPs has been characterised in previous chapters and is well established, an antibody-antibody system was chosen in this case. The primary antibody was a mouse anti-human EpCAM, the same as used in chapter 5 and the secondary antibody was a goat anti-mouse IgG. NPs were labelled with goat anti-mouse IgG as the secondary label and compared with commercially available goat anti-mouse AlexaFluor®647.

Previous nanoparticle work in relation to secondary antibody staining has been carried out by a few groups to detect cancer cells. Chen et al. doped silica nanoparticles with FITC or rhodamine B isothiocyanate and conjugated goat anti-rabbit IgG on their surface to detect a rabbit-anti-EpCAM antibody on the surface of Sk-Br-3 breast cancer cells [1]. They used cells incubated with NPs and no primary antibody as a control but did not compare their staining capabilities to commercially available dyes.

Estéves et al. used fluorescein or Rubpy dye-doped silica NPs coated with NeutrAvidin to detect T-cell leukemic CEM cells [2]. Cells were incubated with biotinylated anti-PTK7 antibody first and NeutrAvidin NPs were added to detect the antibody. The NP label had a signal increase of two orders of magnitude compared to a primary antibody anti-PTK7 AlexaFluor®488 control stain. As the work presented in this chapter

compares secondary labelling to a secondary stain control, it is not expected that the same level of enhancement will be observed in these experiments.

7.2 Materials and methods

7.2.1 Materials

Purified anti-human EpCAM antibody, purified goat anti-mouse IgG antibody and AlexaFluor®647 labelled goat anti-Mouse IgG were obtained from BioLegend. Hoechst 33342 Stain was obtained from Thermo Pierce. All other materials were obtained from Sigma-Aldrich.

7.2.2 Goat anti-mouse IgG NPs

Following the same protocol reported in chapter 4.2.2 and 4.2.3 for the synthesis of dye doped NPs and coating with antibody, the NPs were coated with goat anti-mouse IgG for use in secondary analysis. 2mg of PEGylated NPs were reacted with 50 mM EDC and 12.5 mM sulfo-NHS in MES pH 4.7 buffer for 15 min and were then left to react with 214µg of antibody in 0.1 M MES pH 7.2 buffer for 24 h. After this, the NPs were resuspended in PBS containing 1% BSA for 24 h before being washed in PBS three times and finally placed into PBS containing 1% BSA, 0.05% Tween®20 and 0.01% sodium azide for short term storage at 4 °C.

7.2.3 Direct binding immunoassay

Cascade concentrations of mouse anti-human EpCAM were completed using serial dilution in PBS beginning at a concentration of 20mg/mL. 50µL of each concentration were then added to each well of a 96 well Maxisorb™ black Nunc™ assay plates. The plate was then tapped at the side to ensure the solution filled across the bottom of each well. To enable attachment of the antibody to the bottom of each well the plate was incubated in the oven for 1 hour at 37.5°C. The plate was then tapped to remove excess anti-EpCAM. Plate blocking solution, comprised of PBS with 1% BSA, 10% Tween®20, was added to each well. The plate was then returned to the oven at 37.5 °C for another hour. To remove any non-adsorbed antibody and excess block, the plate was then rinsed three times with PBS containing 0.1% Tween®20 and then three times with PBS. Following this, 50µL aliquots of goat anti-mouse IgG NPs (1mg/mL concentration) in PBS containing 1% BSA and 0.05% Tween®20 were added to each well for one hour

(no spin down or wash steps of NPs before adding to the assay plate) and further incubation at 37.5 °C for another hour. The plate was then rinsed three times with PBS containing 0.1 % Tween®20 and then three times with PBS and placed in the Tecan microplate reader for further analysis. The experiment was carried out in triplicate. A similar protocol for sandwich assay detection was used previously [3].

7.2.4 Cell preparation and staining

Cell lines HeLa, MCF-7, PNT1A and LNCaP were grown in 75cm^2 flasks in DMEM containing 10% heat uninactivated FBS, 1% L-glutamine and 1% penicillin-streptomycin. The cells were detached from the bottom of the flask using trypsin. Cells were centrifuged (300xg, 5 minutes) and resuspended in PBS containing 1% BSA and 0.05% Tween®20. Following this, cells were counted on the hemacytometer and the final solution was adjusted so that there were 125,000 cells per test. Primary antibody, anti-human EpCAM (CD326) was added at 1.25mg per test and incubated for an hour with cells. After this, cells were centrifuged and washed twice in PBS and finally resuspended in PBS containing 1% BSA and 0.05% Tween®20. Anti-mouse IgG conjugated NPs or anti-mouse IgG conjugated AlexaFluor®647 were added to cells and NPs were added at 1µg per test and 3µl of AlexaFluor®647. The cells were left to incubate for another hour before being washed twice in PBS and finally resuspended in PBS before flow cytometry analysis.

7.2.5 Flow cytometry

Cells were analysed using a Millipore Guava EasyCyte8HT instrument and InCyte^{TM} software with red laser and red2 filter. Gain settings were optimised for MCF-7 and HeLa cell lines and LNCaP and PNT1A cell lines separately and were kept constant throughout testing. A red2 gain value of 2.08 was used for MCF-7 and HeLa and a gain of 2.0 was used for LNCaP and PNT1A. Forward scatter and side scatter were kept to 1.0 and a threshold cut off value of below 100. 20,000 events were counted per test.

7.3 Results and discussion

7.3.1 Secondary antibody functionality

Before carrying out secondary antibody cell staining work with goat anti-mouse IgG NPs, their avidity to the mouse anti-EpCAM antibody was investigated. A direct binding

assay was carried out in triplicate, consisting of the anti-EpCAM antibody coated on a 96 well plate at increasing concentrations, from 10-10,000ng/mL, and the addition of goat anti-mouse IgG NPs at 50µL of NPs (1mg/mL concentration). The response of the NPs was measured on the microplate reader and the results are shown in Fig 7.1.
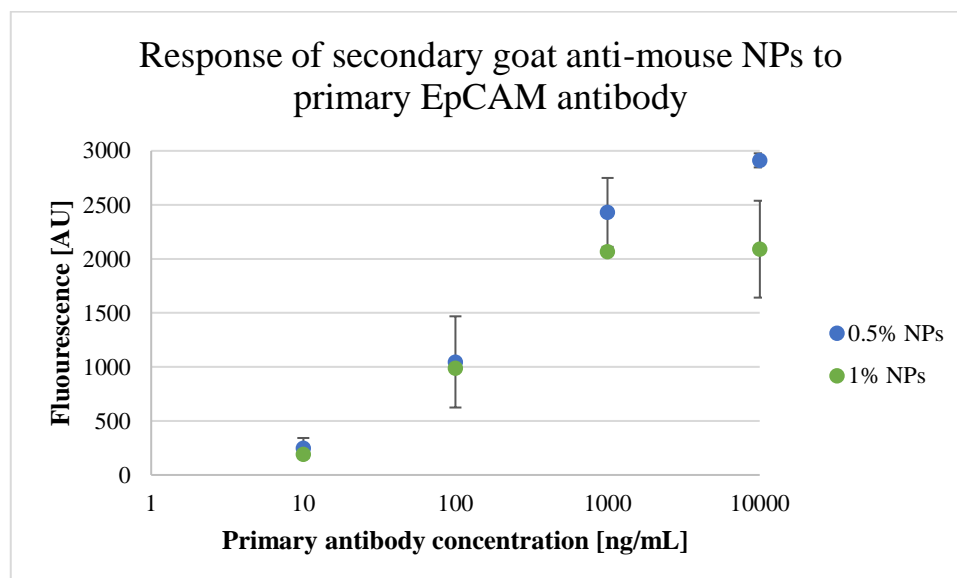

Fig 7.1: Secondary antibody immunoassay to evaluate the activity of the anti-mouse IgG on the surface of 0.168% and 279% NPs.

The data presented in Fig 7.1 shows the fluorescence from NPs in the 96 well plate, which were incubated with increasing concentrations of anti-EpCAM antibody for one hour. As the fluorescence increases comparably with the concentration of the antibody, it can be concluded that they are binding to the anti-EpCAM antibody. If a flat line was obtained, then the NPs would be bound non-specifically to the plate instead. This information allows the continuation of secondary antibody staining with confidence that the NPs will bind to the anti-EpCAM primary antibody.

7.3.2 Flow cytometry and image analysis with MCF-7 and HeLa cell lines

Secondary antibody labelling of cells was performed with NPs using EpCAM positive and negative cells, MCF-7 and HeLa cell lines.

Cells were prepared by placing them in PBS containing 1% BSA and 0.05% Tween®20 and counted on the haemocytometer. Following this, the cells were incubated with anti-EpCAM primary antibody, washed and then the NPs or AlexaFluor®647 secondary antibody added to the cells. The cells were then washed again and brought to the flow

cytometer or imaged under the microscope for analysis. The results from flow cytometry are presented below in Fig 7.2 and the cell imaging in Fig 7.3.
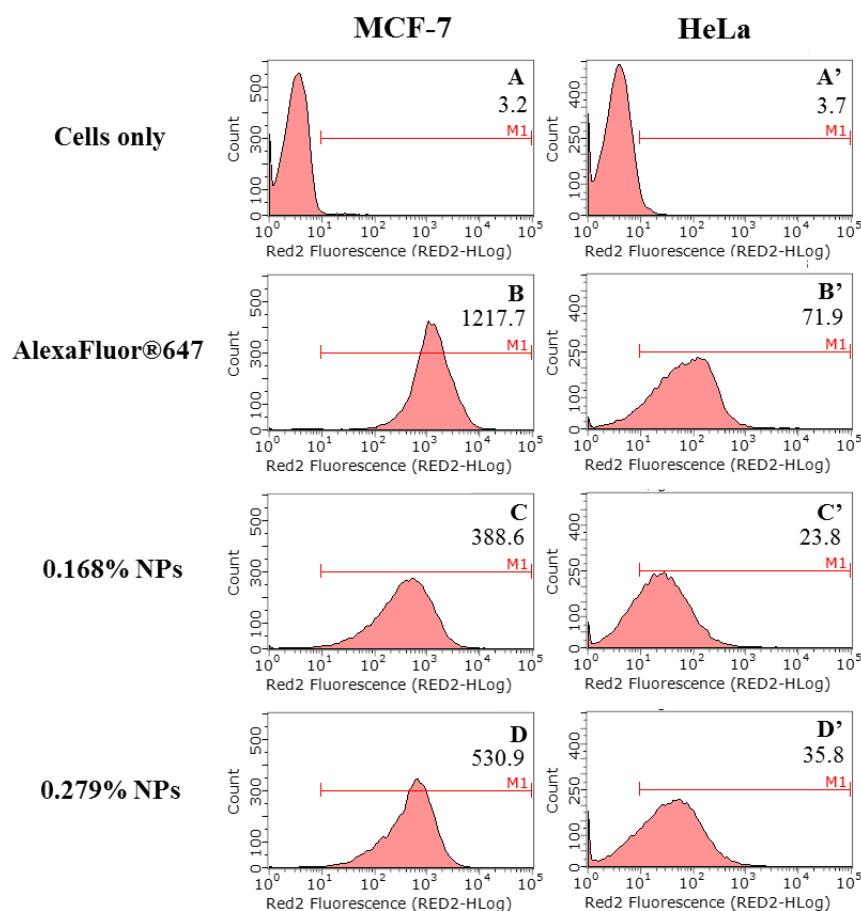
Fig 7.2: Flow cytometry results for secondary antibody staining MCF-7 cells and HeLa where the top row (A and A') are cells only and rows B-D and B'-D' correspond to cells incubated with anti-EpCAM red conjugates. The number in each graph is the median value for that experiment.

Looking at the MCF-7 cell line, from Fig 7.2, there is a high signal from all red-dye conjugates, indicating binding to the EpCAM primary antibody. Viewing the data for the HeLa cells shows that there is a relatively low signal from the two sets of NP secondary conjugates. However, the median value for AlexaFluor®647 appears to be unusually large, indicating non-specific binding (Fig 7.2 B') and can be visualised in Fig 7.3 (f'). This is surprising, as AlexaFluor®647 appears to perform the best for the MCF-7 cells, giving a median value that is three times the value for 0.168% NPs, or twice the value of the 0.279%, but the non-specific binding is higher than that of the NPs. Typically, the commercially available standard has almost no incorrect staining when compared with NPs (from chapter 5). Initially, non-specific binding from AlexaFluor®647 was thought to be caused by oversaturation of the cells with the

fluorophore. Control tests were carried out with flow cytometry in tandem to the tests shown in Fig 7.2 and the results are shown in Fig 7.4.
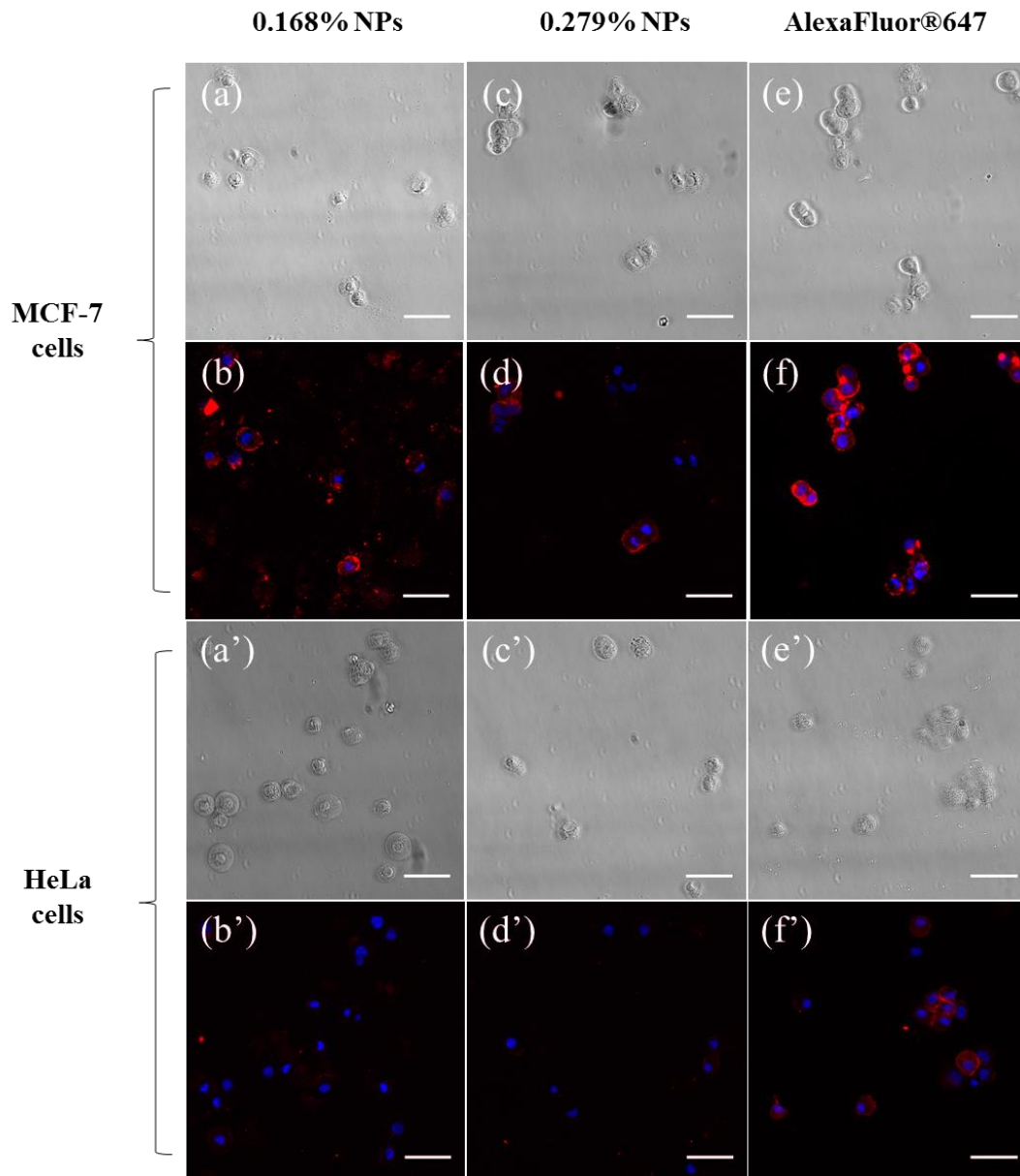
Fig 7.3: Bright field and corresponding fluorescence images of MCF-7 and HeLa cell lines incubated with goat anti-mouse IgG red dye conjugates. The nucleus of the cells (blue) is stained with Hoechst 33342. The scale bar represents 50µm

MCF-7 and HeLa cell control tests were measured by incubating cells with secondary antibody conjugates only, without primary antibody, to determine whether the fluorophores were non-specifically binding to the cells. Protocols were followed as

stated in section 7.2.4, without the addition of the primary antibody. The results are shown in Fig 7.4.
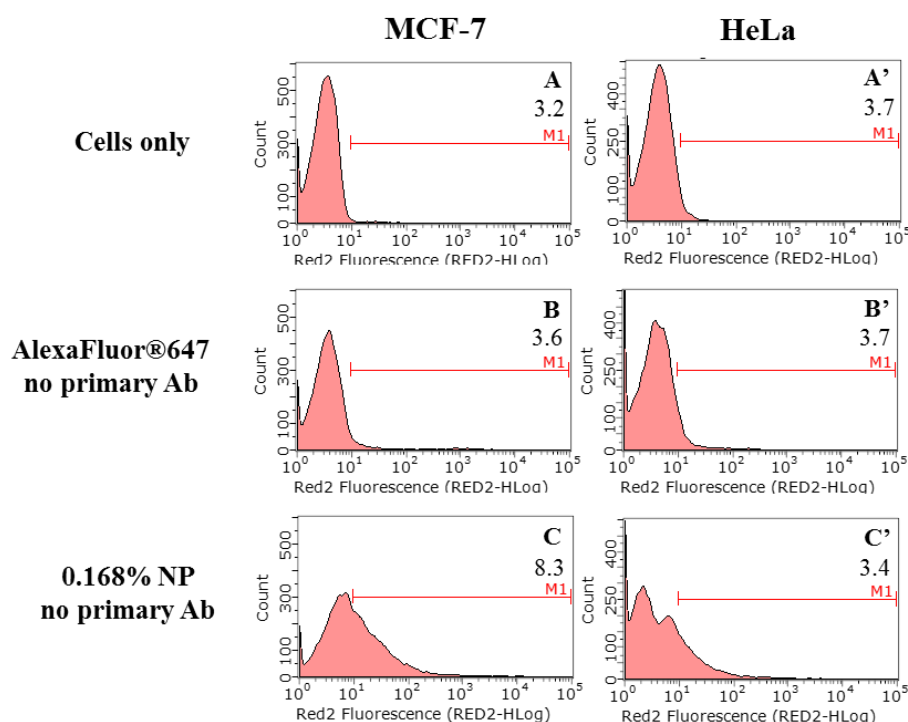
Fig 7.4: Flow cytometry data of cells incubated with AlexaFluor[®]647 or 0.168% NPs without prior incubation with primary antibody. The value is the median fluorescence value of the cells.

It is clear from the data presented in Fig 7.4 that the primary antibody plays a role in the large non-specific signal from the HeLa cells. The median fluorescence values of the AlexaFluor[®]647 are the same as for cells only, indicating that the fluorophore does not stain the cells non-specifically but that the primary antibody is causing the adherence of the dye labelled secondary antibody to the cells. Searching the literature has not led to any satisfactory explanation as to why this might be the case, as the mechanism of how the non-specific binding of the primary antibody can occur is unclear. One suggestion by Jackson Immuno Research Laboratories is to block the cells with goat serum rather than BSA as there may be some cross reactivity between the goat-anti-mouse and bovine IgG proteins that may have contaminated the BSA [4]. As there were no interactions, observed from the flow cytometry data, between secondary antibody and cells that were in solution containing BSA, this would seem to be an unlikely reason for the effect.

Image analysis was carried out on images of the cells in Fig 7.3 and on control NP tests and a summary of the results can be viewed in Fig 7.5. It would appear from the image

analysis that the NPs and AlexaFluor®647 are specific to EpCAM positive cells, as the signal in all cases is higher for MCF-7 cells than HeLa cells, even when the signal from HeLa cells was high. Statistical significance testing, in the form of the student t-test, was performed on all sets of data and it was found that, for all anti-EpCAM red conjugates, the mean values of MCF-7 compared to HeLa were statistically significantly different to each other ($P<0.05$), except for the case of the 0.168% NP control, for which no primary antibody was incubated with the cells, in which case the means were not significantly different to each other ($P>0.05$). This result is positive, as the control group should have similar means which implies that the level of non-specific binding for NPs is similar for both cell lines and does not interfere with specific targeting of the cells.
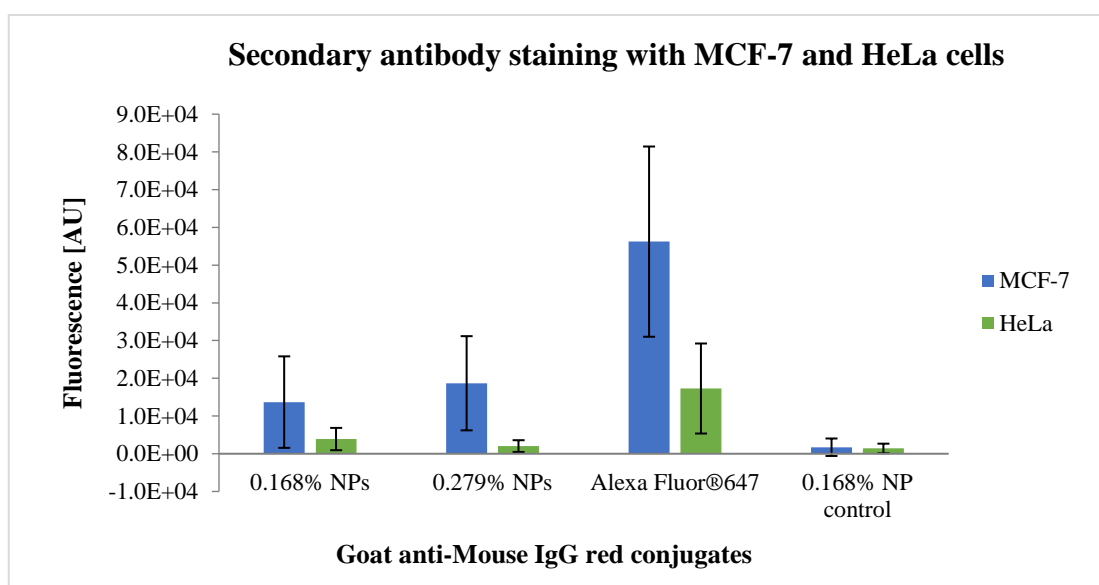
Fig 7.5: Image analysis of MCF-7 and HeLa cells incubated with secondary goat anti-mouse IgG NPs or AlexaFluor®647. The 0.168% NP control set have not been incubated with primary antibody previously.

To conclude, it appears that the NPs are specific to the primary antibody but for reasons currently unknown, the AlexaFluor®647 has a high binding efficiency to the control cell line, HeLa. Despite this, the difference between EpCAM positive and negative cell lines is more than enough to distinguish the different populations in flow cytometry and image analysis methods conclude that the differences in mean between cell lines is statistically significant. Therefore, it can be said that NPs can be used in a secondary antibody EpCAM detection system for MCF-7 and HeLa cell lines.

7.3.3 Flow cytometry and image analysis with LNCaP and PNT1A cell lines

Secondary antibody protocols were carried out on prostate cancer cells to investigate whether comparable results can be obtained for another EpCAM positive cell line, LNCaP. The PNT1A cell line was used as the control cell line. Cells were incubated with secondary goat anti-mouse IgG NPs or AlexaFluor®647 after they had been initially incubated with anti-EpCAM primary antibody. The results of these experiments from flow cytometry can be viewed in Fig 7.6.
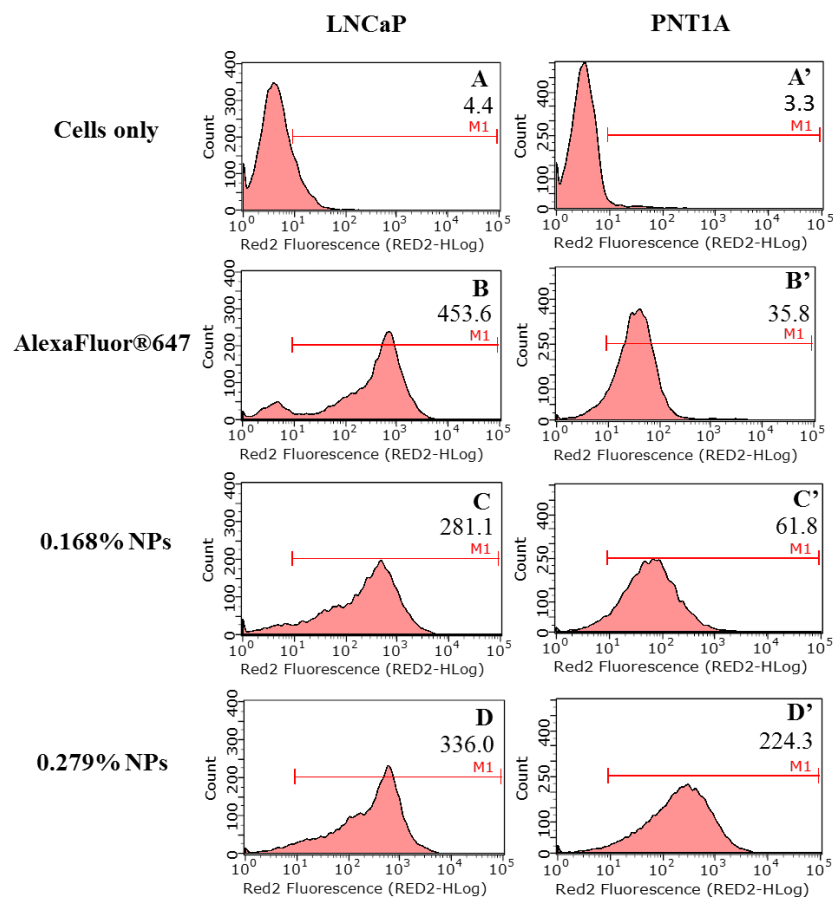
Fig 7.6: Flow cytometry results for secondary staining with LNCaP and PNT1A cells where the top row (A and A') are cells only and rows B-D and B'-D' correspond to cells incubated with anti-EpCAM red conjugates.

Addressing the data for LNCaP cells firstly, there appears to be three cell populations within the graph of the LNCaPs Fig 7.6 (B-D), most notably in Fig 7.6 B, in which cells were incubated with AlexaFluor®647. The majority of the cells in the largest peak appear to have a median fluorescence value of approximately 800, the second shoulder to the left of the main peak has a value in the region of 100 and the third is a small number of cells under the value of 10. The last peak most likely represents cells in the population that do not express EpCAM and the shoulder peak represents cells that have lower

expression than most of the cells. It is interesting to note that these three populations can be seen in the cells which have been incubated with 0.168% nanoparticles. However, the distinction when cells are incubated with 0.279% NPs is not quite so clear and the small population of non-EpCAM expressing cells is almost non-existent. The median value for all three fluorophores is similar and appears to be specific to the primary EpCAM antibody.

Interpreting the data for the PNT1A cells, there appears to be some amount of non-specific binding in the cases of all fluorophores. Interestingly, the signal for AlexaFluor®647 is much lower than that from HeLa cells that was observed in the previous section 7.3.2 and the 0.168% NPs also have a similar median fluorescence value. However, the 0.279% NPs have a much higher non-specific signal to that found with the direct binding anti-EpCAM conjugated NP system of section 5.3.4. It possible that the problem lies with the nanoparticles themselves, but they appear to perform well with the HeLa cell line, which would suggest that it is to do with the cell lines. It is possible that the PNT1A cells may have a different surface charge than the other cells that were used and could attract the NPs if they have enough charge. Cells have been known to vary greatly in zeta potential, even just changing temperature or enzyme treatment [5,6]. As the nanoparticles, 0.168% and 0.279%, also have different zeta potentials (-26mV and -9mV respectively) this could play a role in the larger non-specific binding of 0.279% NPs with PNT1A cells.

Overall, the AlexaFluor®647 and 0.168% NPs appear to be a successful working secondary antibody system. The NPs do not achieve as bright a signal from LNCaP cells as the AlexaFluor®647 in this case, combined with the higher non-specific binding. However, they do have a large enough median population difference. In Fig 7.7 are the corresponding images taken for the flow cytometry data. Image analysis was also carried out for these cells and is summarised in Fig 7.8.
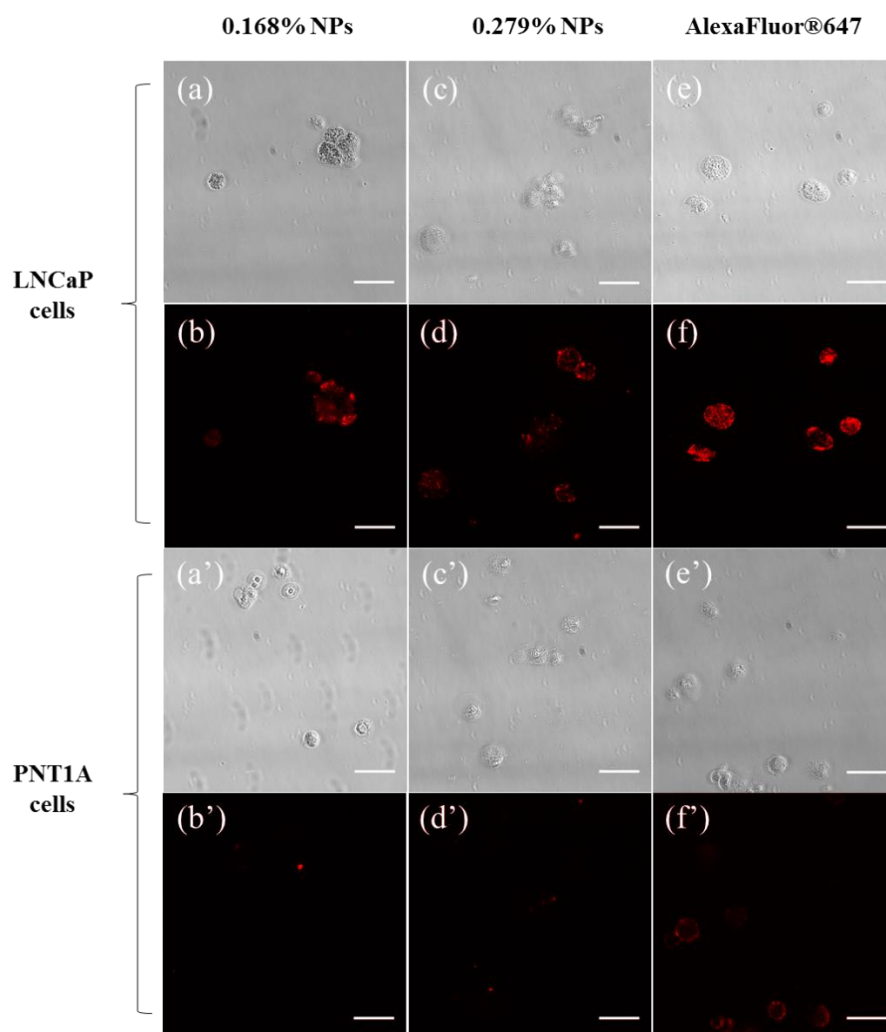
Fig 7.7: Bright field and corresponding fluorescence images of LNCaP and PNT1A cell lines incubated with secondary antibody red dye anti-EpCAM conjugates. The scale bar represents 50µm.

The data from image analysis agrees with data from flow cytometry. In Fig 7.7 (f') for PNT1A cells with AlexaFlour®647, the image appears brighter than the signal from cells with either set of NPs, similar to those images obtained with HeLa cells in section 7.3.2. Data analysis revealed that the means of LNCaP and PNT1A cells for each set of red dye conjugate were significantly different ($P<0.01$) except for the control NP group, to which no primary antibody had been added, for which the mean difference was not significant. Also, similarly to HeLa non-specific binding, the PNT1A for 0.168% NPs with and without primary antibody incubation was not statistically significantly different, again implying that the level of non-specific binding does not hinder the staining methods in the secondary antibody staining system, concluding that the 0.168% NPs could be used to stain EpCAM antibody in an LNCaP and PNT1A cell system.
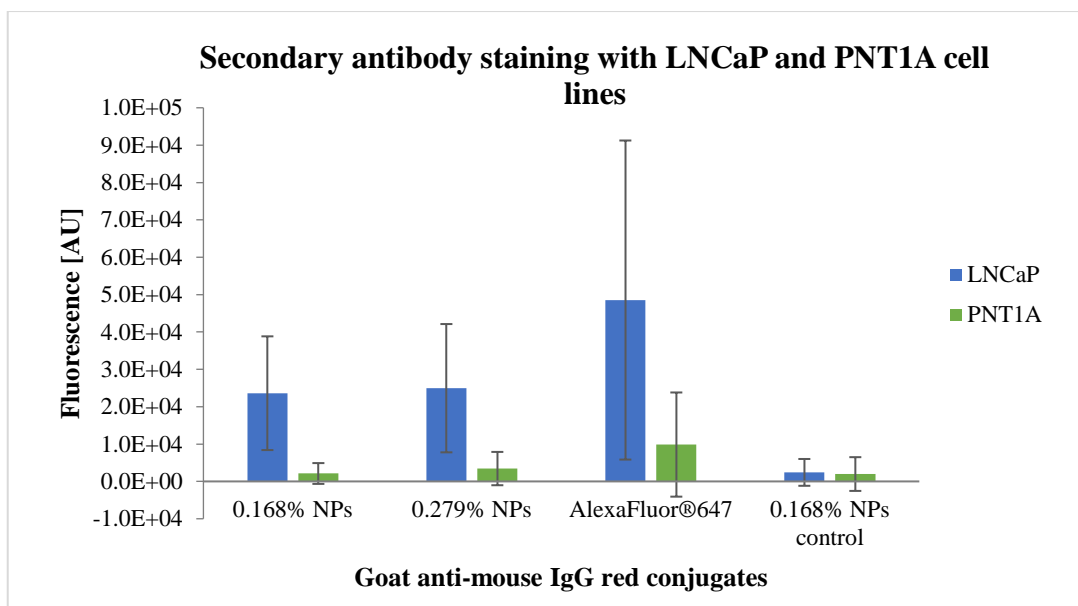
Fig 7.8: Image analysis data of LNCaP or PNT1A cells incubated with goat anti-mouse IgG NPs or AlexaFluor®647. The 0.168% NPs control sample have not been incubated with primary antibody before addition of NPs.

7.4 Conclusions

Secondary antibody NPs were successfully functionalised with goat anti-mouse IgG. The antibody was specific to mouse anti-EpCAM antibody as was tested via a direct binding assay. Flow cytometry tests with MCF-7 and HeLa cells have shown that both sets of NPs were specific to the anti-EpCAM antibody and that the 0.168% NPs were specific for the LNCaP and PNT1A cells. However, problems with non-specific binding of the AlexaFluor®647 have hindered a direct comparison of their performance to the NPs which is most likely due to some interactions between the primary and secondary antibody. Further work is required to determine the exact cause and also to investigated if the zeta potential of the cells interferes with the 0.279% NPs binding to PNT1A cells. The overall conclusion of the secondary antibody approach is that, for reasons stated above, there are no sensitivity advantage using NPs or indeed AlexaFluor®647 secondary staining over the primary antibody approach presented in chapter 5.

7.5 References

[1] M.-. Chen, Z.-. Chen, L.-. Wu, H.-. Tang, D.-. Pang, Goat anti-rabbit IgG conjugated fluorescent dye-doped silica nanoparticles for human breast carcinoma cell recognition, Analyst. 138 (2013) 7411-7416.

[2] M.-. Estévez, M.B. O'Donoghue, X. Chen, W. Tan, Highly fluorescent dye-doped silica nanoparticles increase flow cytometry sensitivity for cancer cell monitoring, Nano. Res. 2 (2009) 448-461.

[3] R. Nooney, C. O'Connell, S. Roy, K. Boland, G. Keegan, S. Kelleher, S. Daniels, C. McDonagh, Synthesis and characterisation of far-red fluorescent cyanine dye doped silica nanoparticles using a modified microemulsion method for application in bioassays, Sens Actuators, B Chem. 221 (2015) 420-479.

[4] I. Jackson, Common Causes of Background from Secondary Antibodies, 2017 (2015).

[5] O.V. Bondar, D.V. Saifullina, I.I. Shakhmaeva, I.I. Mavlyutova, T.I. Abdullin, Monitoring of the Zeta Potential of Human Cells upon Reduction in Their Viability and Interaction with Polymers, Acta Naturae. 4 (2012) 78-81.

[6] H.P. Fernandes, C.L. Cesar, M.L. Barjas-Castro, Electrical properties of the red blood cell membrane and immunohematological investigation, Rev. Bras. Hematol. Hemoterapia. 33 (2011) 297-301.

Chapter 8: Metal enhanced **fluorescence**

8.1 Introduction

In this chapter, the use of surface plasmon-based fluorescence enhancement to improve cell imaging is investigated. This follows on from earlier chapters in which cell imaging using high brightness silica NPs, or single red dye fluorescent labels, was reported. The motivation is to capitalise on ongoing work in the research group on the use of gold plasmonic diffraction grating substrates for enhanced fluorescence-based bioassays and to explore the use of these grating substrates for enhanced imaging of cells using an epifluorescence microscope [1]. The preparation of the grating substrates for cell adhesion, the imaging data and an interpretation of the results are presented herein.

As discussed briefly in Chapter 2, surface plasmon resonance (SPR) is a phenomenon which describes the coupling of incident light into a metal-dielectric interface producing surface plasmon polaritons (SPPs), also known as surface plasmon waves, which include and electric and magnetic component [2,3]. Light will only couple into the SPPs when it is polarised parallel to the plane of incidence (p-polarised) and the momentum of the vector in the X direction (K_{Lx}) matches the momentum of the polaritons (K_{spp}), (see Fig 8.1) [4].
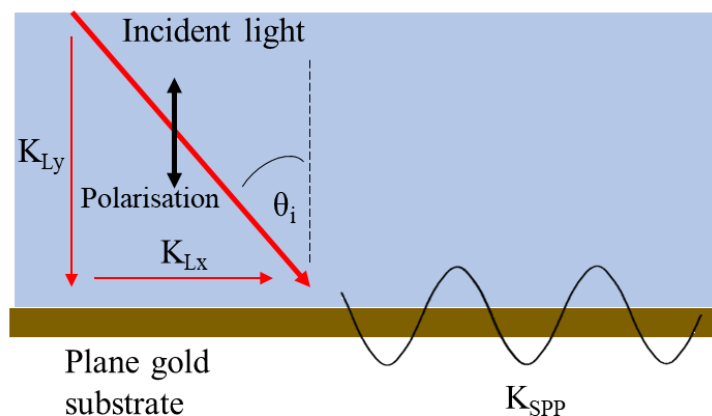

Fig 8.1: Production of surface plasmon resonance from light p-polarised parallel to incident light that matches the required angle and momentum conditions within a prism

The coupling condition for SPR strongly depends on the complex dielectric function of both the metal and dielectric medium and is given below in equation 8.1 and 8.2:

$$K_{Lx} = K_{SPP} \qquad \text{(Eq. 8.1)}$$

$$K_{spp} = \frac{2\pi}{\lambda} \sin\theta_i = \frac{2\pi}{\lambda} \sqrt{\frac{\varepsilon_M \varepsilon_D}{\varepsilon_M + \varepsilon_D}} \qquad \text{(Eq. 8.2)}$$

where λ is the wavelength of incident light, θ_i is the angle between the incident light and the normal of the substrate and ε_M and ε_D are dielectric functions of the dielectric and metal, respectively [3].

There are different optical set ups that can be used in order to achieve coupling. Prism-coupled SPR, can use either the Kretschmann or Otto geometry, which both use a prism to modify the dielectric function so that incident light momentum can be matched to that of the plasmon [5,6]. The Kretschmann configuration requires metal to be deposited onto the side of the prism where light is incident on the metal from inside the prism. The opposite side of the metal is the sensing side [5]. For the Otto configuration, light is also incident through the prism but there is a gap between the prism and the metal [6]. Grating-coupled SPR can be used as a method to couple incident light into the metal, whereby the metal is periodically structured. In this configuration, the periodic structure can be used to modify the in plane component of the light vector through the addition or subtraction of the grating vector. This optical setup has many advantages, but mainly it has a higher coupling efficiency and a simple optical setup [7,8].

In grating coupled SPR, the coupling angle can be controlled by the period and pitch of the grating. The momentum needed to match that of the SPPs is now defined as:

$$K_{Lx} \pm K_g = K_{SPP} \qquad \text{(Eq. 8.3)}$$

where K_g is the momentum introduced by the grating. For a periodic metal layer with a grating pitch of Λ, the matching conditions are described by the following equation [1]:

$$K_{SPP} = \frac{2\pi}{\lambda} \sin\theta_i \pm n \frac{2\pi}{\Lambda} = \frac{2\pi}{\lambda} \sqrt{\frac{\varepsilon_M \varepsilon_D}{\varepsilon_M + \varepsilon_D}} \qquad \text{(Eq. 8.4)}$$

Usually, the pitch of the grating is selected so that θ_i is small enough that this coupling angle is covered by the angle at which incident light will fall onto a grating through a microscope lens.

Some groups have previously used silver coated plasmonic gratings for the amplification of fluorescence from labelled cells [7,9]. Typically, silver provides a better SPR signal as both the real and imaginary parts of the dielectric function are better suited to plasmon generation compared to gold, so enhancements similar to those found with silver would not be expected [10]. Cui et al. used silver coated gratings for imaging cells on an upright microscope with 40x lens [7]. Using this set up, an 8-fold increase in the signal from cells was achieved when compared to a cell on a silver substrate and 24-fold enhancement between the gratings and cells on a glass substrate. This increase was measured from the grey value from a line scan of a stained cell. Tawa et al. also used silver coated gratings for the enhancement of cell imaging. Human embryonic kidney cells (HEK) were dyed with AlexaFluor®647 membrane while being cultured on a grating embedded dish and was compared with a normal glass bottom dish. Using an upright fluorescent microscope, they observed a 14-17-fold increase in signal as compared to the glass bottom dishes. However, this report did not include a comparison to plane silver surfaces [9]. Enhanced fluorescence of fluorescent molecules using gold gratings has been carried out by Byrne et al. and simulated the fluorescence enhancement to penetrate anywhere from 20nm-200nm above the grating surface at certain points [1]. Previous studies using gold gratings for cell imaging have been carried out with LED light sources at 875nm and were used to capture and detect human Jurkat T lymphocytes in an enzyme linked immunosorbent assay format as a present or absent test [11,12]. This was not compared to non-grating surfaces. The results that were obtained for cell fluorescence enhancement using gold grating substrates are reported in this chapter.

8.2 Materials and methods

8.2.1 Materials

Anti-EpCAM AlexaFluor®647 was obtained from BioLegend (CA, USA). DY647-P1 was obtained from Dyomics (Jena, Germany). Gold coated plain plastic and grating plastic substrates were chosen to test for cell imaging due to an ongoing project in the group. They were synthesised by Dr. Daragh Byrne from the School of Physical Sciences Dublin City University. 0.279 (w/w%) Cyanine5 doped silica NPs were synthesised in house as described in chapter 4. All other materials were obtained from Sigma Aldrich.

8.2.2 Plasmonic gratings

Plasmonic gratings were produced using an interference laser lithographic beam previously reported [1]. In brief, gratings were fabricated using a KR1801C TEM00 HeCd laser (Kimmon Koha, Japan) in SU8 resist, followed by polydimethylsiloxane (PDMS) replication. The master grating was produced via interference lithography using a Lloyd mirror configuration. In this configuration, a divergent beam is used to illuminate the photoresist coated substrate and mirror, which are at right angles to each other. The light is reflected from the mirror onto the sample, creating an interference pattern at the substrate surface as shown in Fig 8.2 below. The grating period can be adjusted by altering the angle between the two interfering beams. The pitch of the grating Λ is governed by the equation:

$$\Lambda = \frac{\lambda}{2\sin\theta} \qquad \text{(Eq. 8.5)}$$

where λ is the wavelength of the beam and θ is the angle between the two beams.
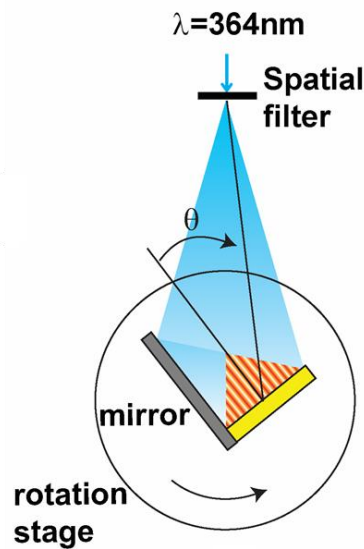

Fig 8.2: Laser interference set up for creating master grating in SU8 on silicon using Lloyd mirror adapted from [13].

The master grating surface on the silicon wafer (see Fig 8.3 below for an atomic-force microscopy (AFM) image of a typical resultant grating) was then used as a template for

PDMS replication. These PDMS moulds were used to create epoxy resin casts which were subsequently coated in gold using a vacuum evaporator.
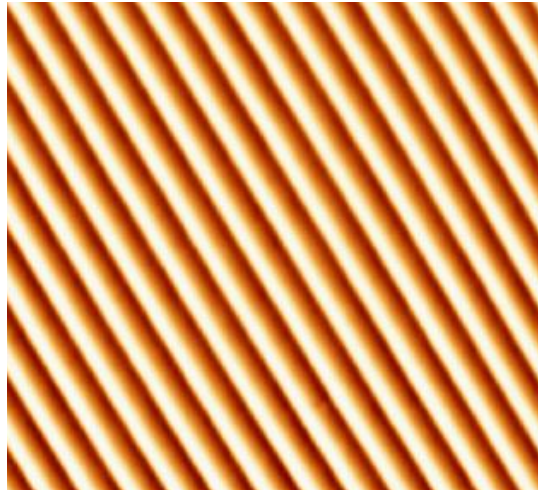
Fig 8.3: Typical grating surface of Si wafer after interference lithography in SU-8 photoresist adapted from [1].

Dye coated substrates were prepared by spin coating with a dye doped polyvinyl alcohol (PVA) mixture containing 1% w/w PVA and 0.008% w/w DY647-P1.

8.2.3 Cell preparation

The MCF-7 cell line was grown in a $75cm^2$ flask in DMEM containing 10% heat uninactivated FBS, 1% L-glutamine and 1% penicillin-streptomycin. The cells were cleaved from the bottom of the flask using trypsin. Cells were centrifuged (300xg, 5 minutes) and resuspended in PBS containing 1% BSA and 0.05% Tween®20. Following this, cells were counted on the haemocytometer and the final solution was adjusted so that there were 125,000 cells for staining with either anti-EpCAM AlexaFluor®647 or 0.168% anti-EpCAM NPs. Stains were added either 3.0 µL of AlexaFluor or 10.0 µL of NPs (1mg/mL concentration) to cells and incubated for 40 mins. After this, cells were centrifuged and washed three times in PBS and finally resuspended in ~30 µL of PBS. Then 7 µL of solution was added to either a glass, gold or grating substrate after which a cover slip was applied and sealed. The cells were left to attach to the substrates for 30 mins before imaging.

8.2.4 Imaging of dye coated or dye labelled cells on substrates

Imaging was initially performed on an Olympus IX71 inverted microscope that was described in section 5.2.4 and referred to as the manual microscope. The second imaging system used was an Olympus IX81 inverted microscope with IX2-UCB motorised XYZ stage control and motorised lenses (Olympus, Tokyo, Japan). A Hamamatsu ORCA-ER CCD camera (Hamamatsu Photonics K. K., Hamamatsu, Japan), MT20 illumination source (Olympus) and Cell R imaging software (Olympus) were used with the inverted microscope. It is referred to as the Hamamatsu microscope. A Cy5 filter cube set was used when imaging all cells in this chapter.

All gains were set to zero and an integration time was chosen so as to achieve near saturation of the CCD camera when imaging the highest concentration sample, or that which should be the brightest i.e. the samples on gratings. Once this integration time was determined, it was applied to all other samples and no parameters were changed. For the manual microscope, this was a 5s integration time with a 20x lens and for the Hamamatsu system this was 50ms using a 20x lens.

Images acquired were analysed using Image J software (NIH, USA), whereby the fluorescence from a region of interest, usually the cell, was measured and compared to background fluorescence from a region where no cells were situated.

8.3 Results and discussion

8.3.1 Adhesion of cells to gold coated substrates.

As the microscope system was an inverted system setup, an investigation was carried out as to the adherence of cells to the surface. This is particularly important as the modified electric field from the generation of surface plasmons decays exponentially with distance from the metal surface and is typically only observed within the first 200 nm range, and only strongly within 50 nm, from the surface of the grating [1]. If the cells do not attach correctly, the fluorophores on the surface of the cell are unlikely to display significant enhancement. A test was devised, whereby MCF-7 cells that were stained with anti-EpCAM AlexaFluor®647 were placed on plane gold and gold grating surfaces either unmodified or after modification with a thiolated RGD peptide. Thiolated RGD has been used to bind cells to the surface of gold previously [14,15].

Images were taken, on the manual microscope, of cells after 30 mins of incubation on the surface of the substrates in both cases and the average fluorescence of the cells was established. Care was taken when imaging the cells to focus on the cell surface that was closest to the gold substrate. The fluorescence results were compared between the thiolated and unmodified gold substrate and also compared between samples that were prepared on a glass slide.
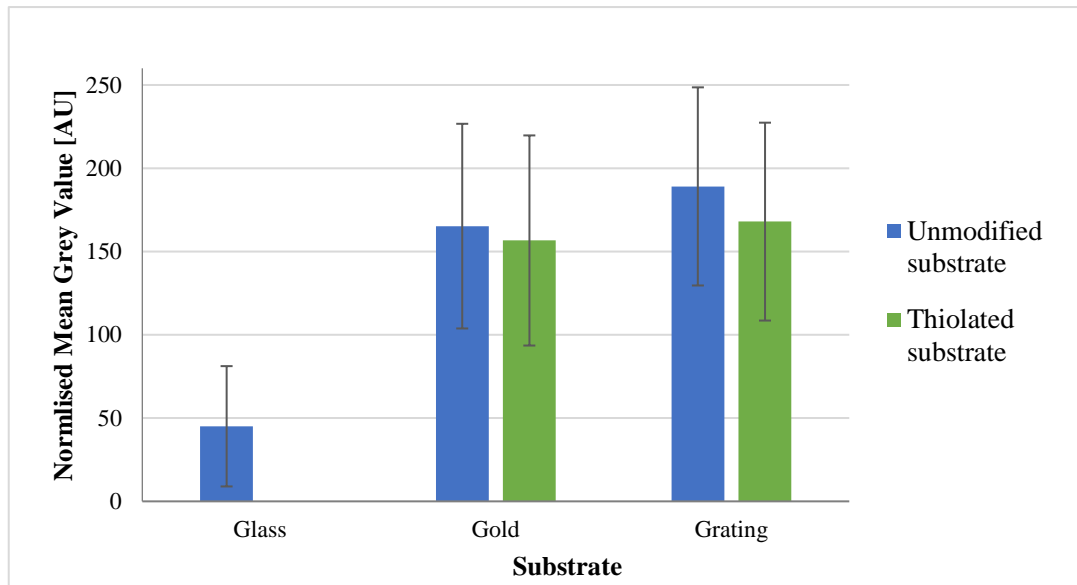

Fig 8.4: MCF-7 cells stained with AlexaFluor®647 attached to unmodified or thiolated plane gold (Gold) or gold grating (Grating) substrates

Fig. 8.4 summarises the results of this experiment where it was found that no statistically significant difference was present between the fluorescence intensity from samples that were placed on thiolated RGD or unmodified substrates from the student's t-test. This indicates that the cells can adhere to the gold surface without the use of RGD peptide. Samples that were placed on gold substrates, both plane and thiolated, were statistically significantly brighter than the cells imaged on glass with $P<0.05$ in all cases. The grating samples were then compared to samples on plane gold and it was discovered that they were not significantly more fluorescent with $P>0.05$ for the two cases. This would indicate that K_{Lx}, is not matching K_{SPP} and more work was carried out to investigate this further. See Fig 8.5 below for sample images of cells take on each of the substrates.
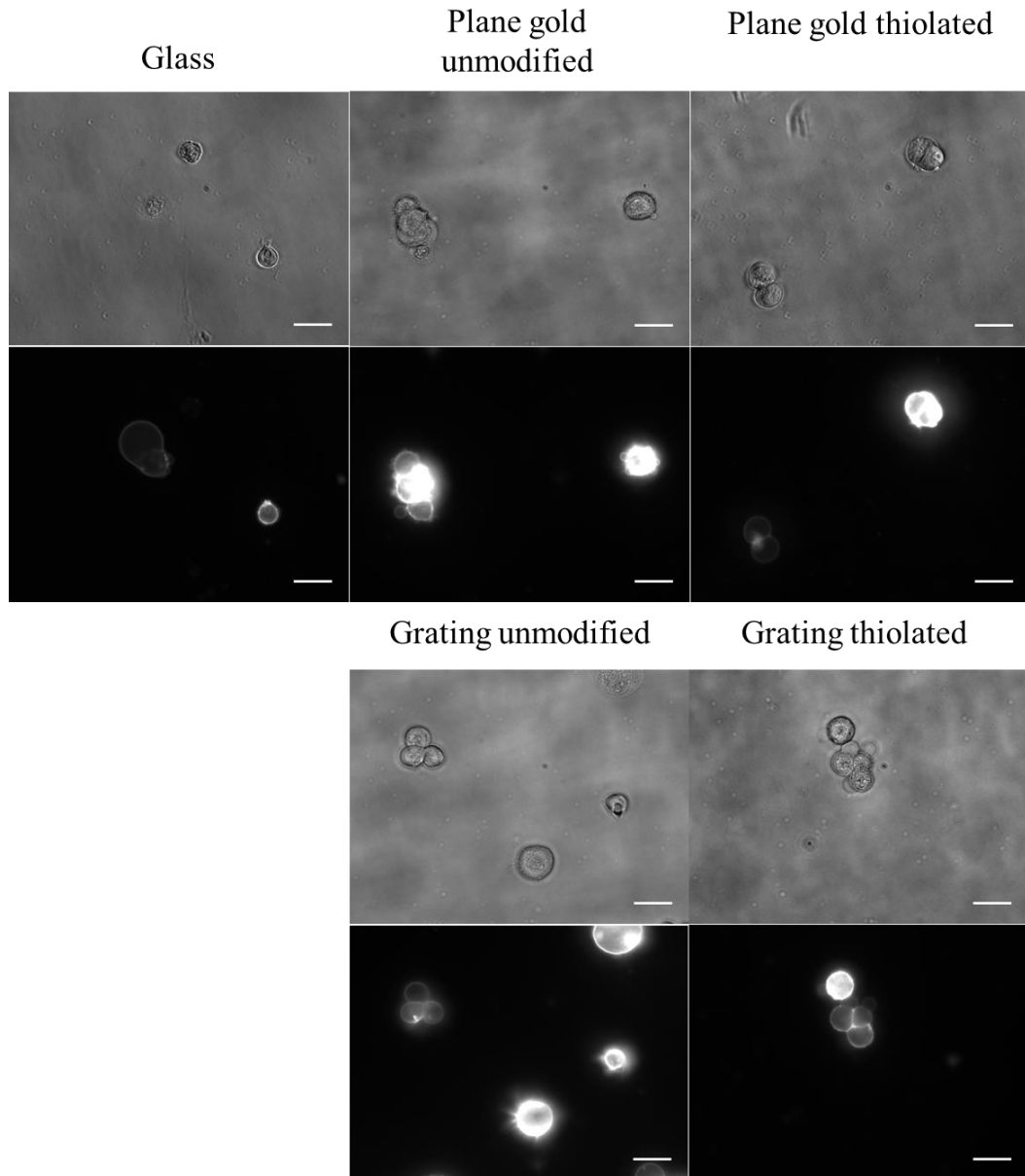
Fig 8.5: Bright field and Cyanine5 filter cube imaging of MCF-7 cells stained with AlexaFluor®647 anti-EpCAM on glass, gold and grating surfaces unmodified or thiolated.

8.3.2 Investigation of coupling of light into the grating surface

As mentioned in the previous section, it is necessary to investigate whether the excitation source of the microscope can couple into the grating. The criteria needed to do this includes that the light is linearly polarised along the Bragg vector of the grating and also that the momentum of the incident light matches that of the SPPs. The fluorescence source in the manual microscope was an X-Cite series 120 excitation lamp which uses a mercury lamp to illuminate the filter cubes. This light source is unpolarised, and so a polariser was introduced in this system. The microscope has a slot at the back where the

light source is coupled to the microscope and in this slot was placed a linear polariser which was free to rotate 360° in the vertical plane. The polariser was rotated every 45° in order to attempt to observe enhanced fluorescence which would indicate the light was linearly polarised to the Bragg vector of the grating. In theory, there should be a maximum every 180°. MCF-7 cells were stained with anti-EpCAM AlexaFluor®647 and were allowed to adhere to either a grating or a plane gold substrate, which was used as a control since there should be no observable maxima with the gold substrate. An image was taken of the same cell every time the polariser was rotated 45°. The images were then analysed in image J and the average pixel grey value of the fluorescence emitted from the cell was obtained and displayed in Fig 8.6.
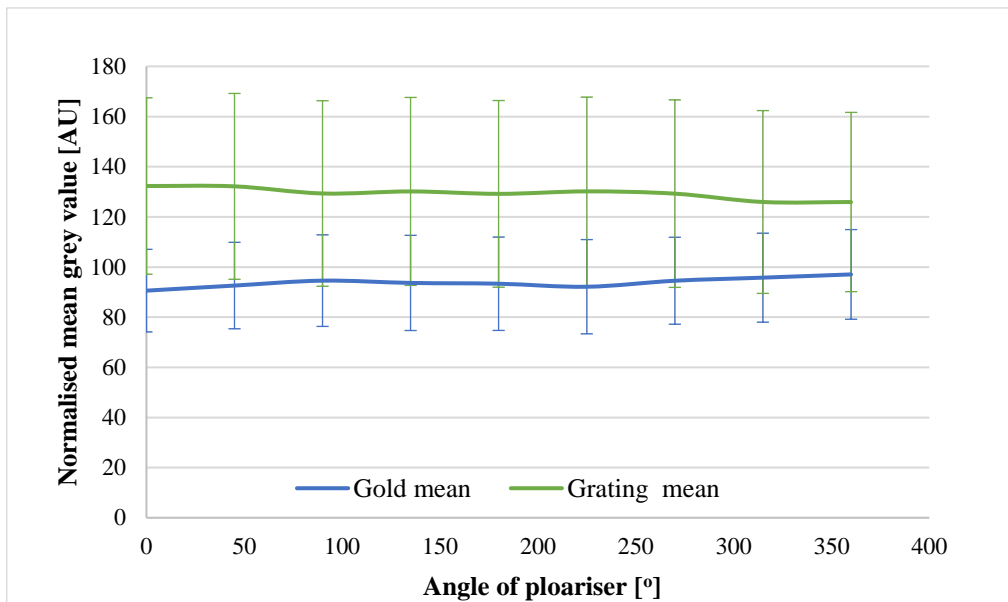
Fig 8.6: Mean grey value of stained MCF-7 cell through rotated polariser on a plane gold or gold grating substrate

It is clear from the data, that for both substrates, the fluorescence intensity was unaltered by the light polarisation angle. This implies that the polarisation is not being maintained within the microscope. As the light passes through the filter cube, it must transmit through three surfaces that possibly do not keep the polarisation introduced by the linear polariser. Because of this, a laser source microscope such as a laser scanning confocal microscope should be easier to achieve this. Also as the beam of light hits the substrate at a range of angles, only a finite distribution of these angles will satisfy the momentum conditions for a fixed period grating. It was reported previously that the coupling angle for a grating pitch of 581nm and wavelength of 630 nm is approximately 5-7° [1]. The range of angles at which a 20x lens illuminates a sample on the microscope can be

calculated using the numerical aperture equation (Eq. 8.6). Knowing the numerical aperture of the 20x lens (NA) of 0.4 and refractive index, η, of 1.52 for glass it can be substituted into the following equation:

$$NA = \eta sin\theta_i \qquad \text{(Eq. 8.6)}$$

to find that the lens allows for angles from 0° to 15.1^o and covers the coupling angle needed.

To ensure that the gratings were functioning correctly and to investigate the response of the microscope to various concentrations of dye, two experiments were devised. The first employed dye-doped PVA that was coated on the surface of plane gold and grating substrates instead of imaging cells. These dye-doped substrates were measured on an instrument built by Dr. Daragh Byrne which has the capability of changing the coupling angle to the substrate and uses a diode laser. The results are presented below in Fig 8.7.
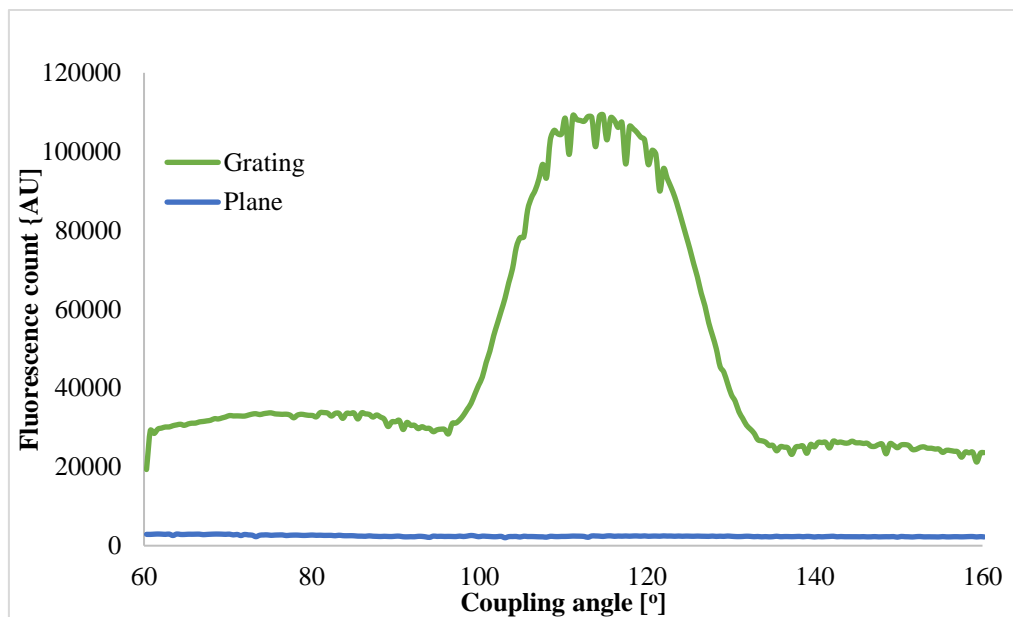
Fig 8.7: Fluorescence response of dye doped polyvinyl alcohol on the surface of plane gold or grating substrates on the system built by Dr. Daragh Byrne as the laser couples into the grating.

From the data in Fig 8.7, the base level from 65-95° of the two substrates refers to the dye concentration on each of the substrates. This base concentration was measured to be 10x more dye on the grating than that on the gold surface before angle coupled enhancement is observed (100-130°). At the peak of the enhancement, ~115°, an enhancement factor of approximately 4x is clearly visible in Fig 8.7. This indicates that,

under appropriate coupling conditions, the gratings do produce a fluorescence enhancement which should translate to the microscope.

Another microscope system, the Hamamatsu microscope, was employed that had better control over illumination, gain and camera settings to test the grating substrates and was tested for comparative purposes.

These substrates were then measured on the two microscope systems, the manual and Hamamatsu, and the results are shown below in Fig 8.8. Three spots on each of the substrates were measured on both systems to ensure comparative results and it was expected to see these enhancements on the microscopes similar to the system built by Dr. Byrne. As the previous results did not show an improvement when using a polariser, no polariser was used with the manual microscope this time around.
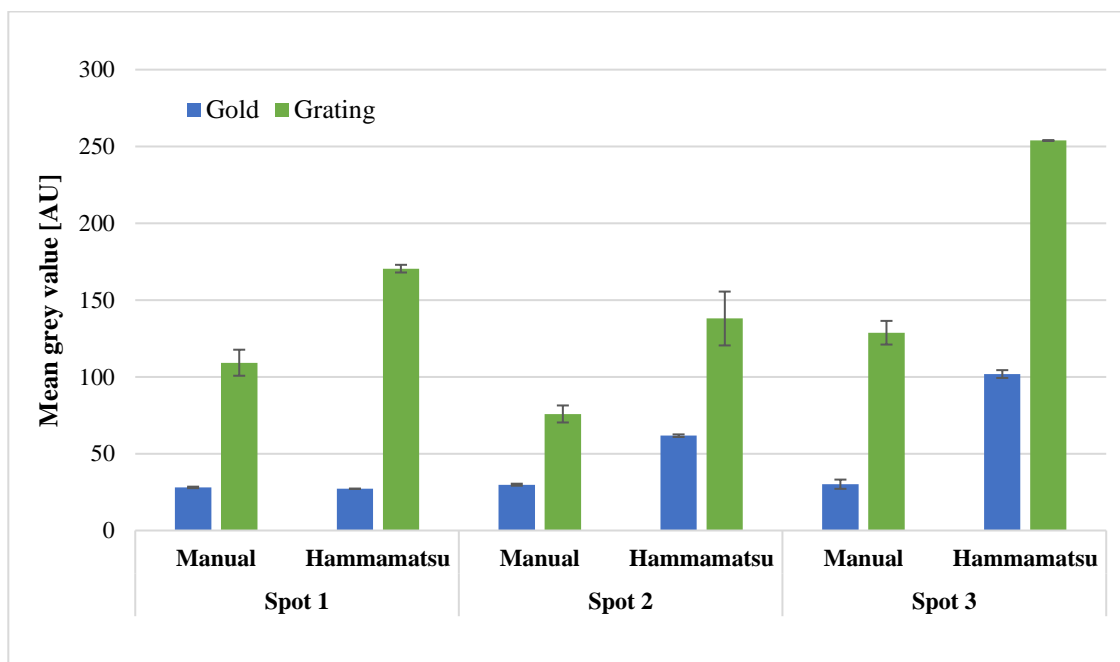
Fig 8.8: Results from measuring dye coated plane gold or grating substrates on a manual microscope (manual) compared with a Hamamatsu microscope at three different spots

Results from these tests showed that there was slight enhancement in signal from the gold and grating samples on the two microscope systems. However, this enhancement did not capture the difference in concentration of dye on the surface of the grating substrates that is accounted for when measuring on the laser angle coupling system. It was unclear if this was due to a difference between the response of the microscope camera compared to the camera used on Dr. Byrne's system.

Another test was run to check the responsivity of the CCD camera on the Hamamatsu microscope in relation to increasing concentrations of dye. A 96-well microplate was used to attach increasing concentrations of DY647-P1 anti-human IgG antibody to the surface of the well plate. Simultaneously, the same antibody concentrations were placed on wells that were coated in silver nanoparticles to enhance the emission of the dye. A colloid solution of silver nanoparticles has been shown to enhance fluorescence emission previously through localised surface plasmon resonance [16]. The results of these tests are summarised in Fig 8.9.
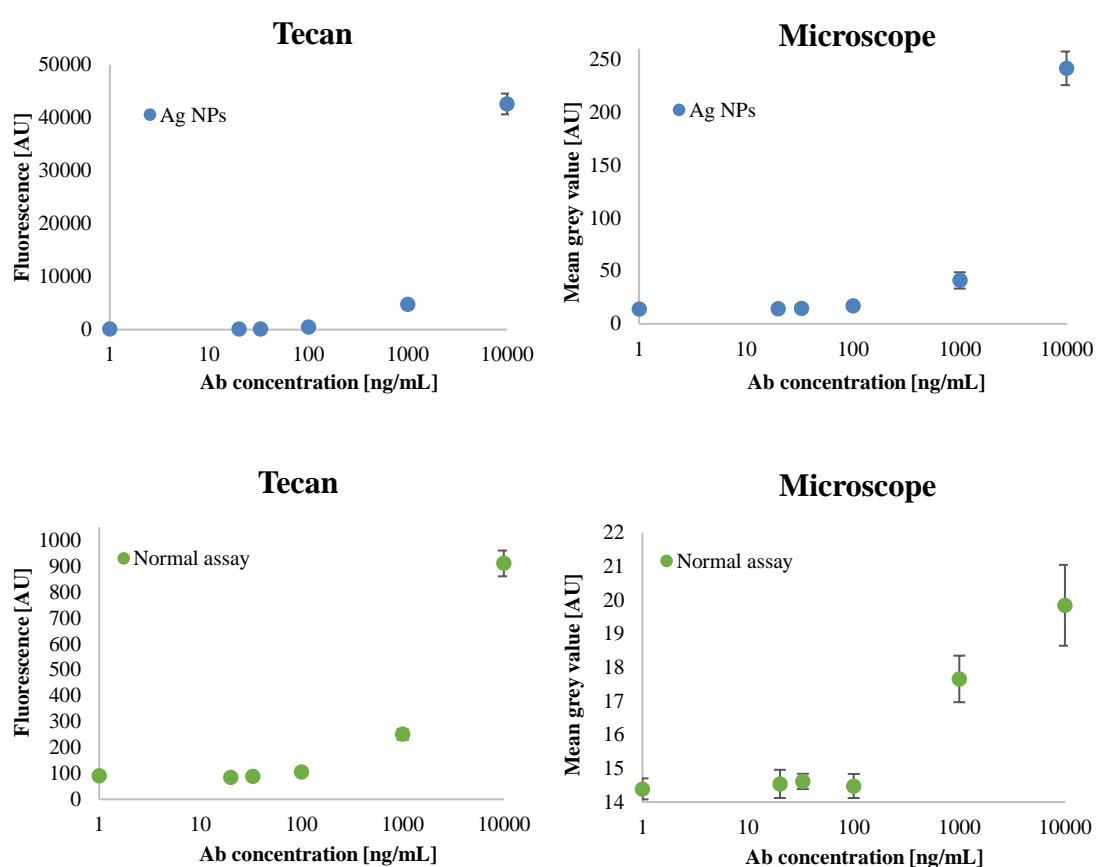
Fig 8.9: human IgG labelled with DY647 on a silver nanoparticle plate well surface (top) and on a normal plate well surface (bottom) on a microplate reader (left) compared with readings from the Hamamatsu microscope (right).

The microscope measures fluorescence on a scale from 0-255 whereas the Tecan can output values up to 50,000 units. As a consequence, the graphs were not plotted together and a general comparison of trend was observed instead. For the assay performed on the silver nanoparticle coated surface of the well plate; both the Tecan microplate reader as well as the microscope system displayed a similar trend in fluorescence emission. This

implies that the camera should be able to detect the enhancement that is associated with imaging on the gold gratings. However, looking at the normal assay that was performed on both systems, the response from the microscope is not as sensitive. It is possible that this was caused by optimising the exposure time of the camera on the Hamamatsu microscope for the brightest well i.e. the highest concentration of antibody on the silver nanoparticle well surfaces. If the secondary assay exposure time was reoptimized a more sensitive response may have been achieved. However, as the microplate reader data was measured on the same gain settings, a like for like experiment was carried out. The conclusion drawn is that if significant coupling was taking place, an enhanced emission should be observable and that the Hamamatsu microscope camera is sensitive enough to distinguish the enhanced signal.

8.3.3 Use of Cyanine5 nanoparticles with grating coupled SPR

Although a large enhancement was not visualised previously using the gratings and AlexaFluor®647, it was decided to test nanoparticles on the microscope system. Anti-EpCAM conjugated 0.168% NPs were incubated with cells and compared with the performance of an AlexaFluor®647 stain. Both were tested on glass, plane gold and gold grating substrates and images were taken of cells with a 20x lens and measured using image J. A summary of the results is displayed in Fig 8.10 and can be visualised in Fig 8.11.
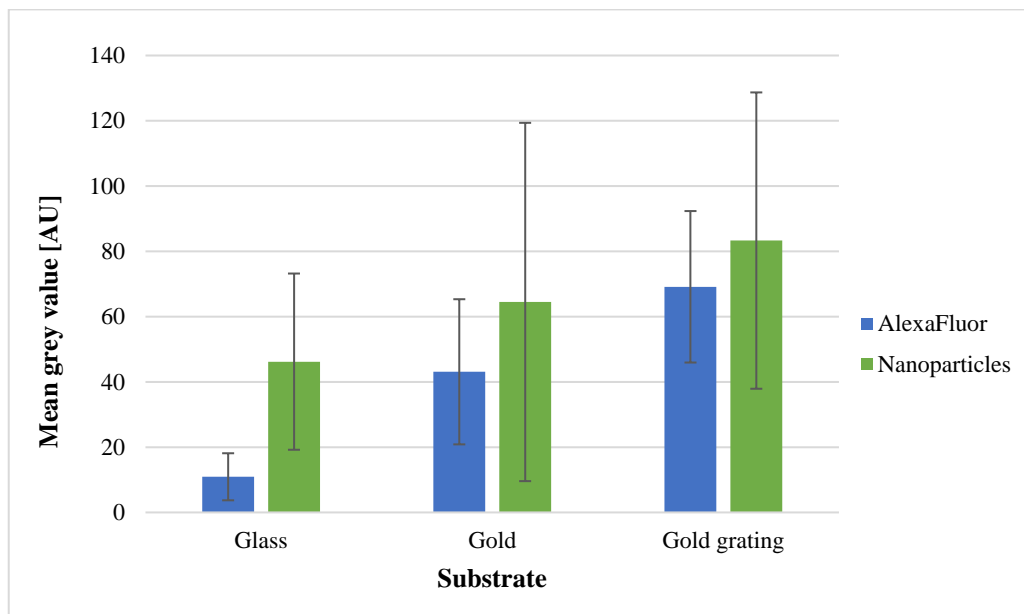

Fig 8.10: Data analysis of images obtained for MCF-7 cells labelled with anti-EpCAM AlexaFluor®647 or NPs that were placed on either glass, gold or grating substrates.

Cells on the grating substrate had an overall higher average than that of the cells on the gold and glass substrates. A 1.6x enhancement was obtained between grating and gold substrates using AlexaFluor®647 and 1.3x for NPs, which was an overall 6.3x and 1.8x increase from grating substrates compared to glass in both cases for AlexaFluor®647 and the NPs respectively. However, statistical significance testing in the form of a student's t-test was performed on the data set and it found that the nanoparticle stained cells on the grating, in comparison to the gold substrate, was not statistically significant (P>0.05) nor was it significant in comparison to glass. Interestingly, the cells stained with AlexaFluor®647 on grating substrates were statistically significant (P<0.05 in all cases) compared to gold substrates and similarly to the glass. It was found that the increase in fluorescence on the gold was also statistically significant compared to the glass substrates. Comparing AlexaFluor®647 to NPs on the same type of substrate, both plane gold and grating substrates were not significantly different but the comparison on glass was significant. This implies that the nanoparticles outperform the AlexaFluor®647 when used with glass substrate but that significant enhancement is not observed when using the NPs with plane gold or grating substrates which is observed when using AlexaFluor®647. There was a large overall variability in mean grey value, generally due to the variance in cell size being measured, but also another contributing factor was the EpCAM expression across the cell membrane.

Previous papers using silver coated gratings have observed an enhancement of fluorescence from cell staining, as mentioned in the introduction [7,9]. One paper in particular observed an 8-fold enhancement using the silver gratings compared to plane silver. However, some scepticism into this result is held as this increase is obtained from taking a line scan across a cell image of one particular cell on a silver grating and compared it to the line scan of one cell that was on a plane silver surface or glass substrate [7]. It is unclear from the report whether this was repeated for any more than one cell and so, does not infer that this was the result for all cells that were found on the substrates. Having said this, other groups have been successful in enhancing the fluorescence of cells grown on a silver grating but this was only compared to a glass substrate and did not measure the cells grown on a plane silver substrate to view pure metal enhanced fluorescence effects [9]. This is particularly important given that the use of a reflective substrate effectively doubles the intensity of light passing through the

fluorophore stained cell. The data in Fig 8.10 for AlexaFluor®647 is comparable to the 14-17-fold increase in signal that was obtained in this paper, taking into account that gold has a reduced ability to produce SPR. It is hypothesised that it would be possible to observe real fluorescence enhancement from the grating substrates with the use of a laser confocal microscope or an angle coupling instrument, like Dr. Byrne's. These instruments will both have linearly polarised light sources and also, in the case for Dr. Byrne's system, would definitely be able to keep a large portion, if not all, of the light at the angle required to couple into the gratings.
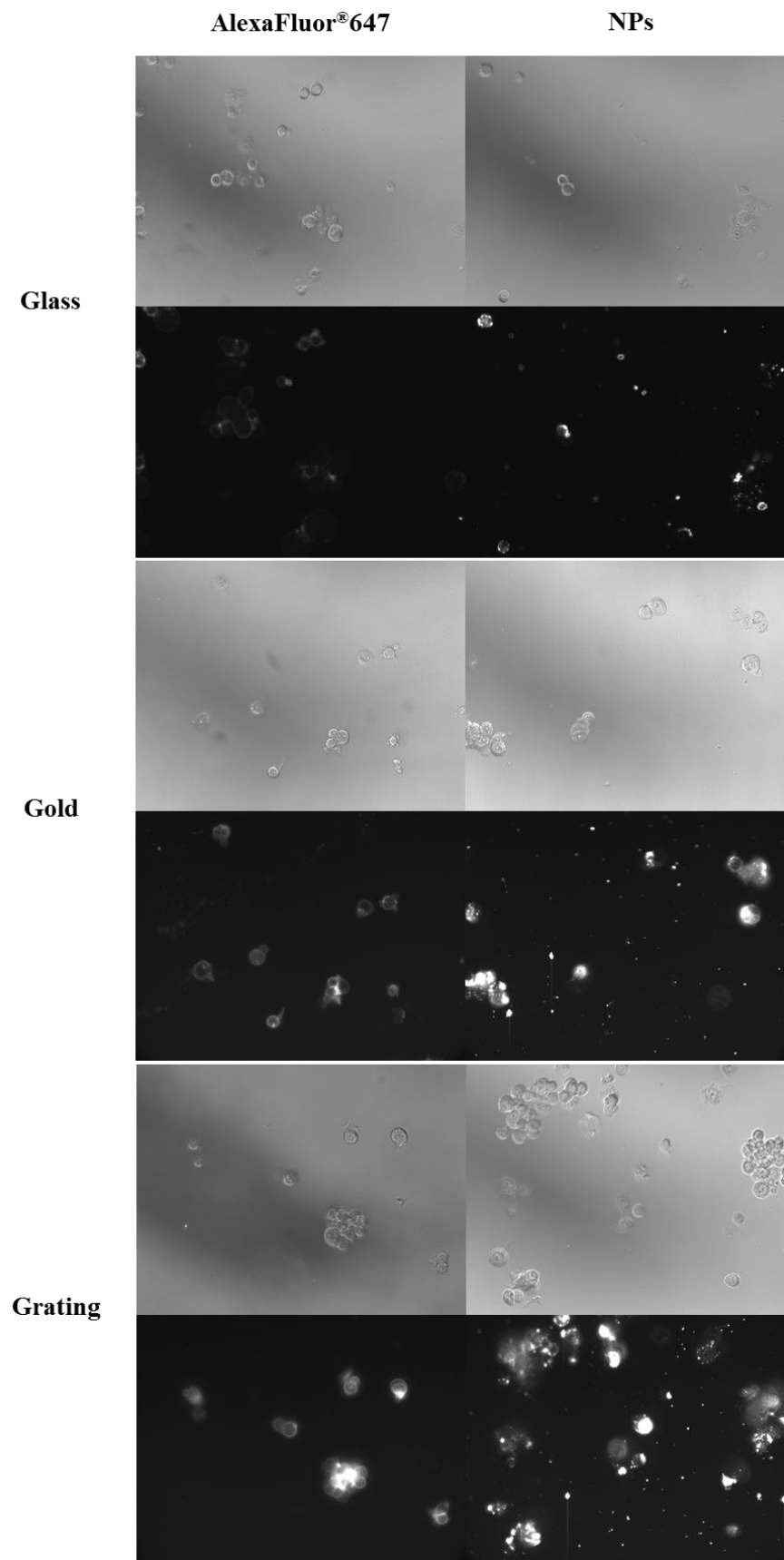
Fig 8.11: MCF-7 cells stained with anti-EpCAM AlexaFluor®647 or NPs on glass, gold or gold grating substrates.

8.4 Conclusions

Gold coated gratings were investigated for the enhancement of cell imaging compared to plane gold and glass substrates. A small enhancement of 1.6x, grating to gold and 6.3x grating to glass was achieved using AlexFluor®647 dye and 1.3x, and 1.8x respectively for NPs. This would indicate that the NPs are best suited for use in glass substrate staining to get maximum differentiation compared to AlexaFluor®647. Challenges have emerged in detecting statistically significant enhancements on a microscope system that was previously measured on a laser diode angle coupling system devised by Dr. Byrne. However, camera response does not appear to interfere with the ability to detect these enhancements as was investigated by means of increasing dye labelled antibody concentrations and measuring on a microscope and microplate reading system. The other issue with using a microscope system is that the angle of illumination is fixed and not necessarily linearly polarised as is required to see large enhancements. Microscope illumination operates generally in a wide range of angles with only one of those angles able to couple into the grating. With the use of a laser confocal microscopy system it may be possible to see more of the enhancement and if the angle of excitation could be adjusted, such as per Dr. Byrne's system or even tested on this system, then I believe that an enhancement should be attainable.

8.5 References

[1] D. Byrne, P. Duggan, C. McDonagh, Controlled surface plasmon enhanced fluorescence from 1D gold gratings via azimuth rotations, Methods Applied Fluorescence. 5 (2017) 015004.

[2] H. Raether, The dispersion relation of surface plasmons on rough surfaces; A comment on roughness data, Surf. Sci. 125 (1983) 624-634.

[3] W. Knoll, Interfaces and thin films as seen by bound electromagnetic waves, Annu Rev Phys Chem. 49 (1998) 569-638.

[4] J.R. Lakowicz, Radiative decay engineering 5: Metal-enhanced fluorescence and plasmon emission, Anal. Biochem. 337 (2005) 171-194.

[5] E. Kretschmann, The angular dependence and the polarisation of light emitted by surface plasmons on metals due to roughness, Opt. Commun. 5 (1972) 331-336.

[6] A. Otto, Excitation of nonradiative surface plasma waves in silver by the method of frustrated total reflection, Z. Physik. 216 (1968) 398-410.

[7] X. Cui, K. Tawa, H. Hori, J. Nishii, Tailored plasmonic gratings for enhanced fluorescence detection and microscopic imaging, Adv. Funct. Mater. 20 (2010) 546-553.

[8] H. Hori, K. Tawa, K. Kintaka, J. Nishii, Y. Tatsu, Surface profile dependence of the photon coupling efficiency and enhanced fluorescence in the grating-coupled surface plasmon resonance, J. Appl. Phys. 107 (2010).

[9] K. Tawa, C. Sasakawa, T. Fujita, K. Kiyosue, C. Hosokawa, J. Nishii, M. Oike, N. Kakinuma, Fluorescence microscopy imaging of cells with a plasmonic dish integrally molded, Jpn. J. Appl. Phys. 55 (2016).

[10] A.J. Tudos, R.B.M. Schasfoort, Introduction to Surface Plasmon Resonance. in: A.J. Tudos, R.B.M. Schasfoort (Eds.), Handbook of Surface Plasmon Resonance, RSC Publishing, Cambridge, 2008, pp. 1-13.

[11] D.W. Unfricht, S.L. Colpitts, S.M. Fernandez, M.A. Lynes, Grating-coupled surface plasmon resonance: A cell and protein microarray platform, Proteomics. 5 (2005) 4432-4442.

[12] J.M. Rice, L.J. Stern, E.F. Guignon, D.A. Lawrence, M.A. Lynes, Antigen-specific T cell phenotyping microarrays using grating coupled surface plasmon resonance imaging and surface plasmon coupled emission, Biosens. Bioelectron. 31 (2012) 264-269.

[13] P.J. Mok, W. Leung, K. Constant, T.-. Kim, K.-. Ho, Nanowires - Implementations and Applications, in: A. Hashim (Ed.), Laser Interference Lithography and Shadow Lithography for Fabricating Nanowires and Nanoribbons. InTech, 2011.

[14] S.-. Yoon, M.R.K. Mofrad, Cell adhesion and detachment on gold surfaces modified with a thiol-functionalized RGD peptide, Biomaterials. 32 (2011) 7286-7296.

[15] A.J. Gormley, A. Malugin, A. Ray, R. Robinson, H. Ghandehari, Biological evaluation of RGDfK-gold nanorod conjugates for prostate cancer treatment, J. Drug Targeting. 19 (2011) 915-924.

[16] C. McDonagh, O. Stranik, R. Nooney, B.D. MacCraith, Nanoparticle strategies for enhancing the sensitivity of fluorescence-based biochips, Nanomedicine. 4 (2009) 645-656.

Chapter 9: Conclusions and outlook

9.1 Conclusions

In conclusion, the overarching aim of this research project, which was '*to demonstrate the specific staining of circulating tumour cells from blood with fluorescent silica nanoparticles for cell staining, both in flow cytometry and imaging, in comparison to single dye molecules*' was successfully achieved.

Cyanine5-doped silica nanoparticles were synthesised using a modified reverse microemulsion method. Two sets of NPs, doped with different weight percent dyes, were approximately 40 nm in size immediately after synthesis and were characterised quantitatively in terms of size, zeta potential and number of dye molecules inside the NPs. Their size was measured using TEM at stages throughout the synthesise steps and shows that with the addition of functionalisation steps that they become no larger than 66 nm before the addition of an antibody. The number of dye molecules that was measured on average per NP, was found to be 137 and 155 dye molecules for the 0.168 (w/w%) and 0.279 (w/w%) dye loaded NPs respectively. Models that were produced based on homo-FRET interactions between dye molecules within the nanoparticle matched well with experimental results and showed that the fluorescence emission peaked at 0.4 (w/w%) loading of dye and that after this amount there was no benefit from the addition of more dye as it induced greater FRET effects.

The conjugation of antibody was first verified using Cyanine3 labelled anti human IgG which was conjugated to the surface and subsequently used to estimate the number of antibodies that were bound via monitoring the supernatant of the solution. This number was found to be 79 ± 5 antibodies per NP. Also, 100% of the antibodies on the NPs were available to bind to analyte that was in solution phase. Knowing this, CTC specific anti-EpCAM antibody was confidently conjugated to the surface using the same method knowing that it would retain specificity.

Both sets of NPs were incubated with an EpCAM positive breast cancer cell line and a cervical cancer EpCAM negative cell line, MCF-7 and HeLa. The NPs showed

specificity to the MCF-7 line and were compared to commercially available anti-EpCAM APC and AlexaFluor®647. Flow cytometry results showed that the 0.168% NPs were twice as bright as the APC and almost three times as bright as AlexaFluor®647. Good specificity was also observed using image analysis methods. Using laser confocal microscopy, NPs were confirmed to be on the surface of the MCF-7 cells where the EpCAM protein is expressed and not endocytosed in the time frame of a few hours. Good specificity was also achieved for a lower EpCAM expressing cancer cell line, LNCaP, which is a prostate cancer line and compared with a healthy cancer line PNT1A.

Patient blood samples were mimicked by spiking the cultured cells into healthy donor blood at different ratios of CTCs to WBCs. NPs were able to distinguish spiked MCF-7 cells up to ratios of 50:1, WBC: CTC, using 0.168% NPs and 20:1 with spiked LNCaP cells. Despite non-specific binding of the NPs to WBCs the number of NPs bound to CTCs was an order of magnitude higher and so via flow cytometry the CTC cell cloud could be identified above the WBC cloud in the red2 channel of the flow cytometer. Comparison of the performance to AlexaFluor®647 shows that the AlexaFluor®647 is more sensitive as it can detect the CTCs at levels of 127:1 and 115:1 for MCF-7 and LNCaP cell lines respectively, indicating that the NPs do need to be improved in terms of non-specific binding. Imaging of the cells complimented the flow cytometry data showing more NPs bound to the CTCs than the WBCs.

Work was carried out to investigate the use of a secondary antibody-antibody labelling system that, when used with dye labelled antibodies, produced a more sensitive detection system. Results from using a secondary system with NPs showed that they were specific as they bound to MCF-7 cells well, compared to HeLa cells. An issue with non-specific binding of the control goat anti-mouse AlexaFluor®647 antibody made it difficult to assess the comparability of the performance of the NPs in this system. There appeared to be no real advantage of using the secondary system over primary staining methods as the overall increase in fluorescence was not larger.

Cell staining was carried out on gold grating surfaces with the intention of showing enhancement on these substrates compared with plane gold and glass substrates. An increase of signal was produced from AlexaFluor®647 labelled MCF-7 cells on the gold grating surfaces but only by an increase of 1.6x compared to the plane gold surface and not nearly the enhancement that was observed on a laser diode system where an

enhancement of up to 30-fold can be observed with the correct conditions. Cells labelled with NPs did not produce as much an enhancement as the dye labelled cells and so there appears to be no real advantage of using NPs over dye labelled antibodies in this application. Despite this, with a more optimised system a greater enhancement could be produced.

9.2 Conclusions in relation to CTC detection

The use of nanoparticles as a viable detection stain for CTCs must be addressed on a number of levels in order to realise them as an enabling technology. Key points of interest are: the number and type of antigens that need to be stained, and, what end goals could be achieved using NP labels, in terms of the challenges in relation to CTC detection. These are discussed below with relevance to studies that have been conducted on patient CTCs.

As CTCs originate in epithelial tissue, it would appear that epithelial markers, such as EpCAM, would be the ideal candidate markers to detect all CTCs of different cancer types. However, the expression of EpCAM on CTCs is not consistent within its lifetime and has been shown to be heterogenous [1,2]. This is due to epithelial to mesenchymal transition (EMT) whereby the cancer cell starts to downregulate the expression of epithelial surface proteins, to promote its preservation from the immune system, chemotherapy and targeted therapy [3,4]. This allows the CTC to stay in circulation long enough to move to another location in the body and upon reversal of the EMT process, the phenotype switches from mesenchymal to epithelial once again via the mesenchymal to epithelial transition (MET) [3,5]. Following this, the tumour cells express epithelial proteins once more, which promotes the ability of the CTCs to form secondary cancer tumours [3,4]. This implies that CTC detection instruments, that use EpCAM as the main distinguishing antigen, may fail to correctly enumerate the CTCs in patients and underestimate those in the circulating system [6]. This is true also for the nanoparticle CTC detection system, where, if EpCAM was to be the sole target antigen, it would fail to enumerate the actual number of CTCs in blood samples. One study looked at the enumeration of EpCAM between different cancer cell lines which included an example of breast, colon, bladder and prostate cancer cell lines [7]. Across the different cell lines there was a large variance in expression of EpCAM, with the MCF-7 cell line expressing approximately 500,000 molecules per cell, closely

followed by colo205 colon cancer and SKBr-3 breast cancer [7]. LNCaP expressed approximately a third less EpCAM molecules than the other cells lines and the T24 bladder cancer cell line only expressed 2,000 molecules. The number of EpCAM molecules on CTCs, from various metastatic carcinoma cancer patients, was found to be in the range of 30,000-60,000 molecules, exhibiting EMT downregulation of epithelial markers [7]. This data strengthens the argument to test CTC systems on patient samples, and not only cell lines, to get a true picture of how robust the EpCAM detection method is. It also points out a flaw in the EpCAM detection method, as not all cell lines are highly EpCAM expressive. If this nanoparticle CTC detection system were to continue, it would be imperative that tests on patient blood samples should be a next step in the development process. Another study, that also came to the same conclusion, showed that using EpCAM for the detection of CTCs in prostate cancer patients was successful 57% of the time. This was compared with the detection of EpCAM positive CTCs from non-small cell lung cancer where the successful detection rate was only 20% [8,9]. It is clear from this study that EpCAM cannot be used for the detection of all types of CTCs. EpCAM can be used for certain carcinomas, like prostate and breast cancers but that for lung and bladder cancer, alternative markers and methods must be applied [9,10]. If this is the case the nanoparticles could only be used on certain types of carcinomas and that other antibodies would have to be conjugated to the nanoparticles to detect other types of CTCs.

As EpCAM is a marker that cannot be relied upon alone, a panel of markers, that are a combination of epithelial and non-epithelial based must be envisaged that should indicate the presence of CTCs in a sample. One negative control that is routinely used is the anti-CD45 negative stain [11]. This is a marker for WBCs that is not expressed by CTCs, however, the expression of CD45 is quite varied between WBCs and some have low/no expression of CD45, particularly neutrophils, myeloid-derived suppressor cells (MDSCs) or other immature myeloid cells [12-15]. The challenge is combing a number of these antigens together to form a panel of antigens to categorise the CTCs. CellSearch®, which was FDA approved, have chosen four steps to categorise a cell as a CTC. These are: that it must be EpCAM positive, cytokeratin positive, have a nucleus and be negative for CD45 [16]. Such a range of markers have been successful in the identification of breast cancer CTCs. Using the nanoparticles as stains would have to follow the same protocol as CellSearch®, in identifying a number of criteria or stains to

identify CTCs in blood. In order to complete this challenge, a range of dyes at different wavelengths would have to be synthesised and antibodies specific to the desired antigens would have to be conjugated to them. This would provide a panel of markers from which the NPs could be used to doubly or triply verify that the EpCAM positive cells are actually CTCs. This would require an investment in time and any issues with non-specific binding would have to be addressed, particularly when dealing with false positives or false negatives. Some suggestions to improve non-specific binding of nanoparticles are suggested in section 9.3. If these challenges can be overcome, such as; detection of low EpCAM expression on patient CTCs, designing of a CTC antigen identification panel and non-specific binding of nanoparticles, then I believe that nanoparticles could be used as a viable stain to identify CTCs from the blood of cancer patients.

9.3 Outlook

Overall, the potential for dye-doped silica nanoparticles to be used as a new type of antibody label was realised throughout this work. The NPs offer a viable alternative to single dye labels for cell staining and, with some optimisation, have the potential to be a very powerful tool in the applications of CTC detection via flow cytometry and microscopy. It is hoped that the work will continue in this field of nanoparticles to improve sensitivity of the NPs and allow the synthesis of highly sensitive cancer detection tools which can improve patient outcome by detecting these rare cells in low numbers.

This is just one application of the NPs, but they could be used for many more specific applications such as rare antigen tagging. This work has shown that NPs containing cheaper dyes with lower quantum yields can be comparable to antibodies conjugated with more expensive dyes of higher quantum yields. Doping the NPs with dyes of higher quantum yield would increase the photon emission of each nanoparticle allowing for brighter emission signal for the detection of those rare surface antigens. Not only can these NPs be used to incorporate red dyes but they can be substituted for most dyes throughout the spectral range thus allowing the development of a large set of nanoparticles for different excitation and emission wavelengths. This could allow for multiple antigen imaging with different dye-doped silica nanoparticles. However, due to the issues regarding non-specific binding that were encountered in this project, time

would need to be invested in optimising the NPs so that there is a reduction of non-specific binding. Some suggestions that have come to light recently include using binding/capping agents such as polyvinylpyrrolidone (PVP) to block the surface of the NPs. Also, upon the advice of researchers in flow cytometry development, a suggestion has been to use low molecular weight linear or branched PEGs in solution to improve the stability of the NPs in biologically viable media. Other possibilities that could lead to more specific staining rather than modifying the staining buffer, include the use of aptamer conjugated nanoparticles or those that use a streptavidin and biotin system instead of antibodies. The use of recognition molecules that have a high binding affinity, such as biotin-streptavidin, should improve the specificity of the NPs by reducing non-specific binding through F_c regions on conjugated antibodies.

There are many possibilities to expand the research of these dye-doped silica nanoparticles into other applications such as drug delivery or single cell analysis. As the NPs synthesised by this method can incorporate not only dye, they could be used as a system of drug delivery. Some modifications to the NPs would have to be made in terms of additional shells of silica and functionalisation but it does have a potential for this application. Also, if the specificity of the NPs can be improved using aptamers or similar then it could be used for high resolution imaging for individual cells such as STED or stochastic optical reconstruction microscopy (STORM) to gain a better understanding of the positioning of rare antigens or cell structures.

9.4 References

[1] L.G. Martelotto, C.K.Y. Ng, S. Piscuoglio, B. Weigelt, J.S. Reis-Filho, Breast cancer intra-tumor heterogeneity, Breast Cancer Res. 16 (2014).

[2] C. Hiley, E.C. de Bruin, N. McGranahan, C. Swanton, Deciphering intratumor heterogeneity and temporal acquisition of driver events to refine precision medicine, Genome Biol. 15 (2014).

[3] H. Hugo, M.L. Ackland, T. Blick, M.G. Lawrence, J.A. Clements, E.D. Williams, E.W. Thompson, Epithelial - Mesenchymal and mesenchymal - Epithelial transitions in carcinoma progression, J. Cell. Physiol. 213 (2007) 374-383.

[4] H. Liu, X. Zhang, J. Li, B. Sun, H. Qian, Z. Yin, The biological and clinical importance of epithelial–mesenchymal transition in circulating tumor cells, J. Cancer Res. Clin. Oncol. 141 (2014) 189-201.

[5] Y. Chao, Q. Wu, M. Acquafondata, R. Dhir, A. Wells, Partial mesenchymal to epithelial reverting transition in breast and prostate cancer metastases, Cancer Microenvironment. 5 (2012) 19-28.

[6] C. Raimondi, C. Nicolazzo, A. Gradilone, Circulating tumor cells isolation: The "post-EpCAM era", Chin. J. Cancer Res. 27 (2015) 461-470.

[7] C.G. Rao, D. Chianese, G.V. Doyle, M.C. Miller, T. Russell, R.A. Sanders Jr., L.W.M.M. Terstappen, Expression of epithelial cell adhesion molecule in carcinoma cells present in blood and primary and metastatic tumors, Int. J. Oncol. 27 (2005) 49-57.

[8] M.G. Krebs, J.-. Hou, R. Sloane, L. Lancashire, L. Priest, D. Nonaka, T.H. Ward, A. Backen, G. Clack, A. Hughes, M. Ranson, F.H. Blackhall, C. Dive, Analysis of circulating tumor cells in patients with non-small cell lung cancer using epithelial marker-dependent and -independent approaches, J. Thorac. Oncol. 7 (2012) 306-315.

[9] W.J. Allard, J. Matera, M.C. Miller, M. Repollet, M.C. Connelly, C. Rao, A.G.J. Tibbe, J.W. Uhr, L.W.M.M. Terstappen, Tumor cells circulate in the peripheral blood of all major carcinomas but not in healthy subjects or patients with nonmalignant diseases, Clin. Cancer Res. 10 (2004) 6897-6904.

[10] E.E. Reyes, D.J. VanderWeele, M. Isikbay, R. Duggan, A. Campanile, W.M. Stadler, D.J. Vander Griend, R.Z. Szmulewitz, Quantitative characterization of androgen receptor protein expression and cellular localization in circulating tumor cells from patients with metastatic castration-resistant prostate cancer, Journal of Translational Medicine. 12 (2014) 1-15.

[11] F.A.W. Coumans, C.J.M. Doggen, G. Attard, J.S. de Bono, L.W.M.M. Terstappen, All circulating EpCAM+CK+CD45-objects predict overall survival in castration-resistant prostate cancer, Ann. Oncol. 21 (2010) 1851-1857.

[12] F. Lacombe, F. Durrieu, A. Briais, P. Dumain, F. Belloc, E. Bascans, J. Reiffers, M.R. Boisseau, P. Bernard, Flow cytometry CD45 gating for immunophenotyping of acute myeloid leukemia, Leukemia. 11 (1997) 1878-1886.

[13] J.L. Schehr, Z.D. Schultz, J.W. Warrick, D.J. Guckenberger, H.M. Pezzi, J.M. Sperger, E. Heninger, A. Saeed, T. Leal, K. Mattox, A.M. Traynor, T.C. Campbell, S.M. Berry, D.J. Beebe, J.M. Lang, High specificity in circulating tumor cell identification is required for accurate evaluation of programmed death-ligand 1, PLoS ONE. 11 (2016).

[14] W. Gorczyca, Z.-. Sun, W. Cronin, X. Li, S. Mau, S. Tugulea, Immunophenotypic Pattern of Myeloid Populations by Flow Cytometry Analysis, Methods Cell Biol. 103 (2011) 221-266.

[15] B. Almand, J.I. Clark, E. Nikitina, J. Van Beynen, N.R. English, S.C. Knight, D.P. Carbone, D.I. Gabrilovich, Increased production of immature myeloid cells in cancer patients: A mechanism of immunosuppression in cancer, J. Immunol. 166 (2001) 678-689.

[16] CellSearch, How does the CellSearch system work? 2017 (2017).

List of publications

Peer reviewed papers:

1. Nooney R., Robello V., Keegan G., <u>O'Connell C.L.</u>, Byrne D., McDonagh C. Highly sensitive detection of C-reactive protein using a novel dissolution approach in a dye-doped silica nanoparticle-based fluorescence immunoassay. *Anal. Methods* (2017) 9(6), 994-1003.

2. <u>O'Connell C.L,</u> Nooney R., McDonagh C. Cyanine5-doped silica nanoparticles as ultra-bright immunospecific labels for model circulating tumour cells in flow cytometry and microscopy. *Biosensors and bioelectronics.* (2017) 91, 190-198.

3. Nooney R., <u>O'Connell C.,</u> Roy S., Boland K., Keegan G., Kelleher S., Daniels S., McDonagh C. Synthesis and characterisation of far-red fluorescent cyanine dye doped silica nanoparticles using a modified microemulsion method for application in bioassays. *Sens. Actuators B* (2015) 221, 470-479.

4. Nooney R., White A., O Mahony C., <u>O'Connell C.,</u> Kelleher S. M., Daniels S., McDonagh C. Investigating the colloidal stability of fluorescent silica nanoparticles under isotonic conditions for biomedical applications. *J. of Colloid and Interface Sci.* (2015) 456, 50-58.

5. Czugala M., <u>O'Connell C.,</u> Blin C, Fischer P., Fraser K. J., Benito-Lopez F., Diamond D. Swelling and shrinking behaviour of photoresponsive phosphonium-based ionogel microstructures. *Sens. Actuators B* (2014) 194, 105-113.

In preparation

Detection of model CTCs from blood using cyanine5-doped silica nanoparticles. <u>O'Connell C.L.</u>, Nooney R., McDonagh C. *In prep.*

Conference proceedings:

1. <u>O'Connell C.</u>, Nooney R., Glynn M., Ducrée J., McDonagh C. Fluorescent cyanine5-doped silica nanoparticles for cancer cell imaging. *Proceedings of SPIE Optics and Photonics*. San Diego, USA. August 2015.

2. Kirby D., O'Connell C., Ducrée J. Continuous, stopped-flow separation for integrated blood cell enrichment and analysis on centrifugal microfluidic platforms. *Proceedings of the 4th European Conference on Microfluidics.* Limerick, Ireland. December 2014.

3. Czugala M., O'Connell C., McKeon A., Blin C., Fischer P., Fraser K. J., Dermot D., Benito-Lopez F. Photo-patterning of ionogel microstructures for on-chip microvalve applications controlled by fiber optics. *2013 Transducers & Eurosensors XXVII: The 17th International Conference on Solid-State Sensors, Actuators and Microsystems (TRANSDUCERS & EUROSENSORS XXVII).* Barcelona, Spain. June 2013.

Conference poster presentations

1. O'Connell C., Nooney R., McDonagh C. Cyanine5 doped silica nanoparticles as biosensors for the detection of prostate circulating tumour cells from blood. *CYTO 2017.* Boston, USA. June 2017.

2. O'Connell C., Nooney R., McDonagh C. Cyanine5 doped silica nanoparticles for prostate cells detection from blood. *IOP Spring conference.* March 2017, Dublin, Ireland.

3. O'Connell C., Nooney R., McDonagh C. Fluorescent dye doped silica nanoparticles for cell imaging. *Europtrode 2016.* Graz, Austria. March 2016.

4. O'Connell C., Nooney R., Glynn M., Ducrée J., McDonagh C. Fluorescent cyanine5-doped silica nanoparticles for cancer cell imaging. *Photonics Ireland.* Cork, Ireland. September 2015.

5. O'Connell C., Nooney R., Glynn M., Ducrée J., McDonagh C. Fluorescent cyanine5-doped silica nanoparticles for cancer cell imaging. *SPIE Optics and Photonics.* San Diego, USA. August 2015

6. O'Connell C., Nooney R., McDonagh C. Fluorescent dye doped silica nanoparticles for cell imaging. *BOC poster competition.* Dublin City University, Ireland. February 2015

7. O'Connell C., Nooney R., McDonagh C. Fluorescent dye doped silica nanoparticles for cell imaging. *IUPAC workshop, Nanomaterials and Human*

Health: Trends and Future Outlook. University of Kent, Canterbury, UK. August 2014.

8. O'Connell C., Nooney R., McDonagh C. Fluorescent dye doped silica nanoparticles for cell imaging. *IOP Spring conference*. Dublin, Ireland. March 2014

9. O'Connell C., Czugala M., Benito Lopez F., Diamond D. Micro-bioreactors controlled with photonic ionogel actuators. *2nd International Symposium on Functional Nanomaterials*. Dublin City University, Ireland. September 2012.

Awards

- Recipient of the DCU Faculty of Science and Health Outstanding Graduate Researcher award 2017
- Recipient of ISAC student travel award 2017 to attend *CYTO 2017*.
- 2nd place "Tell It Straight" DCU science communication competition in 'Late stage' PhD oral category 2017
- 1st place "I'm A Scientist Get Me Out of Here" Nanoscience Zone 2015
- 1st place "Tell It Straight" DCU science communication competition in video category 2015
- Finalist of Institute of Physics (Ireland) IOP Spring conference science communication competition 2017
- Finalist in ResearchFest at InspireFest 2016
- Finalist of "Thesis in Three" science communication competition 2014

Appendix A: Programming codes for homo-FRET models

A1: Codes for calculation of Forster radius:

```
% script for calculating Forster radius between Cy5 and Cy5 (homofret)

ext_Cy5= load('ext_Cy5.txt'); % M^(-1)*cm^(-1)

em_Cy5 = load('em_Cy5.txt');

step=1;

lambda = 500:step:850; %in nm units

ex= spline(ext_Cy5(:,1),ext_Cy5(:,2),lambda);

em= spline(em_Cy5(:,1),em_Cy5(:,2),lambda);

dl= step*ones(size(lambda));


J = (em.*ex.*lambda.^4*dl')/(em*dl') % in M^(-1)*cm^(-1)*nm^4


kappa = 2/3  % isotropic orientation

fiD = 0.20 % quantum efficiency of Cyanine5

n = 1.5 % refractive index of the surrounding medium

Na = 6.023*10^23 % Avogadro constant in mol^(-1)


R = (9*log(10)/(128*pi^5*Na)*10^17*kappa^2*fiD/n^4*J)^(1/6) % in nm
```

A2 Radius vs FRET models

% script for calculating the homo-fret in high brightness NPs

R0 = 5.5525; % forster radius for homo-fret of given dye in nm

fi = 0:0.01:1; % range quantum efficiency of the dye

r = 0:0.1:10; % distance in nm

Eff = R0^6./(R0^6 + r.^6); % FRET efficiency equation rearranged

[EFF, FI] = meshgrid(Eff, fi);

Ft = (1 - EFF)./(1-FI.*EFF); % equation from paper

fi = 0.20; % QY for cyanine5

n=1:3:3000; % no. of fluorophores

R=0.5:0.5:30; % radius of NP in 0.5nm steps

[nn,RR] = meshgrid(n,R);

% **Total fluorescence from one NP**

r6= 16/9*pi^2*RR.^6./nn.^2;

Ef= R0^6./(R0^6 + r6);

nFt= nn.*(1-Ef)./(1-fi*Ef);

md= 616.19 % mol. weight of dye

Na= 6.022*10^23 % Avogadro const

% **Calculation weight percent dye loading**

j=41;

Rw = R(j) % specific radius of the NP 20.5 nm radius

wt = n*md/Na./(n*md/Na + 4/3*pi*Rw^3*1.6*10^(-21))*100; %mass of dye/total mass NP

figure(3)

```matlab
plot(wt, nFt(j,:));

xlabel('wt [%]');

ylabel('relative fluorescence by homofret')

title(['Radius of HB NP = ' num2str(Rw) 'nm (forster radius =5.55 nm, fi=0.20 )'])


assignin('base','x_values',wt.');

assignin('base','y_values',nFt(j,:).');


save Cy5_20.5nm_r_fluorescencetestsave.out nFt -ASCII

save weightCy5testsave.out wt -ASCII


figure(4)

plot(wt,n);

xlabel('wt [%]');

ylabel('# of molecules')

title(['Fluorphores inside HB NP = ' num2str(Rw) 'nm (forster radius =5.55 nm, fi=0.20 )'])


assignin('base','x_molecule_values',wt.');

assignin('base','y_molecule_values',n.');
```

Appendix B: Supplementary figures for chapter 4
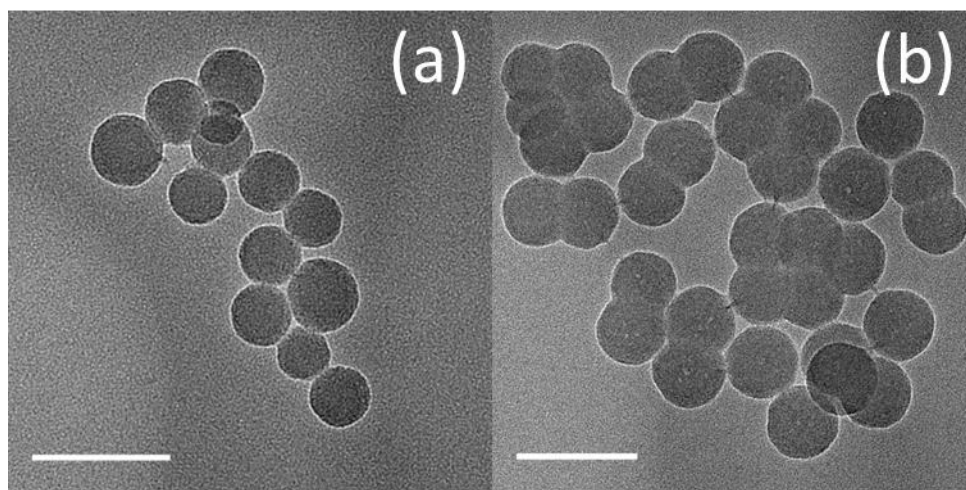
Fig B1: 1% NPs (a) as synthesised radius of 20.4 ± 1.0 nm and (b) PEGylated radius 29.0 ± 1.3 nm. The scale bar represents 100 nm.
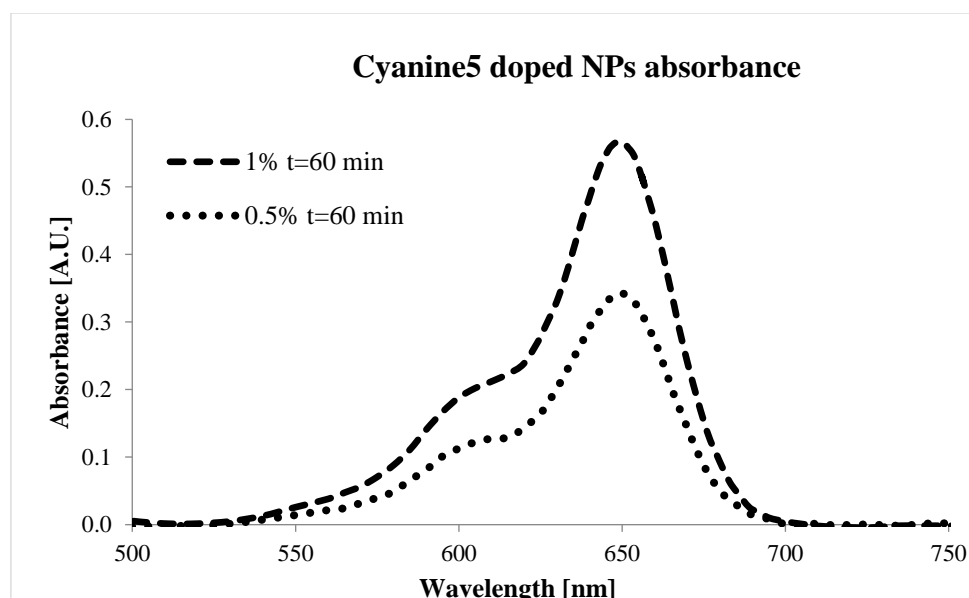

Fig B2: Absorbance of 0.5 w/w% and 1 w/w% Cy5 NPs after dissolution (t=60 min) of the silica matrix using carbonate buffer at pH 10.0. The absorbance of each set was background subtracted to reflect a true change in the absorbance at 650 nm.

0.168% NP labels as synthesised fluoresence comaprison to dye molecuels

y = 2.49E+12x - 9.15E+00
R² = 1.00E+00

y = 1.93E+10x - 3.61E+00
R² = 1.00E+00

- 0.168% NPs
- Free dye

Fluorescence [A.U.]

Concentration of labels [M]

0.279% NP labels as synthesised fluoresence comaprison to dye molecules

y = 1.78E+12x + 3.22E+01
R² = 1.00E+00

y = 1.57E+10x + 5.47E+00
R² = 1.00E+00

- 0.279% NPs
- Free dye

Fluorescence [A.U.]

Concentration of labels [M]

Fig B3:Graph of fluorescence of NP labels 0.168% (top) and 0.279% labels (bottom) in blue compared to free cyanine5 dye molecules in red using a cascade dilution of concentrations for each label.

# Appendix C: Supplementary figures for chapter 5
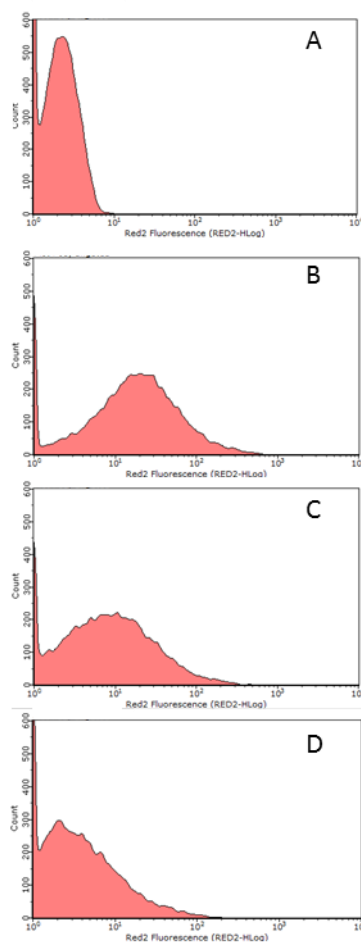
Fig C1: Optimisation of 0.279% NP concentration for incubation with cells to minimise non-specific binding with HeLa cells. (A) represents HeLa cells only (B) HeLa cells with 20 µg of NPs (C) with10 µg of NPs and (D) with 7.5 µg of NPs
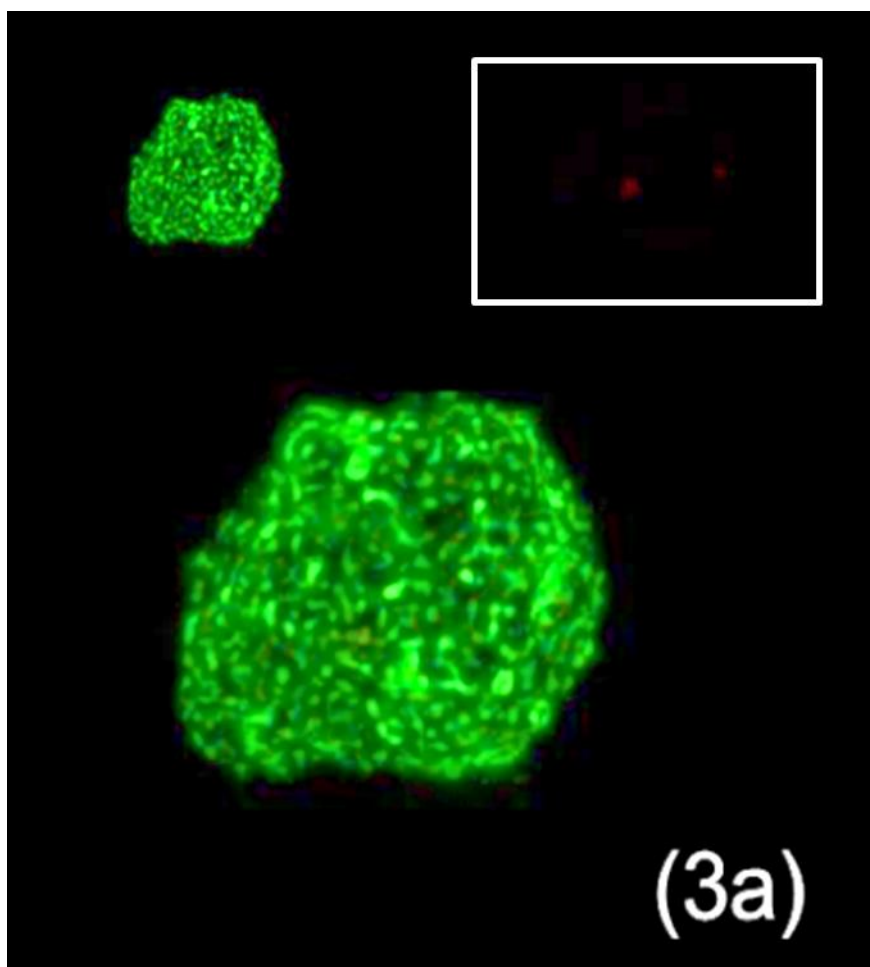
Fig C2: Enlarged and enhanced (3a) image from Fig 5.4 showing NPs on HeLa cell (in white box)

# Appendix D: Supplementary figures for chapter 6
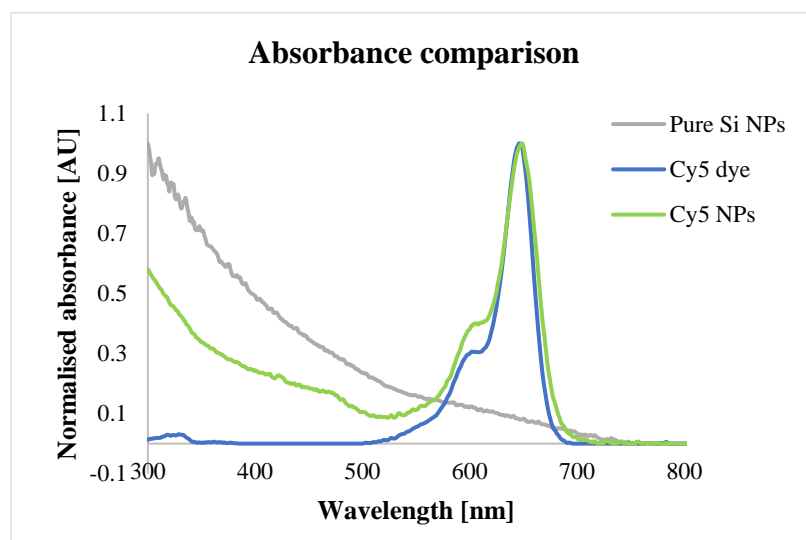
Fig D1: Absorbance spectra for pure silica (Si) NPs, Cyanine5 (Cy5) dye and Cyanine5 doped silica NPs
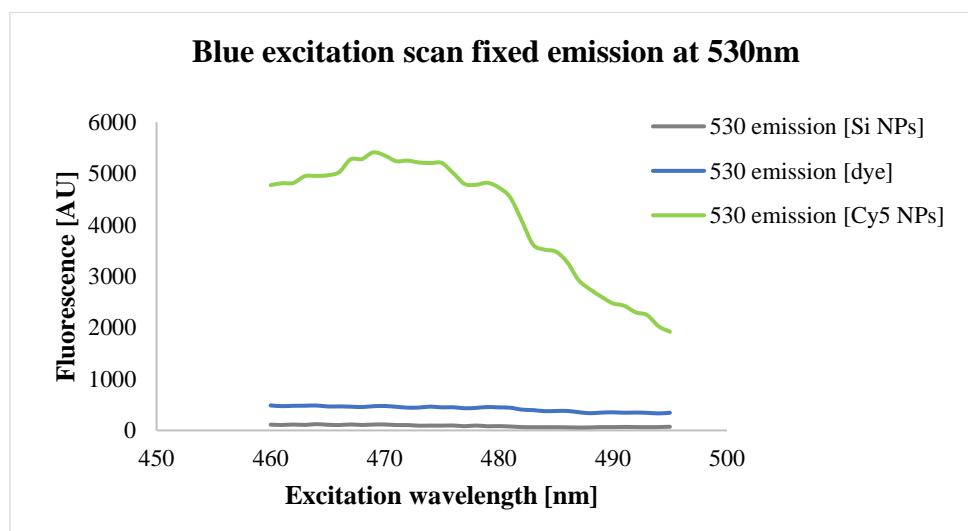

Fig D2: Fluorescence emission of pure silica (Si) NPs, Cyanine5 (Cy5) dye and Cyanine5 doped silica NPs at a fixed wavelength over a range of excitation wavelengths.